SLAC-386
UC-414
(T/E)

AN AMPLITUDE ANALYSIS OF THE K K-BAR SYSTEM ($M < 2$ GeV/c^2) PRODUCED IN J/ψ RADIATIVE DECAY*

LIANG-PING CHEN**

Stanford Linear Accelerator Center
Stanford University
Stanford, California 94309

November 1991

Prepared for the Department of Energy under contract numbers
DE–AC03–76SF00515, DE–AC02–76ER01195,
DE–AC02–87ER40318, DE–AC03–81ER40050, and DE–AM03–76SF00010

Printed in the United States of America. Available from the National Technical Information Service, U.S. Department of Commerce, 5285 Port Royal Road, Springfield, Virginia 22161.

---

* Ph.D. thesis

** Permanent address: Department of Physics and Astronomy, Vanderbilt University, Nashville, TN 37235, USA.

ABSTRACT

Using the 5.8×10^6 J/ψ events collected by the MARK III experiment on the SPEAR e^+e^- storage ring at SLAC, a mass independent amplitude analysis of the $J/\psi \to \gamma\ K_s K_s$ and $J/\psi \to \gamma\ K^+K^-$ decays is presented. For $K\overline{K}$ systems having mass less than 2 GeV/c^2, the efficiency-corrected spherical harmonic moments of the J/ψ joint decay angular distribution are measured. Fits are then performed in each independent mass interval in order to extract the underlying helicity amplitude structure; amplitudes describing $K\overline{K}$ systems of spin zero and spin two are included simultaneously.

For the first time, a large spin zero component in the $\theta(1720)$ mass region is observed; consistent results are obtained for the data samples corresponding to the individual decay modes. This structure is attributed to the production of an S wave resonance, the $f_0(1710)$, of mass and width $M = 1710 \pm 20\ MeV/c^2$, $\Gamma = 186 \pm 30\ MeV/c^2$, respectively, with branching fraction $Bf(J/\psi \to \gamma f_0, f_0 \to K\overline{K}) = (6.47 \pm 1.14 \pm 0.84) \times 10^{-4}$. A small amount ($\sim 24\%$) of spin two component in this mass region cannot be ruled out with the present statistics. These results revise the previous conclusion that the $\theta(1720)$ is a spin two resonance, a result obtained on the basis of spin hypothesis tests, which assumed that either pure spin zero or pure spin two states contribute in this mass region, but not both.

The previous measurements of the $f_2'(1525)$ have been refined in the present analysis because of the simultaneous inclusion of spin zero and spin two amplitudes in the fit. The ratios of the helicity amplitude intensities for this state are found to be $\frac{|a_{21}|^2}{|a_{20}|^2} = 1.08 \pm 0.31$ and $\frac{|a_{22}|^2}{|a_{20}|^2} = 0.25 \pm 0.24$, and are consistent with the interpretation of the $f_2'(1525)$ as a $q\overline{q}$ meson.

ACKNOWLEDGEMENTS

First of all, I would like to thank my thesis advisor, Prof. Bob Panvini for providing me the opportunity to participate in two experiments at SLAC, SLD and MARKIII, and to thank Prof. Walter Toki at SLAC, who, along with Bob, made the arrangement that allowed me to join the latter experiment.

I am deeply grateful to all members of the MARKIII collaboration. It is their hard work that provided the data and made this analysis possible. Special thanks should go to Walter Toki, Bill Dunwoodie and Bill Lockman, who provided advice on every aspect of this analysis, to Min-Zu Wang, who worked together with me during the early stages of this analysis, to Larry Parrish, Tim Bolton.... who, along with the people above, are helping me on the paper for publication.

It should be pointed out that without the training I received during the two years of work on SLD, I would be much more inexperienced in the area of data analysis. I am grateful for the guidance on drift chamber hardware and data analysis from Richard Yamamoto, Charlie Young, Patrick Reutens, Kirk Bunnell, John Venuti, Ray Cowan, Gary Word, Leon Rochester and George Chadwick. In collaboration with these people, a resolution measurement was made with a prototype of the SLD central drift chamber; this is described in SLD New Detector Note No. 195. I also value the guidance I received in studing the physics feasible with SLD from Traudl Hansl-Kozanecka and the Vanderbilt group at SLAC.

On a more personal level, I would like to thank my parents, my family and friends, relatives, most especially my wife Lei Yang. Nothing could have happened without their support.

TABLE OF CONTENTS

LIST OF TABLES

LIST OF ILLUSTRATIONS

CHAPTER I

INTRODUCTION

The J/ψ Laboratory

Since the discovery of the J/ψ resonance in 1974,[1] the production of this $c\bar{c}$ bound state through high energy e^+e^- collisions has provided a useful laboratory for interesting and detailed studies in light meson spectroscopy. That the J/ψ is well suited for this purpose is a consequence of its unique physical characteristics.

First of all, its production rate is high compared to the continuum background. The mass and width of the J/ψ are:[2] $M_{J/\psi} = 3096.9 \pm 0.1 MeV/c^2, \Gamma_{J/\psi} = 68 \pm 10 KeV/c^2$. The quantum numbers are $I^G(J^{PC}) = 0^-(1^{--})$. These well established quantities provide precise initial state information for studies of its decay processes. In addition, the vector nature of the e^+e^- production mechanism[3] causes the J/ψ to be produced with only transverse polarization, i.e. helicity ± 1; this is especially useful for spin-parity analyses of the type described in this thesis.

The narrow width of the J/ψ is due to the fact that it is too light to decay to charmed meson pairs, while its decay to light mesons is suppressed by the OZI rule.[4] This results in a life time which is long in comparison to those of other particles which also decay through the strong interaction. On average, J/ψ decays involve about four charged tracks and a similar number of neutral particles in the final state. The resulting small number of tracks in the detector for each event allows for complete event reconstruction with good efficiency. The

narrow width of the J/ψ allows a kinematical fit to be made event by event, which requires the total energy and momentum of the tracks in the final state be consistent with those of the J/ψ, which is produced at rest. The kinematic fit appreciably improves the resolution of the measured quantities for each event, especially those of the photons in the final state.

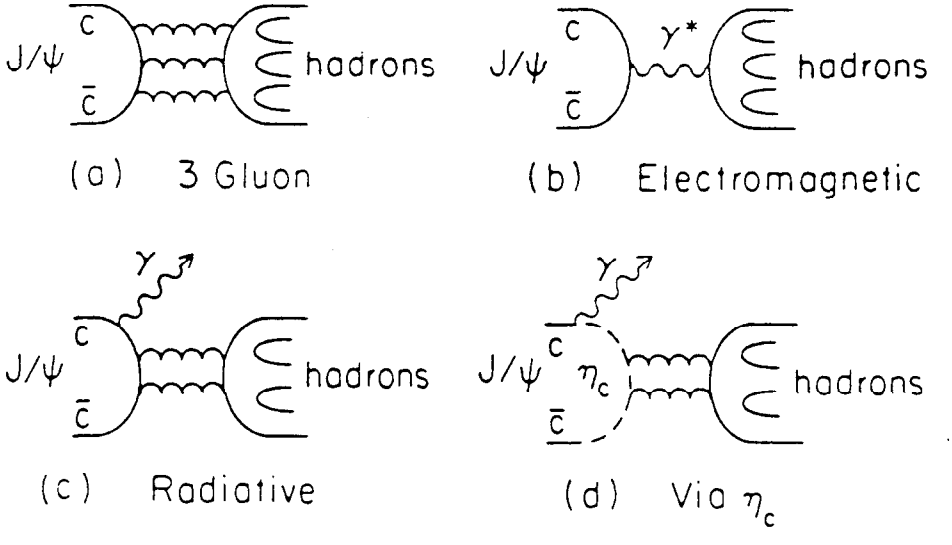

Figure 1. The first order decay diagrams of the J/ψ ; a) three gluon annihilation, b) electromagnetic decay, c) radiative decay, d) transition through η_c.

The four leading mechanisms describing J/ψ decay to hadrons are sketched in Fig.1; they represent (a) the hadronic decay via $c\bar{c}$ annihilation into three gluons, (b) the electromagnetic decay via $c\bar{c}$ annihilation to a virtual photon, (c) the radiative decay with $c\bar{c}$ annihilation into a photon and two gluons, (d) the magnetic dipole transition to the $c\bar{c}$ $^1S_0$ state $\eta(2980)$. Using lowest order expressions with first order QCD corrections, the decay rates corresponding to these mechanisms are calculated in perturbative QCD to be:[5]

$$\Gamma_{ggg} : \Gamma_{\gamma^*} : \Gamma_{\gamma gg} : \Gamma_{\gamma\eta_c} = 75 : 16 : 8 : 1.$$

Radiative decays, which are the focus of this analysis, thus account for about 7% of the total width, after taking account of decays to lepton pairs. The two-gluon system in the radiative decay is of particular interest since non-perturbative QCD models predict the existence of gluonic bound states (glueballs), as discussed in the next section, with masses accessible via this J/ψ decay mode.

In J/ψ radiative decay, C parity is a good quantum number. Since the J/ψ and the photon have negative C parity, it follows that the systems recoiling against the radiated photon are constrained to have even C parity. Furthermore, for those which decay to a pseudoscalar pair (such as K_sK_s, and K^+K^-, which are the subject of this analysis), the spin of the resulting system is even and the parity positive. The isospin of these systems is zero, since the production rate

for isovector systems is low.† The corresponding G parity is positive. In the present analysis, which is concerned with systems with mass less than $2GeV/c^2$, spins as high as 4 are excluded, since objects with such high spin are unlikely to exist in this mass region. Therefore the quantum numbers of the intermediate states of the pseudoscalar pairs are restricted to $I^G(J^{PC}) = 0^+(0^{++}, 2^{++})$.

The Light Meson Spectroscopy and Glueball Phenomenology

The study of light meson spectroscopy dates from the discovery of the first few mesons. Though a large number of light mesons have been observed, and although the quark model provides a consistent qualitative interpretation of most of these states, a complete quantitative accounting of this spectroscopy is still lacking. The difficulties of the spectroscopy are two-fold. Theoretically, QCD cannot be used to make quantitative predictions of the masses of the states, since perturbative techniques do not apply in the light quark sector; experimentally, high statistics measurements are required in order that detailed amplitude analyses can be carried out. This is an essential technique for isolating resonances with different spins which overlap in mass.

In the framework of the quark model, mesons are interpreted as quark anti-quark, $q\bar{q}$, bound states, and are catalogued in nonet structures according to total spin, parity and charge conjugation parity J^{PC}.‡ For example, using

† The process by which an isovector system is produced with a recoiling photon is that of Fig. 1a) with a photon emitted from the final state. The rate of this process is reduced by a factor of $\alpha = \frac{1}{137}$, the electromagnetic fine structure constant, which describes the coupling of the additional photon to the final state.

‡ C for the neutral, non-strange members of the nonet.

J^{PC}	$I=1$	$I=0$	$I=0$	$I=\frac{1}{2}$	EXTRA FOR $I=0$
2^{++}	$\underline{a_2(1320)}$	$\underline{f_2(1270)}$	$\underline{f_2'(1525)}$	$\underline{K_2^*(1430)}$	$+{}^{f_2(1720)}_{g_T(2100-2400)}$
1^{++}	$\underline{a_1(1270)}$	$\underline{f_1(1285)}$	${}^{f_1(1420)}_{f_1(1530)}$	$\underline{K_1(1400)}$	
0^{++}	$\underline{a_0(980)}$	$\underline{f_0(1300)(?)}$	$\underline{f_0(975)}$	$\underline{K_0^*(1350)}$	$+{}^{f_0(1590)}_{f_0(1750)}$

Figure 2. The status of the ground state triplet P-wave $q\bar{q}$ states.

standard spectroscopic notation,[§] the current status of the ground state triplet P-wave $q\bar{q}$ states is summarized in Fig. 2, which is part of Fig. 5 in Ref. 5. Although the interpretation of some of the scalars is somewhat out of date, Fig. 2 gives an adequate representation of the status of the experimental search for these states. As the symbols indicate, the tensors and pseudovectors are well established, while, among the scalars, the $f_0(1300)$ (listed as $f_0(1400)$ in ref. 2) needs clarification and confirmation. The assignments of the well-established $a_0(980), f_0(975)$ are questioned, since their masses are very low in

§ The symbol a, f and K denote, by convention, states having isospin 1, 0 and $\frac{1}{2}$ respectively.

comparison with their tensor and pseudovector partners ($a_2(1320), a_1(1270)$ for $a_0(980)$, $f_2'(1525), f_1(1420)$ or $f_1(1530)$ for $f_0(975)$). From the small mass splitting of the triplet P-wave $b\bar{b}$ and $c\bar{c}$ states (the various χ states), and of the $K_2^*(1430), K_1(1400)$ and $K_0^*(1350)$ states in Fig. 2, one naively expects a small mass splitting for the remaining triplet P-wave states in Fig. 2. Recent studies[6] suggest that the $f_0(975)$ is a $K\overline{K}$ molecule (a 4 quark state as discussed in the next paragraph), and that the $a_0(980)$ is of similar origin; this would exclude these states from the $q\bar{q}$ picture.

In the context of QCD, the spectroscopy of the low mass meson states is expected to be more complex than that predicted by the quark model. The self-coupling of the gauge bosons in QCD allows the existence of bound states of the gluons (gg, ggg), called glueballs. In addition, QCD models predict the existence of bound states of four quarks ($qq\overline{q}\overline{q}$), quark-gluon hybrids ($q\bar{q}g$), etc. The experimental search for glueball and hybrid states has thus far been inconclusive. The observation of at least one such object would provide an important confirmation of the theory. However, the identification of such non-$q\bar{q}$ states is difficult, since they have no clear predicted characteristics which would distinguish them from conventional $q\bar{q}$ mesons. For example, the signatures naively expected for gluonium (gg) are as follows:[2]

1. no available place in the predicted level structure of the $q\bar{q}$ states;
2. flavor singlet coupling, i.e., equal strength coupling to $u\bar{u}, d\bar{d}$ and $s\bar{s}$ ..... final state configurations;
3. enhanced production in gluon-rich channels such as J/ψ decay;
4. reduced $\gamma\gamma$ coupling;

5. exotic quantum numbers, which are not allowed for $q\bar{q}$ states.

Since non-$q\bar{q}$ states can mix with the $q\bar{q}$ states having the same quantum numbers, signatures 2, 3 and 4 may not be observed. Furthermore, since decay rates depend on various dynamical effects, signature 2 may be obscured by the dynamical effects alone, if these effects are large. Therefore, the only clear evidence for a non-$q\bar{q}$ state will be its having exotic quantum numbers (signature 5), or that it results in there being too many candidates for a particular nonet in the $q\bar{q}$ spectroscopy (signature 1). As there is no conclusive result, as yet, of the search for states with exotic quantum numbers, signature 1 plays an important role in the search for non-$q\bar{q}$ states. However, the application of this signature requires a thorough understanding of the $q\bar{q}$ states themselves.

Among the non-$q\bar{q}$ states, the gg bound states attract attention the most since their configuration is the simplest. The expected J^{PC} values for these states are listed in Table 1; these are obtained by requiring that the two-gluon wave function be symmetric under the interchange of space, spin and color indices. The 1^{-+} possibility is forbidden in a standard $q\bar{q}$ picture, while it is possible for gg if the gluons are off-shell. It should be noted that the gg bound states are isoscalars.

Table 1. Expected quantum numbers for gg states

$L=0$	$J^{PC}=0^{++}, \quad 2^{++}$
$L=1$	$J^{PC}=0^{-+}, \quad 1^{-+}, \quad 2^{-+}$
$L=2$	$J^{PC}=0^{++}, 1^{++}, ..., 4^{++}$
.....	.....

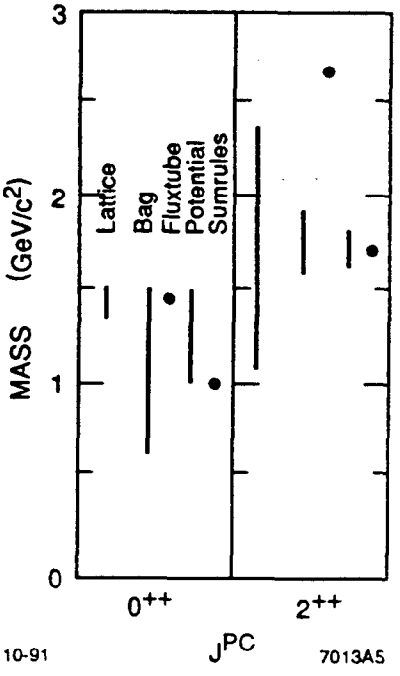

Figure 3. Predicted mass of the ground state scalar and tensor gg glueballs from various QCD models. This figure is extracted from a similar one in reference 5.

The masses of the gg states are predicted by various models, such as QCD lattice gauge calculations, bag models, fluxtube models, potential models and QCD sum rules. The predicted masses of the ground state scalar and tensor gg states are shown in fig. 3. Though the predictions are not very precise, the models generally agree that these glueball states should lie in the mass region of 1 - 2 GeV/c^2; thus they are accessible to the $K\overline{K}$ systems in the present analysis. In contrast, there is no reliable prediction of the widths of such states.

Experimentally, there are several isoscalar states observed, which are interpreted as glueball candidates. For example, $\iota/\eta(1440)$, $G/f_0(1590)$, $\theta/f_2(1720)$.

one or all of the three $g_T(2100-2400)$ states, $\xi(2230)$ etc. For a comprehensive review, the reader is referred to reference 7. In this and in the following sections, the current status of these states is briefly summarized. This task is divided as follows: in the rest of this section, states which are not accessible to this study are discussed (e.g. the $\iota/\eta(1440)$, $g_T(2100-2400)$ and $\xi(2230)$), while in the following two sections, those which are accessible to this study (e.g. the $G/f_0(1590)$, $\theta/f_2(1720)$) are considered. It should be noted that, most of these states (eg. $\iota/\eta(1440)$, $\theta/f_2(1720)$ and $\xi(2230)$) are first observed in J/ψ radiative decay, a gluon-rich channel as discussed earlier; the states under question couple to J/ψ through two gluons, as shown in Fig. 1c). It should also be noted that, apart from the 0^{-+} state, $\iota/\eta(1440)$, all of the above states are listed in Fig. 2 as extra states for the I=0 tensors or scalars. The states with mass less than 2 GeV/c^2 are not possibly assigned to the nonets with radial or higher orbital excitation due to the low masses of these states. Note that being an extra state for the $q\bar{q}$ spectroscopy is an indication of the possible non-$q\bar{q}$ nature of the states.

A recent MARK III partial wave analysis of the $K_s^0K^{\pm}\pi^{\mp}$ system from J/ψ radiative decay[8] concludes that, in the mass region of the $\iota/\eta(1440)$, there are three resonances: a 0^{-+} $a_0(980)\pi$ structure near 1420 MeV/c^2, and 1^{++}, 0^{-+} $K^*\overline{K}$ states at higher mass. These structures are consistent with those observed in the processes $\pi^-p \to K_s^0K^+\pi^-n$ at 8 GeV/c[9] and $\pi^-p \to K_s^0K_s^0\pi^0n$ at 21 GeV/c.[10] The consistency between these gluon-rich (the J/ψ radiative decay) and quark-rich (π p scattering) processes argues against the idea that the 0^{-+} state near 1420 MeV/c^2 is a gluonium state. However, the two 0^{-+}

states observed in this analysis together with the 0^{-+} $\eta(1280)$[11] result in there being three 0^{-+} states for the first radial excitation of the I=0 pseudoscalars, indicating that a non-$q\bar{q}$ state may exist between 1.2 and 1.6 GeV/c^2.

The three 2^{++} $g_T(2100-2400)$ states are found through their decay to $\phi\phi$ in the OZI suppressed process $\pi^- p \to \phi\phi n$[12] (Fig. 8 a)). It is argued that at least one of these states is a glueball which mixes with the otherwise ideally mixed $q\bar{q}$ tensor states and breaks the OZI suppression. There are supporting observations of these states from the WA67 group[13] in the process $\pi^- Be \to \phi\phi + X$, and from the WA76 group[14] in the process $pp \to pp\phi\phi$. The upper limits on the production branching fractions of these states in J/ψ radiative decay set by the MARK III[15,16] and DM2[17] are also consistent with the prediction of R. Sinha,[18] under the assumption that one of these is a gluonium state.

The $\xi(2230)$ is a narrow state ($\Gamma = 18 \pm {}^{23}_{15} \pm 10) MeV/c^2$ reported by MARK III[19] in the processes $J/\psi \to \gamma\xi, \xi \to K^+K^-$ and $\xi \to K_s K_s$. The spin is not determined due to the statistics limitation. The observation of its decay to $\omega\phi$[15] with a branching fraction comparable to those for the above channels, and the observations by the GAMS group[20,21] in the process $\pi^- p \to nX, X \to \eta\eta'$ support its interpretation as a non-$q\bar{q}$ state. But the possible observation in the processes $K^- p \to \Lambda X, X \to K^0_s K^0_s$[22] and $X \to K^+K^-$[23] favors its interpretation as an L=3 $s\bar{s}$ state, in contradiction to the interpretation above. The DM2 group[24] did not observe this resonance in the channels in which MARK III observation was made, though the upper limits set by the DM2 group are consistent with the MARK III branching fraction measurements within error. There is no observation of this state in the process $p\bar{p} \to K\overline{K}$.[25] The conclusion

is that the existence and quantum numbers of this state are uncertain, and that new high statistics studies are required.

The Status of the I=0 Scalar Mesons

The meson full listings of the Review of Particle Properties[2] contain several listings for $I^G(J^{PC}) = 0^+(0^{++})$ states in the mass region from the vicinity of the $K\overline{K}$ mass threshold (995 MeV/c^2 for $M_{K_sK_s}$, 987 MeV/c^2 for $M_{K^+K^-}$) to 2 GeV/c^2, namely, $f_0(975)$, $f_0(1240)$, $f_0(1400)$, $f_0(1525)$, $f_0(1590)$ and $f_0(1750)$. Comprehensive lists of references to experimental studies of these states are contained in this review; some of these states are also discussed in the mini-review of non-$q\overline{q}$ states in this publication. In the present section, brief discussion of these states is provided. The results of the present analysis which are relevant to certain of these states are presented at the end of this thesis.

$f_0(975)$

The mass of this resonance is below K^+K^- and K_SK_S threshold; its width is estimated as 33.6 ± 5.6 MeV/c^2. This resonance is expected to show only as a threshold enhancement in the $K\overline{K}$ data, if it shows at all. Recent studies indicate that this state may be a $K\overline{K}$ molecule.[6]

$f_0(1240)$

This state is reported by only one experiment,[26] seen in phase shift analysis of the K_sK_s system in the process of $\pi^-(23GeV/c)p \rightarrow nK_sK_s$. It needs confirmation.

$f_0(1400)$

The $f_0(1400)$ is seen in $\pi\pi$ phase shift analysis, and it is conventionally interpreted as a $(u\bar{u} + d\bar{d})$ state. However, a large gluonium mixing is not excluded, because the $\eta\eta/\pi\pi$ branching ratio is only half of the flavor-symmetry prediction.[27]

$\underline{f_0(1525)}$

This state is reported by two experiments. First it is seen as a peak in the S-wave intensity distribution as a function of K^+K^- mass in the interaction $K^-(8GeV/c)p \rightarrow K^+K^-\Lambda$,[28] and secondly as an S-wave K_sK_s state in the interaction $K^-(11GeV/c)p \rightarrow K_sK_s\Lambda$.[22] The mass and width reported by the second experiment are consistent with those of the $f_2'(1525)$, but the uncertainties are large.

$\underline{f_0(1590)}$

This state was first seen as an S-wave $\eta\eta$ resonance in the partial wave analysis of the process $\pi^-(38GeV/c)p \rightarrow \eta\eta n$ and named the G(1590) by the GAMS group in 1983.[29] The measured mass and width are 1595 ± 25 and 210 ± 40 MeV/c^2 respectively. With more experiments, its decay rates to various pseudoscalar pairs have been found to be in the following ratio:

$$\pi^0\pi^0 : K\overline{K} : \eta\eta : \eta\eta' : 4\pi^0 =< 0.3 :< 1 : 1 : 3 : 0.8$$

this is peculiar for a $q\bar{q}$ or even a $qq\bar{q}\bar{q}$ state. For the latter states, the rate to $\pi\pi$ or $K\overline{K}$ would be larger by one order of magnitude. As a result, other explorations have been sought. The idea that this particle is a glueball candidate is advocated by Gershtein et al.,[30] who propose that the hadronization of

uncolored pairs of gluons occurs preferentially into η and η'. It is claimed that this proposal follows directly from the data of the J/ψ radiative decays, which favors η' and η compared to π^0 in the ratio of $108 : 22 : 1$.[2] As discussed earlier, J/ψ radiative decay is expected to be a source of glueball production. The large branching fractions for J/ψ radiative decay to η or η' are explained as due to the large gluon content of these states.

Stroot[31] has remarked that the long, unproductive quest for "exotics" (glueballs etc.) may be linked to the fact that experiments using bubble chambers and charged particle spectrometers mostly provide detection of charged π's and of both neutral and charged K's, the particles least likely to show significant gluon content, while they have a low efficiency for the detection of η and η'. Consistent with this speculation, the GAMS group reports evidence for a tensor state at a mass of 2180 MeV/c^2 in the mass distribution of the $\eta\eta$ centrally produced in the reaction $\pi(300GeV/c)p \rightarrow \eta\eta\pi p$ and $p(450GeV/c)p \rightarrow \eta\eta pp$. The properties of this new tensor state are very similar to those of the $G/f_0(1590)$. These peculiar scalar and tensor states found in the $\eta\eta$ systems are speculated to be the lowest lying glueballs.

The $G/f_0(1590)$ has not been observed in the $\pi\pi$, $K\overline{K}$ or $\eta\eta$ systems produced in J/ψ radiative decay, or centrally via double Pomeron exchange. This argues against a glueball interpretation of this state. However, as described in detail in the next section, the θ[32] resonance was seen in the $\eta\eta$ system in J/ψ radiative decay, with mass $1640 \pm 50 MeV/c^2$ and width $220 \pm {}^{100}_{70} MeV/c^2$. These values are consistent with the corresponding values obtained for the $G/f_0(1590)$. These two states might have been considered to be the same were their spins

not different. The spin of the θ was estimated as 2, by means of a pure spin hypothesis test as described in the next section, based on very limited statistics.

$\underline{f_0(1750)}$

A spin zero resonance in the mass region of 1700 MeV/c^2 was first claimed in an amplitude analysis of the reaction $\pi^-(23GeV/c)p \rightarrow K_s^0 K_s^0 n$,[33] based on about 15000 events in the low t region ($|t-t_{min}| < 0.1(GeV/c)^2$). The mass and width were estimated as $M = 1.771 \pm {}^{0.077}_{0.053} GeV/c^2, \Gamma = 0.200 \pm {}^{0.156}_{0.009} GeV/c^2$. With the analysis extended to the whole data sample of 29000 $K_s^0 K_s^0 n$ events,[26] the same group reports that a new scalar resonance is needed in the mass region of 1240 MeV/c^2, as discussed above, and the mass of the $f_0(1750)$ is refined to $M = 1730 \pm 10 \pm 20 MeV/c^2$.

In an experiment to study the inclusive production of the $K_s K_s$ system in $\pi^- N$ interactions at 200 GeV/c,[34] the $f_0(1750)$ is included, together with the dominant smoothly falling background in a fit to the $K_s K_s$ mass spectrum. The fitted parameters obtained are $M = 1.742 \pm 0.015 GeV/c^2, \Gamma = 0.057 \pm 0.038 GeV/c^2$, but there is no spin-parity analysis.

The GAMS experiment, which reports the observation of the G(1590)[29] in the $|t| < 0.2(GeV/c)^2$ region, extends the analysis to the region $|t| > 0.35(GeV/c)^2$, and finds a narrow peak on top of an otherwise continuous $\eta\eta$ spectrum.[35] The statistical significance of this peak is larger than seven standard deviations; the corresponding mass is $M = 1755 \pm 8 MeV/c^2$, the width of the peak is equal to the instrumental resolution so that the intrinsic width of the

resonance is quoted to be less than $50MeV/c^2$. However, the production mechanism of this state must be different from that of the other states, since all resonances seen in the lower t data sample, like the $f_0(1400), f_2(1270), G/f_0(1590)$ etc., do not appear in this high t region.

The latest report of a scalar in this mass region is from the MSS ITEP group.[36] A partial wave analysis of the 6700 $\pi^- p \to K_s^0 K_s^0 n$ events, with $t' < 0.2(GeV/c)^2$, reveals the scalars $f_0(1440)$ and $S^*(1720)$. The mass, width and $\sigma Bf(K\overline{K})$ of the latter scalar are $1720 \pm 60MeV/c^2$, $350 \pm 150MeV/c^2$ and $140 \pm 35nb$. However, the same analysis also reports a tensor in the same mass region with corresponding parameter values $1700 \pm 15MeV/c^2$, $30 \pm 20MeV/c^2$ and $11 \pm 7nb$.

In summary, scalars with a mass around $1700MeV/c^2$ are observed in various experiments, but they may not be all real nor be the same resonance; the measured widths are also different.

The Resonance $\theta(1720)$ and the Estimation of its Spin; the Principle Goal of This Analysis

The resonance, θ,[32] was first reported by the Crystal Ball group in 1982[37] as the $\theta(1640)$ in the $\eta\eta$ system produced in J/ψ radiative decay. The invariant mass distribution of the $\eta\eta$ system for events consistent with the decay $J/\psi \to \gamma\eta\eta$ is shown in Fig. 4. The solid curve in Fig. 4 is a fit to the mass distribution between 1200 and 2400 MeV/c^2 with a relativistic Breit-Wigner resonance plus a flat background; this yields 39 ± 11 resonance events over a background of 0.9 events per 50 MeV/c^2. The spin of this resonance is estimated with the events

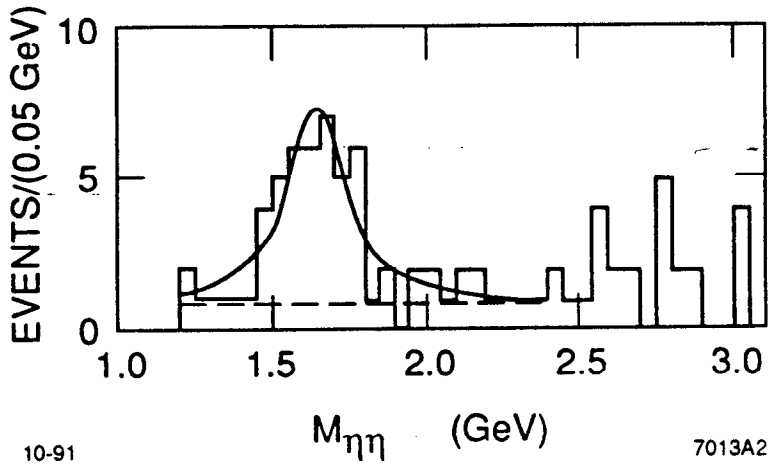

Figure 4. The $\eta\eta$ invariant mass distribution for events consistent with $J/\psi \rightarrow \gamma\eta\eta$ decay from the Crystal Ball experiment. The solid curve represents a fit to the mass distribution. The dashed curve represents the background.

in the selected mass region. The event angular distribution of this sample is compared to the expectation for a pure spin zero or a pure spin two intermediate state. The helicity amplitudes associated with the pure spin two hypothesis are adjusted to maximize the likelihood that the hypothesis describe the data. It is concluded that the pure spin two hypothesis is favored over pure spin zero.

The MARK III[38,39] and DM2[24] groups observe two peaks in the mass region of the $\theta(1640)$ in J/ψ radiative decay to $K\overline{K}$ and $\pi^+\pi^-$. Similar structures are seen by the WA76 group for $K\overline{K}$ systems centrally produced in the reactions $\pi^+p \rightarrow \pi^+(K\overline{K})p$, $pp \rightarrow p(K\overline{K})p$.[40] These observations are illustrated in Figs. 5, 6 and 7. The first peak is identified as the well established $f_2'(1525)$,[2] while the second, with a mass around 1720 MeV/c^2, is assumed to be due to the θ; as a result, the θ is at present referred to as the $\theta(1720)$. To estimate the spin of

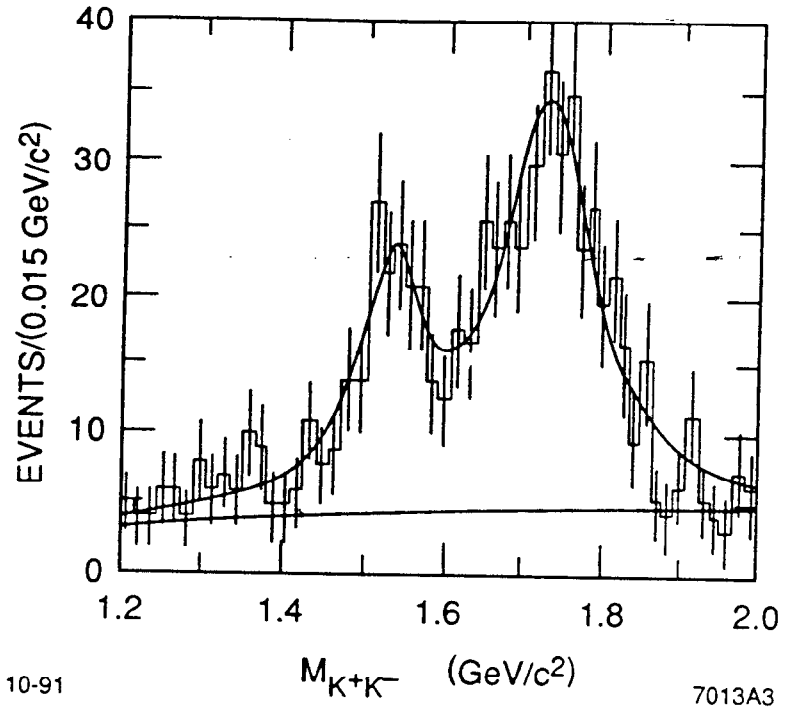

Figure 5. The first half of the MARK III $J/\psi \to \gamma K^+K^-$ data sample.

the θ, the above groups applied a spin hypothesis test similar to that used by the Crystal Ball group, with the $\theta(1720)$ events selected to lie within a particular $K\overline{K}$ or $\pi\pi$ mass range. The MARK III and WA76 groups concluded that the pure spin two hypothesis is favored over pure spin zero.

A pure spin hypothesis test is often used when statistics are low, since in this case an analysis allowing the presence of different angular momentum contributions tends to yield unreliable or ill-defined results. The limitations of such a test are obvious, as it relies on the assumption that only one angular momentum state contributes in the mass region under consideration. When resonances with different spin overlap, the spin hypothesis test cannot, by definition, resolve the contributions from the different spin states, and may in fact lead to erroneous conclusions. For example, if the tail of a spin two resonance overlaps

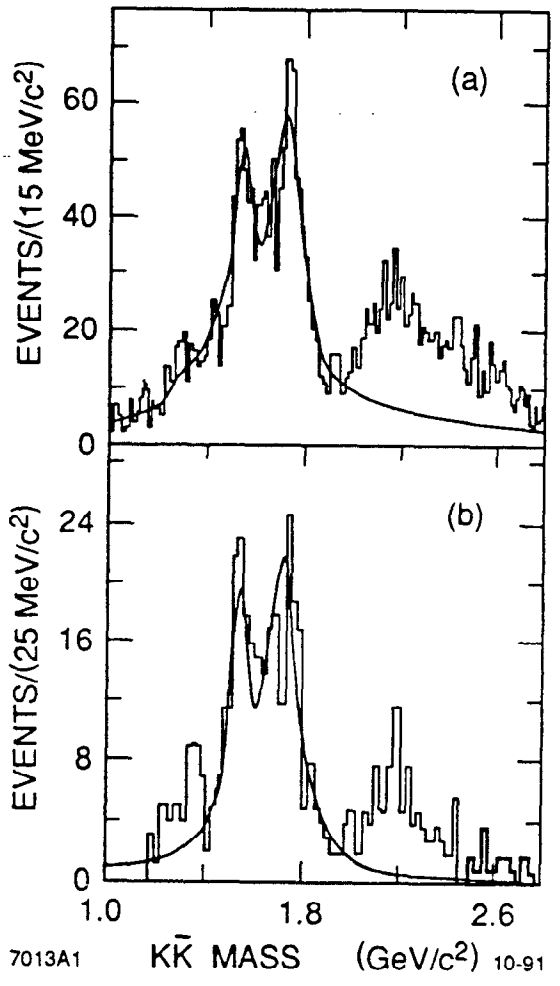

Figure 6. The DM2 $K\overline{K}$ mass distributions for the processes a) $J/\psi \rightarrow \gamma K_s K_s$ and b) $J/\psi \rightarrow \gamma K^+ K^-$.

with a region dominated by a spin zero resonance, interference effects can yield non-isotropic angular distributions. A pure spin test would therefore favor spin two over spin zero in this region, since an appropriate superposition of spin two amplitudes having different helicities will, in general, be able to reproduce the observed angular distributions within error.

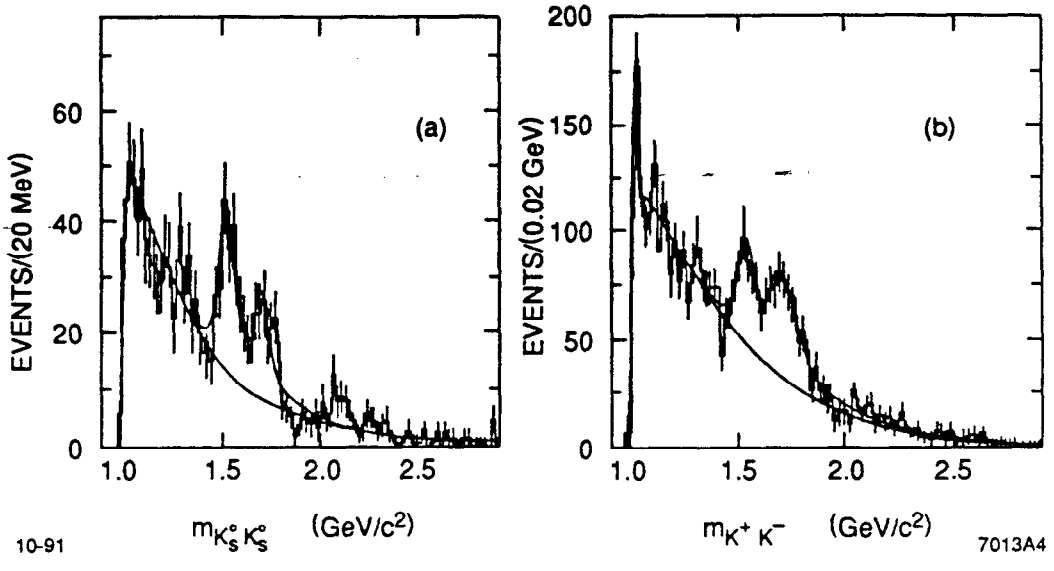

Figure 7. The WA76 $K\overline{K}$ mass distributions for the reactions a) $pp \rightarrow p_f(K_sK_s)p_s$ and b) $pp \rightarrow p_f(K^+K^-)p_s$.

The resonance $\theta(1720)$ is often interpreted[42] as a glueball, because of its production in gluon-rich channels, like J/ψ radiative decay,[37,38,24] (Fig. 1c) and double-Pomeron scattering[40] (Fig. 8b), and its absence in quark-rich channels, such as peripheral production[22] (Fig. 8c) and two-photon collisions[43] (Fig. 8d). It appeared as an extra state for $q\bar{q}$ spectroscopy, since the required two I=0 tensors for the ground state tensor nonet are identified as the well established states, $f_2(1270)$ and $f_2'(1525)$, while the mass of $\theta(1720)$ is considered too light for it to be an excitation tensor state. Explanations of the ratios of the helicity amplitudes of $\theta(1720)$ in these J/ψ radiative decays are also attempted in the context of its glueball interpretation.[42]

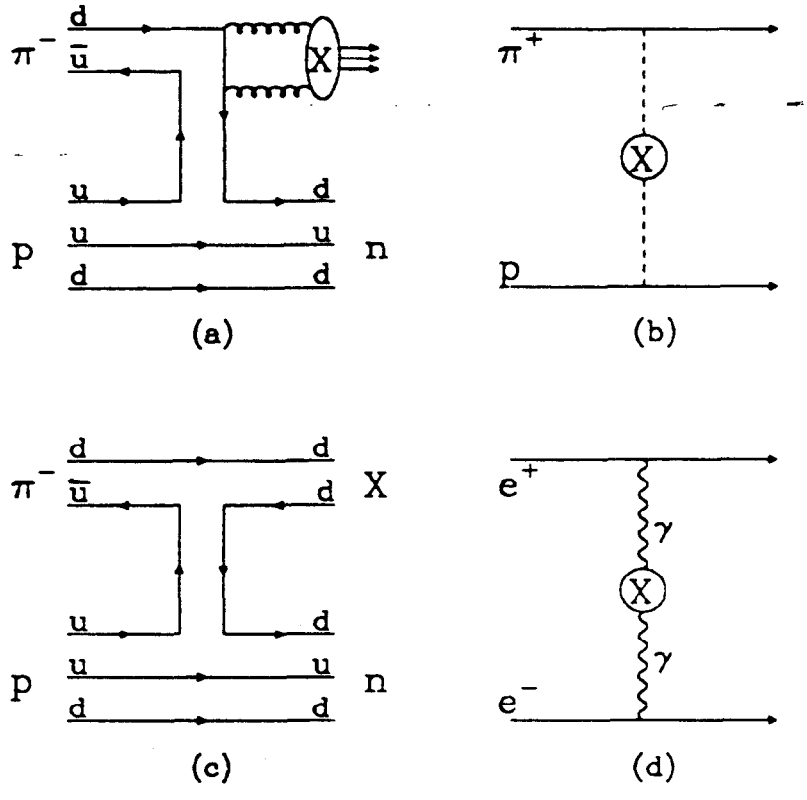

Figure 8. Gluon-rich channels: a) OZI suppressed hadro-production, b) double Pomeron scattering. Quark-rich channels: c) peripheral production, d) two-photon collision.

When its entire J/ψ data sample became available, the MARK III group began an amplitude analysis[39] of the $K\overline{K}, \pi^+\pi^-$ systems, resulting from radiative decay, with simultaneous inclusion of the spin zero and spin two possibilities for the $K\overline{K}$ or $\pi^+\pi^-$ systems. The interaction amplitudes associated with different spin and helicity states of the $K\overline{K}$ or $\pi^+\pi^-$ systems were determined from the

spherical harmonic moments of the event angular distribution of samples in various $K\overline{K}$ or $\pi^+\pi^-$ mass intervals. Preliminary results of that analysis indicated that the events in the $\theta(1720)$ region are associated mainly with a spin zero amplitude, implying that a spin zero intermediate state may exist in this mass region. It follows that the previously reported results, which were obtained on the basis of pure spin hypothesis tests, are called into question. Connections between this possible scalar state and the $f_0/G(1590)$ and $f_0(1750)$, discussed in the previous section, have been the subject of some speculation.[41]

This thesis attempts to define the spin of the $\theta(1720)$ and to advance current knowledge of the other I=0 scalar and tensor mesons in the mass region accessible to the decay modes under study. The current analysis, which concentrates on the $K\overline{K}$ systems, is essentially the same as the one described in Ref. 39, i.e., an amplitude analysis with simultaneous inclusion of the spin zero and spin two possibilities of the $K\overline{K}$ system, which makes use of the whole J/ψ sample of 5.8×10^6 events collected by the MARK III experiment at the SPEAR e^+e^- storage ring at SLAC. This analysis corrects a few minor errors in the moment-amplitude relations of Ref. 39 and takes a technical approach to the analysis of the data which is different from that described in Ref. 39. Consistent amplitude results are obtained with the K_sK_s and K^+K^- data.

Preliminary results of this study, and of a similar one of the $\pi^+\pi^-$ system from J/ψ radiative decay have been reported at various conferences.[44,45] However, the final results for the $\pi\pi$ system will be presented in a separate report. The study of the $\pi^+\pi^-$ system requires a thorough understanding of the

decay $J/\psi \rightarrow \pi^+\pi^-\pi^0$;[46] the latter decay mode results in a large background contribution to the $J/\psi \rightarrow \gamma\pi^+\pi^-$ sample.

Outline of the Thesis

The following chapter describes the MARK III detector, the data production and the detector simulation. Chapter 3 describes the procedures followed in defining the event samples. Chapter 4 describes the amplitude analysis procedure and the results of tests using Monte Carlo samples; detailed derivation of the formalism used in this analysis is contained in the Appendix. Chapter 5 presents the amplitude results obtained with the real data, and reliability tests of these results. Subsequently, Breit-Wigner resonance line shapes are fitted to the distributions of amplitude intensities; Chapter 6 presents the resulting mass, width and branching fractions of the resonances observed, and discusses these results. Chapter 7 concludes this study.

CHAPTER II

APPARATUS

This chapter gives a brief review of the SPEAR storage ring, followed by descriptions of the MARK III detector and its major components. It concludes with summarized descriptions of the J/ψ run history, data samples, and the MARK III Monte Carlo simulation programs.

The SPEAR Storage Ring

SPEAR is an e^+e^- storage ring at the Stanford Linear Accelerator Center (SLAC), which is designed to operate in the 3 to 5 GeV center-of-mass energy range. Construction of this machine was completed in 1972, and it has since performed extraordinarily well. The charmonium family, charmed mesons, the τ lepton and quark jets were discovered or co-discovered at this device. Operation of this machine at the J/ψ production energy yields the data used in the present study. The relevant machine performance characteristics are summarized in Table 2.

The storage ring has a bend radius of $\sim$ 32m. Counter-rotating bunches of positrons and electrons cross in two interaction regions with a characteristic time interval of 781 ns. At $\sqrt{s} = M_{J/\psi}$, the typical bunch density is $\sim 10^{11}$ particles, producing peak luminosities of $5.5 \times 10^{29} cm^{-2} \cdot s^{-1}$. The cross section for $e^+e^- \rightarrow J/\psi$ at the J/ψ peak energy is high. After reduction by a factor of $\sim$ 30 due to the energy spread of the machine, the effective cross section is about

Table 2. Relevant SPEAR properties for J/ψ production

Parameter	Value
Beam Energy	$E_B = 1.5484\ GeV$
Energy Spread	$\sigma_{E_B} = 0.8\ MeV$
Energy Scale Uncertainty	$\delta_{E_B} = 3.1\ MeV$
Peak Luminosity	$\pounds_P = 5.5 \times 10^{29}\ cm^2 \cdot s^{-1}$
Horizontal Beam Size at I.P.	$\sigma_x = 0.7$ mm
Vertical Beam Size at I.P.	$\sigma_y = 0.03$ mm
Longitudinal Beam Size at I.P.	$\sigma_z = 30$ mm
Mean Polarization Time Due to S.R.	$t = 16 - 20$ hours

$2\mu b$. This gives an interaction rate of roughly 1 Hz in the experiment, or, taking into account the typical 50% live time during a run, $\sim 10^6 J/\psi$'s produced per month.

One of the important features of this machine is the small beam size at the interaction point (I.P.), in particular, the small longitudinal bunch length (30mm). This permits high resolution Time-of-Flight techniques to be used in particle identification. In addition, the beams are unpolarized and the transverse polarization induced by synchrotron radiation (S.R.) during a run is negligible, since at SPEAR, for $\sqrt{s} = 3.1$ GeV, the characteristic exponential build-up time for the polarization is typically 16-20 hours, which is much longer than the typical interval between beam fills of 2-3 hours.

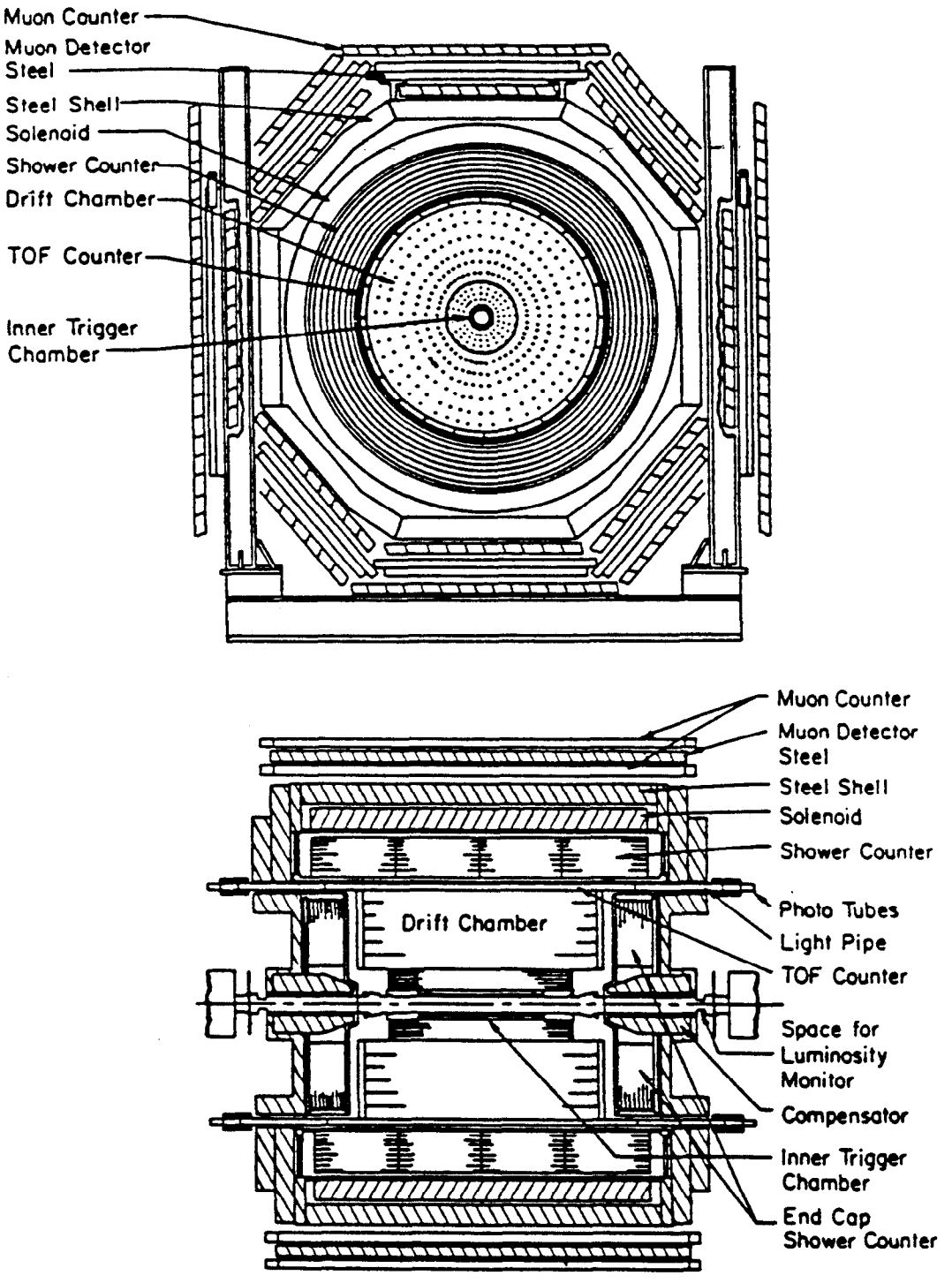

Figure 9. The MARK III detector in axial and transverse views.

The MARK III Detector

The MARK III detector was installed in 1981, and occupies the west interaction region of the SPEAR storage ring. It became the only detector for high energy physics at this machine with the departure of the Crystal Ball detector from the east pit in 1982. The MARK III detector was designed for measurements of exclusive final states in the $\sqrt{s} = 3 - 6\ GeV$ region. Measurements of this kind are possible at these energies due to the low multiplicities of the events and low momenta ($< P > \simeq 500\ MeV/c$) of the tracks. The main requirements for such a detector include:

- high geometrical acceptance for charged particles and photons;
- low material density in the inner part of the detector to minimize multiple scattering of charged particles, and maximize detection efficiency for low energy photons;
- high resolution measurement of the charged track momenta;
- fine segmentation in the photon detector to minimize the shower overlap problem and permit good measurements of photon direction;
- efficient particle identification for charged tracks with momentum $\leq 1 GeV/c$.

These requirements are satisfied by a design based on a scheme of co-axial functional components. The resulting detector is shown in axial and transverse views in Fig. 9. The ordering of the components in increasing radial sequence, is as follows: the beam pipe, trigger chamber, main drift chamber, Time-of-Flight (TOF) counters, electromagnetic calorimeter, magnet coil, magnet flux return and muon counters. Endcap electromagnetic calorimeters are plugged into the

holes around the beam pipe not covered by the above components. The detector and the individual components have been thoroughly described elsewhere;[47-53] in the following, the major components are briefly described.

The Beam Pipe and Trigger Chamber

The innermost components of the detector are the 15cm diameter, 1.5mm thick beryllium beam pipe, and the trigger drift chamber. The particular material and thickness of the beam pipe are chosen to minimize multiple scattering of charged particles and to maintain the vacuum of the storage ring. The trigger chamber, which is referred to as the layer 1 drift chamber in track reconstruction, is shown in an axial view in Fig. 10. It consists of four concentric sub-layers, each containing 32 cells. The cells are offset by half a cell from neighboring sub-layers. Since the gas (70% Ar, 30% ethane) is "fast", i.e. the drift velocity is independent of electric field, and the tracks coming from e^+e^- interactions are nearly radial (because the distances they have traveled are small and the effects of the magnetic field are negligible), the sum of drift times from hits due to these tracks in two adjacent cells in two neighboring sub-layers is approximately constant, T_{sum}, regardless of the position of a track within a cell. This is illustrated in Fig. 10b). With this feature, signals from two adjacent cells in the innermost two layers are fed into a circuit called a *chronotron* that produces a pulse only if the drift times from the two cells add up to T_{sum} to within some tolerance. The output pulse is then gated with the appropriately delayed beam crossing signal to form the lowest lever trigger (referred to as the level-0 trigger in later discussion). This trigger suppresses cosmic ray and beam-gas

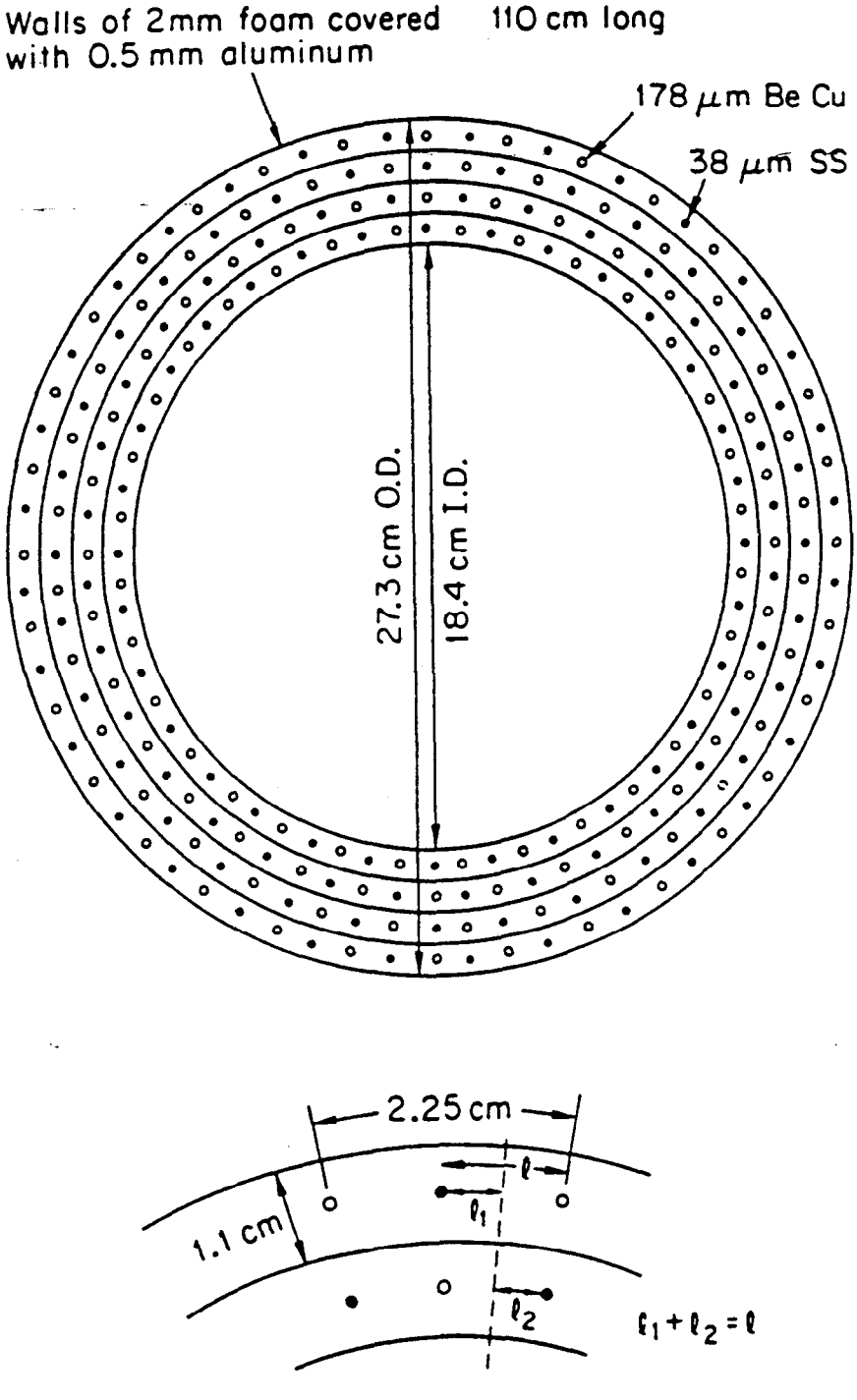

Figure 10. a) Axial view of the trigger drift chamber. b) Axial view of the trigger drift chamber, showing two offset layers.

backgrounds; cosmic ray tracks are usually not radial, so that the drift times in these cells are uncorrelated, while beam-gas events are usually out of time with the beam crossing. In addition, the chamber length was kept small (1.1m), which provides further cosmic ray and beam-gas rejection.

Besides functioning as a trigger device, this chamber provides position measurements for charged particle tracks, and yields a spatial resolution of about 350μm. With the stainless steel sense wires, z-measurements are made by means of charge division.

The Main Drift Chamber

The main drift chamber is also a cylindrical structure, with inner and outer radii of 0.28m and 2.28m, respectively. It consists of two sections sharing a common gas volume. The first section is a region of high density signal wires, collectively called layer 2. The second section is a larger section, which contains layers 3-8. Axial and transverse views of the main drift chamber are shown in Fig. 11.

With respect to the rest of the chamber, layer 2 is shorter in the z-direction to allow space for the field compensating solenoids. This layer consists of 32 cells in azimuth, each containing 13 sense wires and two stainless steel guard wires at the inner and outer radii of each cell. These wires are spaced 1cm apart radially. The dense spacing of wires provides accurate measurement of the tracks, which aids in the reconstruction of secondary vertices from K^0_s and Λ decays. To help resolve the left-right ambiguity of track positions in both sides of a cell from one measured drift time, the sense wires are alternately offset by $\pm 150\mu m$

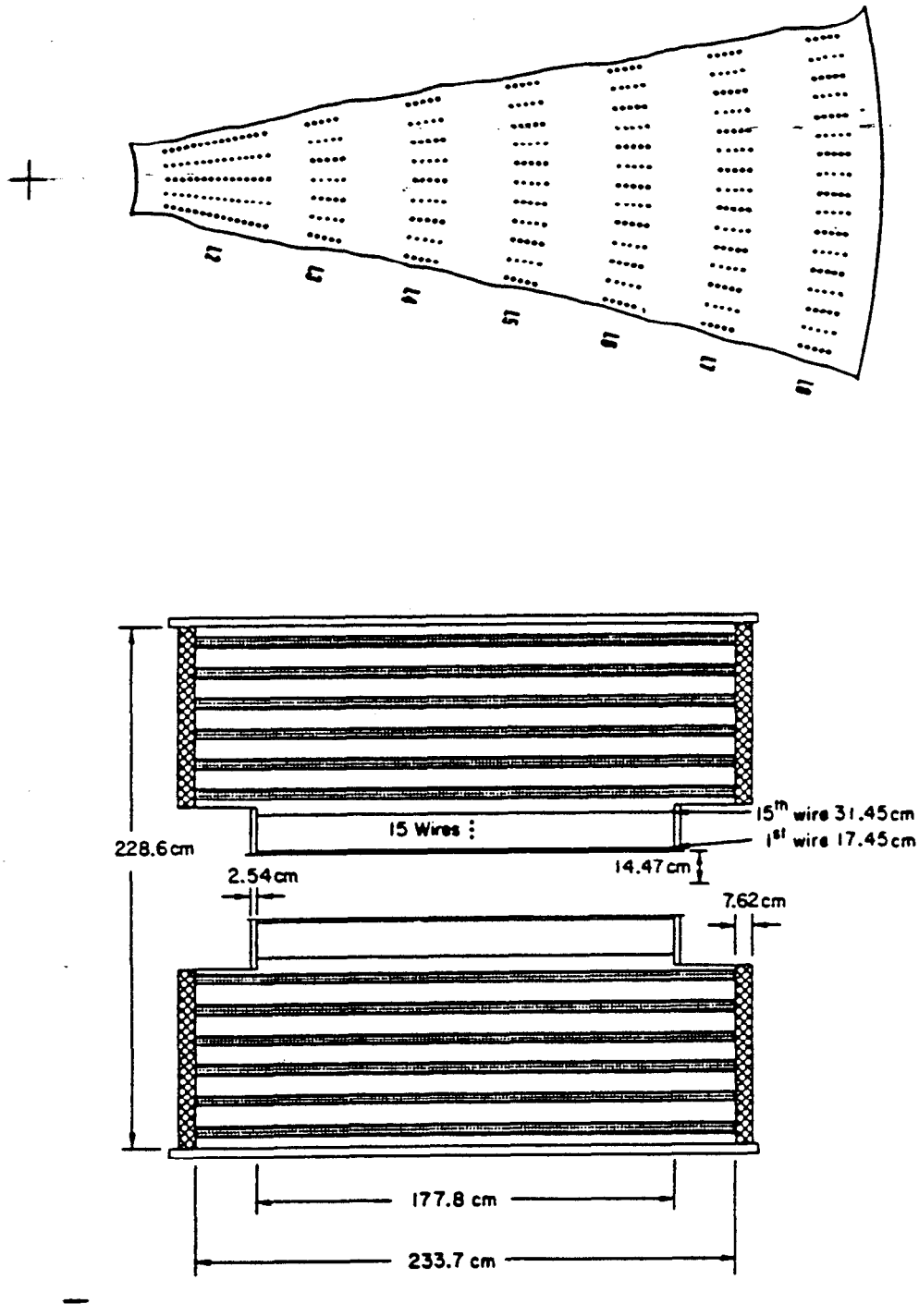

Figure 11. a) Axial and b) transverse views of the main drift chamber.

from the central plane of the cell. The guard wires provide z-measurements by charge division. The operating high voltage of this layer is set low enough so that it operates in proportional mode, and a $\frac{dE}{dx}$ technique can be used for K/π separation at low momentum ($\leq$ 600 MeV/c); however, this technique is not used in the present analysis, since a more powerful technique, namely particle identification with TOF counters, is used.

Layers 3-8 are arranged in small cells. Layer N is at a radius 13.45 $\times$ N cm and contains 16 $\times$ N cells. The cell structure is detailed in Fig. 12. Each cell contains a triplet sense wire configuration, wherein the middle wire of each triplet is offset by 800 μm in ϕ with respect to the other two sense wires, allowing for quick resolution of left-right ambiguities. Stainless steel guard wires again bound each cell at its inner and outer radii, and provide z-measurements by charge division for layers 3, 5 and 7. Layers 4 and 6 are stereo layers, and are used for independent z-position measurements. The field wires are held at about -4.3 kV, while the guard and sense wires are held at ground potential.

The Time of Flight Detector

The Time of Flight system consists of forty-eight 15.6cm wide $\times$ 5.1cm thick $\times$317cm long scintillation counters, mounted lengthwise in a cylindrical configuration on the outside of the main drift chamber, as shown in Fig. 13a). The counters are located at a mean radius of 1.15m from the beam, and cover 80% of the solid angle. Ultraviolet-transmitting light guides, carefully designed to maximize the average photon scattering angle, join the scintillators to photomultiplier tubes located at each end, outside of the magnet iron.

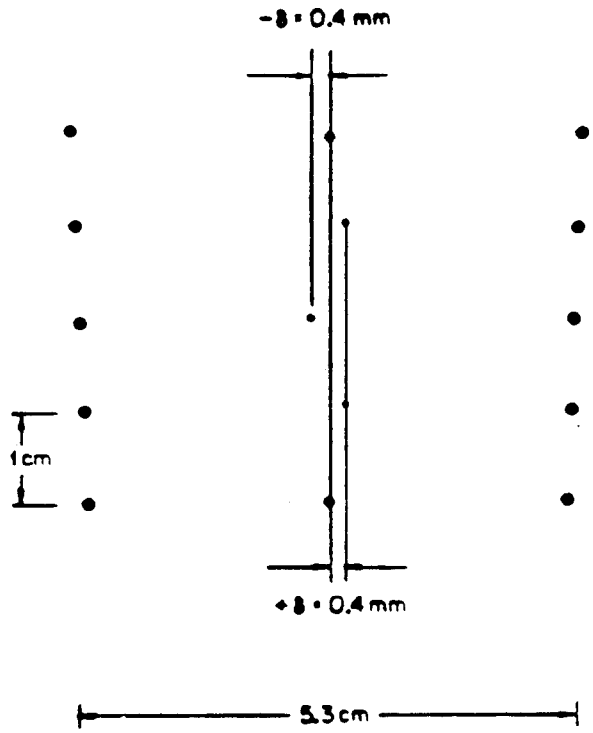

Figure 12. Wire configuration of a cell in layers 3-8 of the main drift chamber.

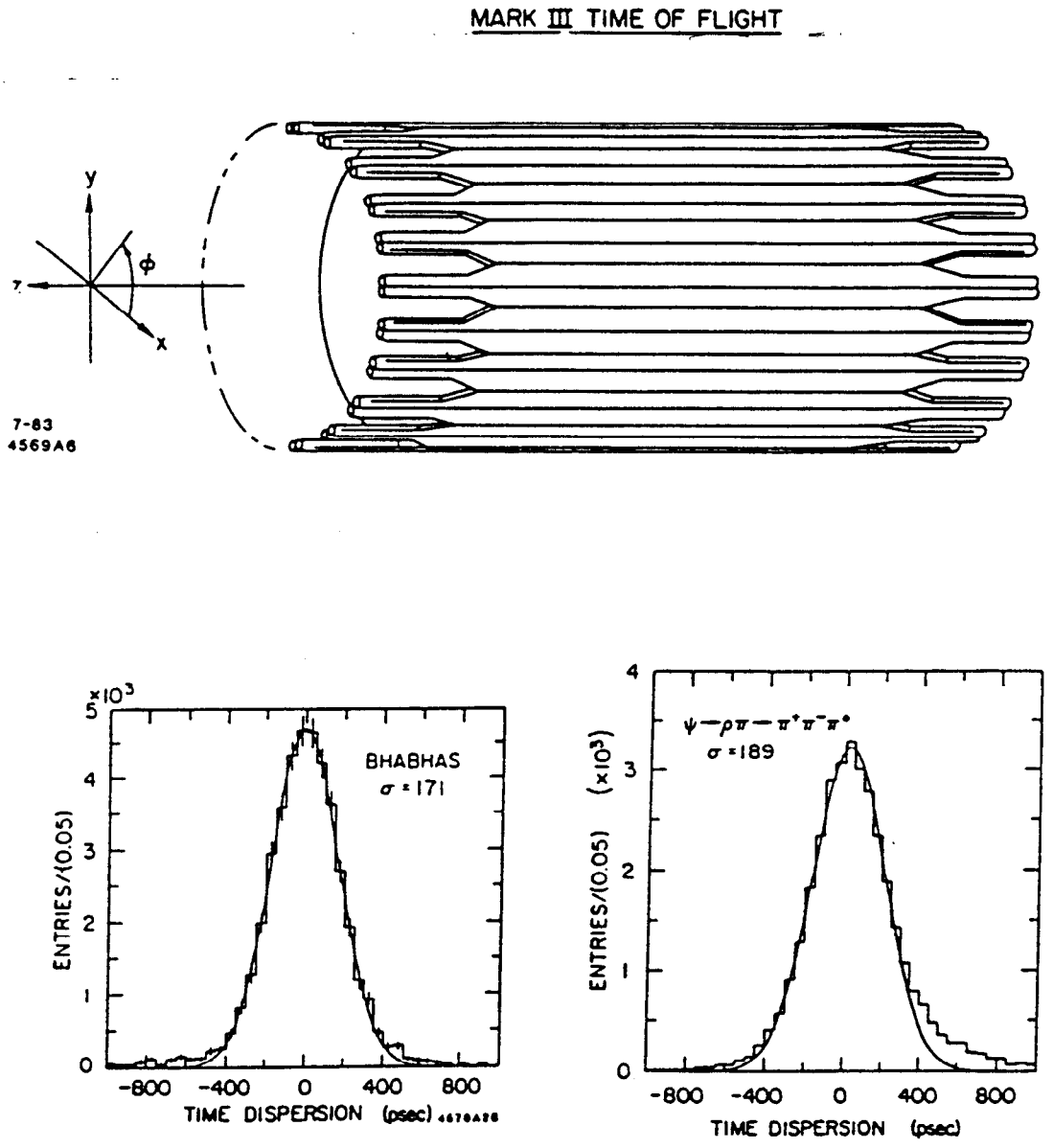

Figure 13. a) Configuration of the TOF counters. b) difference between the measured and predicted time for Bhabha events and for pions from the reaction $J/\psi \to \pi^+\pi^-\pi^0$.

The time information of the photomultiplier pulses is measured at two thresholds simultaneously. The time of flight of a particle is defined as the time measured relative to a beam pick-up signal from SPEAR. The timing electronics are calibrated with a mercury-switch pulser. The zero-time, and the coefficients relating charge and z-position to the measured time, are determined with Bhabha events.

Particle identification by time of flight is based on the relations

$$m^2 = p^2 \left(\frac{1 - \beta^2}{\beta^2} \right), \qquad \beta = \frac{L}{ct},$$

where the momentum, p, and the path length, L, are measured in the drift chambers, and β is determined using the time of flight, t. Quantitatively, TOF identification involves the comparison of the measured time, and the flight time predicted on the basis of the measured momentum and a given mass hypothesis. The difference of these two quantities is measured in terms of the corresponding timing resolution.

When the system was first brought up in 1982, timing resolutions of 171 ps and 189 ps were obtained for electrons from Bhabha events, and hadrons from hadronic events, respectively; Fig. 13b) shows the measured time dispersion for these two cases. Roughly 80% of the resolution smear is intrinsic to the counters, photomultipliers and electronics. The rest is attributed to contributions from tracking errors in the drift chambers, and jitter in the time information of beam crossing. Hadronic events are more affected by tracking errors than di-lepton events. By 1985, the overall time dispersion was about 10% worse than in 1982,

a degradation attributable to radiation damage to the scintillators, and the 1985 increase in the SPEAR bunch length.

The TOF system provides the most powerful means of particle identification in the MARK III detector. Pions and kaons are separated at the 3σ level up to 800 MeV/c, and at the 2σ level up to 1 GeV/c. This is illustrated by the plot of β versus p, shown in Fig. 14.

The Electromagnetic Calorimeter

The electromagnetic calorimeter consists of three sections of shower counters: a cylindrical barrel shower counter that covers 76% of the solid angle, and two endcap counters that extend the solid angle coverage down to about 10^o from the beam. Combined, the electromagnetic calorimeter covers about 94% of the solid angle.

The barrel and endcap shower counters have a similar design, and consist of 24 parallel layers of rectangular proportional tubes, interleaved with 23 sheets of 0.5 radiation-length-thick lead-antimony alloy. In the barrel, the proportional tubes are aligned in the z-direction, while in the endcaps they are aligned perpendicular to this direction. Each tube contains a single 46μm stainless steel sense wire maintained at 2kV. Charge division is used to measure the shower coordinate along the wire. Both systems use a gas mixture of 80% argon and 20% methane. In the barrel, there are 320 cells arranged in azimuth for each layer, and in the endcaps there are 146 cells in total for each layer.

In order to maximize the efficiency for detecting low energy photons, the barrel shower counter is located inside the magnetic coil. Mechanically, it is

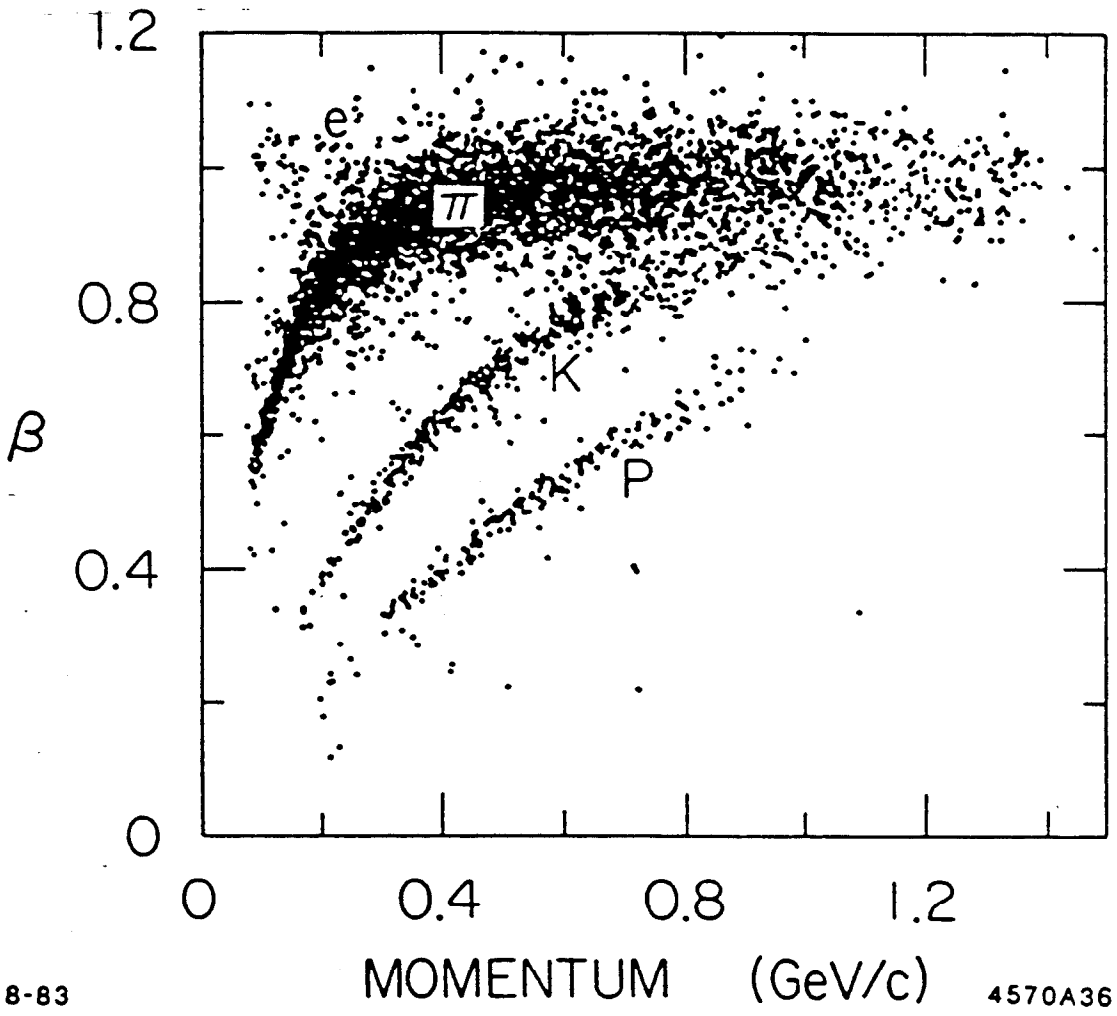

Figure 14. Scatterplot of β versus momentum showing e, π, and P bands.

constructed on a 23mm thick aluminum spool, which is 3.85m long and 2.52m in diameter. The spool and TOF counters account for roughly 0.4 radiation length of material before the first layer of proportional tubes. To support the lead-antimony sheets, five equally spaced aluminum bands 1.27cm tall (radially) and 2.67cm wide (axially) are used in each layer. These "ribs" unfortunately create small dead regions.

In both the barrel and the endcaps, the first six layers are read out individually at both ends, thus allowing coordinate determination along the tube as well as pulse height measurement. Wires in the last 18 layers are combined in groups of three in depth and again are read out at both ends. This reduces the number of electronics channels while preserving the full information from the inner layers, where the showers from low-energy photons are usually confined.

Position resolution parallel and transverse to the wire direction is measured using Bhabha electrons and muon pairs. Energy resolution is studied using Bhabha events in the high energy region, and photons from decay $J/\psi \rightarrow \pi^+\pi^-\pi^0, \pi^0 \rightarrow \gamma\gamma$ in the lower energy region. The position and energy resolution for the barrel and endcap counters are summarized in Table 3.

Table 3. Shower counter resolution.

Measurement	Barrel counters	Endcap counters
Energy resolution	$\sigma_E = 17.5\% \times \sqrt{E(GeV)}$	$\sigma_E = 17.0\% \times \sqrt{E(GeV)}$
Longitudinal resolution	$\sigma = 0.8\% \times$ (wire length)	$\sigma = 1.0\% \times$ (wire length)
Transverse resolution	$\delta_\phi = 7$ mrad	$\delta_\phi = 7$ mrad

The energy resolution is attributed to the fluctuations in energy loss in the gas, the transverse resolution is determined by the cell size, and the longitudinal resolution is the charge division resolution.

The efficiency of photon detection is plotted in Fig. 15a), and is determined using a large sample of $J/\psi \rightarrow \pi^+\pi^-\pi^0, \pi^0 \rightarrow \gamma\gamma$ events. With the momenta of the two charged pions measured with the drift chambers, and the momentum direction of one photon measured with the shower counters, the energy and momentum direction of the second photon are predictable. The efficiency at a given photon energy is determined as the ratio of the number of found photons divided by the total number of predicted photons at the given energy. A comparison of the measured and predicted energy of the second photon is given in Fig. 15b), which shows that the data scale linearly down to photon energies of about 50 MeV.

Beyond the shower counters is the solenoid, which provides a magnetic field strength of 0.4T at the center of the detector. The flux return of the solenoid, along with the shower counter, serve as hadron absorbers for the muon detectors.

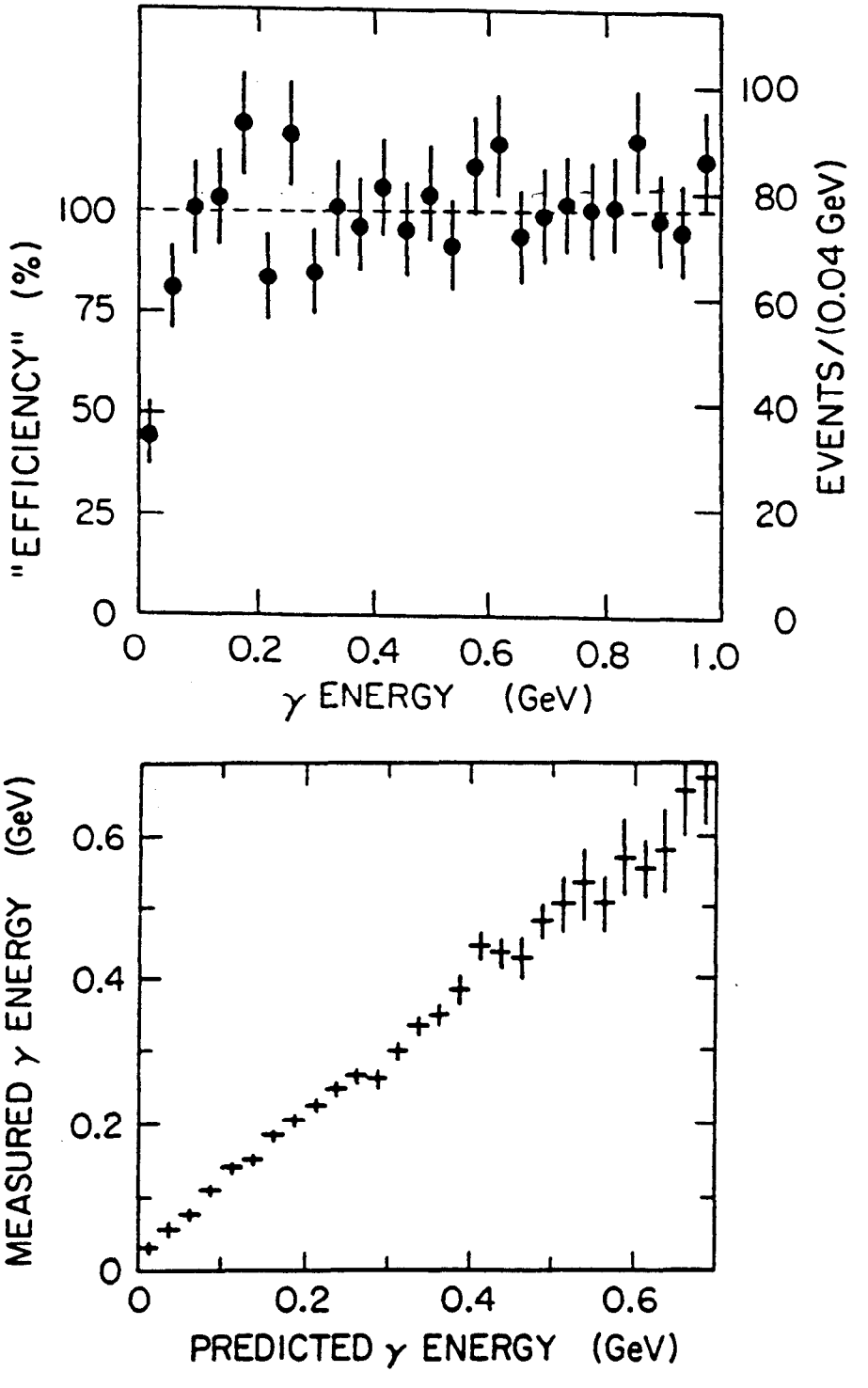

Figure 15. Shower counter performance based on a study of $J/\psi \rightarrow \pi^+\pi^-\pi^0, \pi^0 \rightarrow \gamma\gamma$ events; a) detection efficiency versus photon energy, b) predicted versus measured photon energy.

The Muon Detector

The muon detector system consists of 1080 proportional tubes, grouped together in modules of 16, and arrayed in a two-layer octagonal pattern around the outside of the magnet iron. The two layers of muon tubes are separated by 21cm of steel. This configuration helps to suppress pion and kaon punch-through, since it is highly unlikely that a hadron that fails to interact before the first layer will also make it through the second. The proportional tubes are 5cm in radius and 4.2m long. The azimuthal segmentation is adequate, since charged tracks reaching the muon counters have already suffered considerable multiple scattering. The z-position of tracks is determined by charge division to an accuracy of 6cm.

The solid angle coverage of the muon detector system is 60% of 4π. This system is fully efficient for muons with momentum greater than 1 GeV/c, and completely inefficient for muons with momentum less than 600 MeV/c. For the analysis presented here, the system is used to reject muons only; it is nonetheless important to know the probability for π's and K's to punch-through to the muon counters, so that detection efficiencies for these particles can be correctly calculated. The punch-through effect has been carefully studied and incorporated in all detector simulations.

The Event Trigger

The MARK III trigger is based on the idea of finding charged particle track trajectories in the drift chambers using fast pattern recognition electronics. Two triggers operated in parallel for the J/ψ data: a "one track" and a "two track"

trigger. As their names suggest, these triggers correspond to finding one or two charged particle track candidates in the event in question.

The beam crossing interval at SPEAR (780 ns) is much shorter than the time required to process and log an event to tape (30 ms). To minimize dead time, the triggers are divided into two levels of complexity, called "level-0" and "level-1". The level-0 trigger, which requires less than one beam crossing time to make a decision, uses information from the trigger chamber, as described earlier, and the TOF counters. The one and two track triggers require one and two layer 1 chronotron hits respectively. The TOF information is needed for the one track trigger only in order to suppress beam-gas events; a TOF counter hit, which is in-time with the beam crossing, is required. If neither trigger is satisfied at level-0, a reset signal is issued to the detector electronics 590 ns after the beam crossing, giving the capacitors used in sample-and-hold electronics enough time to discharge. Otherwise, the reset signal is inhibited to allow time for the level-1 decision to be made.

The level-1 trigger, which requires two beam crossing intervals to make a decision, identifies patterns of hit cells in layers 1, 3 and 5 with physical track trajectories in the $r - \phi$ plane. For the purpose of the trigger, a hit cell in layer 1 means a chronotron hit, while that in layer 3 or 5 means that 2 or 3 wires in a cell produce signals. For each hit cell in layer 5, there are a number of combinations of layer 1 and layer 3 hit cells that correspond to real tracks with a certain minimum transverse momentum. These combinations are searched quickly, through the use of programmable array logic, and compared with the

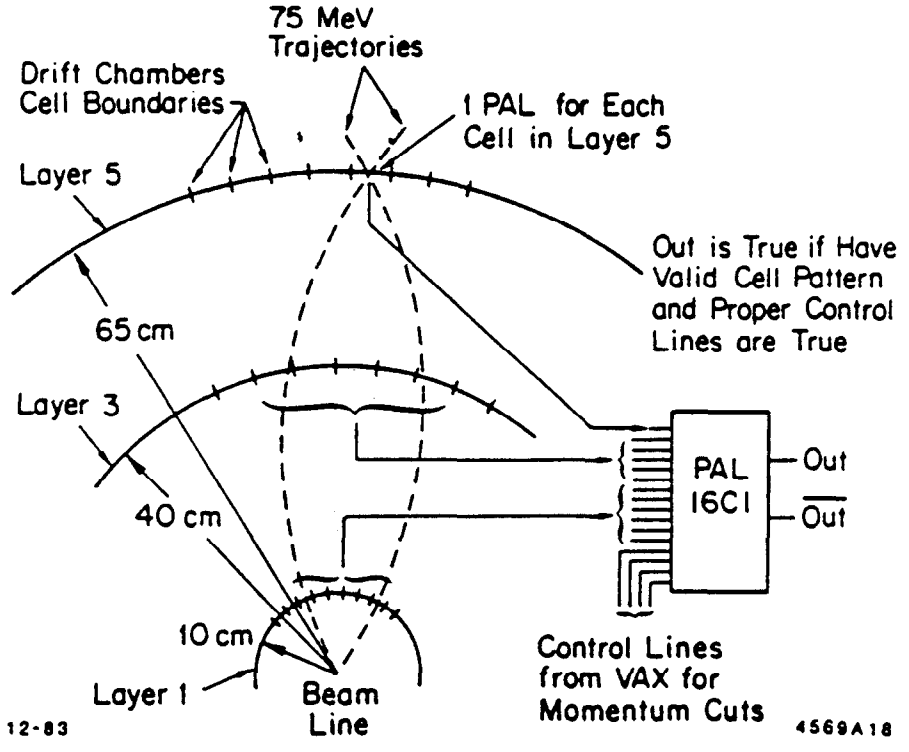

Figure 16. Schematic of the level-1 trigger.

signal hit cell pattern, as illustrated in Fig. 16. An interrupt signal to the computer for data log is generated if the level-1 trigger logic is satisfied.

The level-0 trigger rate is 2-3 kHz and is mostly due to beam-gas events and X-rays from scattered synchrotron radiation. The level-1 trigger rate is 2-3 Hz and is a roughly equal mixture of cosmic ray, beam-gas, and e^+e^- events at the J/ψ beam energy. The trigger results in $\sim 10\%$ dead time under typical running conditions. Its efficiency was measured in 1982 by using a sample of $\psi(3685)$ events. The $\psi(3685)$ decays to $\pi^+\pi^- J/\psi$ 50% of the time. This allows one to "tag" the J/ψ using the two pions, and then to see how many times the J/ψ products would have triggered the detector. The measured efficiency for the J/ψ is 93%.

Data Reduction

Events satisfying trigger-1 were logged onto magnetic tape by an on-line VAX 11/780 computer. At the end of each shift, tapes filled during that shift were taken to the SLAC computer center for processing on the IBM mainframe. To save computer time, events were first run through a fast filter program, which uses information from the shower counters and TOF counters to further remove cosmic ray and beam-gas events. The filter reduced the event sample by a factor of 70%, while removing only 0.5% of real hadronic events. Events passing the filter were then passed to the reconstruction program, which converted raw time and pulse height measurements into momentum vectors, energy and particle identification quantities. Accurate reconstruction requires a large number of calibration constants, and since these constants vary with time, they were

obtained for each data set separately. For this reason, it was necessary to make two or more passes through the data. The first pass was used to obtain the calibration constants, and to check for gross mistakes in the data. The second pass was used to reconstruct the events using the constants from the first pass, and to produce the best measurements of the track 4-momenta. Fully reconstructed events were then sorted into sub-sets according to charged-prong count and compressed into Data Summary Tapes (DSTs), which were then used for the physics analysis. To set the scale, the 2-prong J/ψ sample consists of ~ 175 raw data tapes; the DST program reduced this number to 17 tapes.

The J/ψ Run History

The MARK III J/ψ data sample, corresponding to 5.8×10^6 produced J/ψ's, was collected in blocks of 0.9×10^6, 1.8×10^6, and 3.1×10^6 in 1982, 1983 and 1985 runs respectively. The number for the 1983 run was determined on the basis of a visual scan of the events collected in that run, and the J/ψ detection efficiency was obtained using a separate $\psi(3685) \rightarrow \pi^+\pi^- J/\psi$ sample. The sizes of the other two runs were determined by scaling by the ratio of the number of $J/\psi \rightarrow \mu^+\mu^-$ events in each data set, to the corresponding number in the 1983 data set. The overall uncertainty in the total number of J/ψ's is 8.5%.

Monte Carlo Simulation

Monte Carlo simulation programs are essential for calculating acceptance and efficiency corrections, and for estimating backgrounds. The MARK III Monte Carlo programs can be divided into two pieces. The first, the event generator, produces track 4-momentum vectors according to some pre-defined

kinematic models for the specified J/ψ decay modes. It is also responsible for taking into account of decays of the J/ψ decay products. The second part simulates the response of the detector to charged tracks and photons. Energy loss, multiple Coulomb scattering and nuclear interactions in the detector material are taken into account, as is the variation of detector efficiency and resolution with run period.

The drift chamber simulation is very accurate, because track trajectories are constructed using a high density of drift time measurements which individually have nearly Gaussian resolution. The TOF counters are well-modeled also. The shower counters are the most difficult components to simulate, because the electromagnetic showers have energy and shape distributions that are non-Gaussian, especially at low energies. An additional complication arises from the dead regions due to the barrel support structure, and to the gaps separating the barrel from the endcaps. Finally, the high πN and KN cross sections in the calorimeter at low energy inevitably result in extra photons in the events.

To simulate the shower counters well, the MARK-III Monte Carlo program has three options for shower generation. The oldest package, called FAKSHR, creates showers based on phenomenological shower shapes and energy distributions, and is tuned on a subset of $J/\psi \to \pi^+\pi^-\pi^0$ events. This package is found to model the data well when photons of energy greater than 100 MeV are involved. Another package used is the MARK III adaptation of EGS3,[54] which is in principle more accurate because of its emphasis on minute details, but is often prohibitively slow. The third generator, called ELSHWR, utilizes a library of photon showers taken from real $J/\psi \to \pi^+\pi^-\pi^0$ events. This package

is considered an effective compromise between FAKSHR and EGS3, in that it provides fairly accurate shower simulation without creating an intense computational burden. On the average, efficiency calculations from the three generators agree to within 5%. Since none of these shower generators includes πN and K N interactions, MARK III physics analyses normally make no stringent requirements on the number of photons in a particular event.

CHAPTER III

EVENT SELECTION

The event selection for the J/ψ decay modes, $J/\psi \rightarrow \gamma\ K_s K_s$ and $J/\psi \rightarrow \gamma\ K^+K^-$ is described in this chapter. The data sample used in the present analysis is from the MARK III 1982, 1983 and 1985 J/ψ data runs; this corresponds to 5.8×10^6 J/ψ events.

The procedures described are based on those applied in previous MARK-III analyses.[38,39,19] The quality of the resulting data samples is discussed in detail in the following sections.

Selection of the $J/\psi \rightarrow \gamma\ K_s K_s$Events

The K_s mesons in the event are identified through the decay $K_s \rightarrow \pi^+\pi^-$. The preliminary selection criteria for $J/\psi \rightarrow \gamma\ K_s K_s$ events are as follows:

1. each event has four charged tracks, with net charge zero.
2. each event has at least one neutral shower.
3. each charged track has a good helix fit, which is such that the corresponding error matrix is of good quality, and can thus be used in fit to the event as a whole.
4. the four charged tracks can be grouped into two pairs, each having two oppositely charged tracks with an acceptable distance of closest approach, and having invariant mass within 50 MeV/c^2 of that of the K_s, when each track is assigned the mass of the pion.

When the invariant mass of each track pair, denoted as $M_{\pi^+\pi^-}(1)$ or $M_{\pi^+\pi^-}(2)$, is calculated, the momentum vectors of the charged tracks are specified at the point of closest approach. These momentum vectors are also utilized for the kinematic fit to the event, together with the parameters of the neutral shower which has the highest energy deposit in the shower counters. The kinematic fit requires that the total momentum and energy of the final state particles be consistent with those of the J/ψ produced at rest; a confidence level of at least 1% for the fit to the hypothesis of $J/\psi \rightarrow \gamma\pi^+\pi^-\pi^+\pi^-$ is required in order that the event be considered an acceptable candidate.

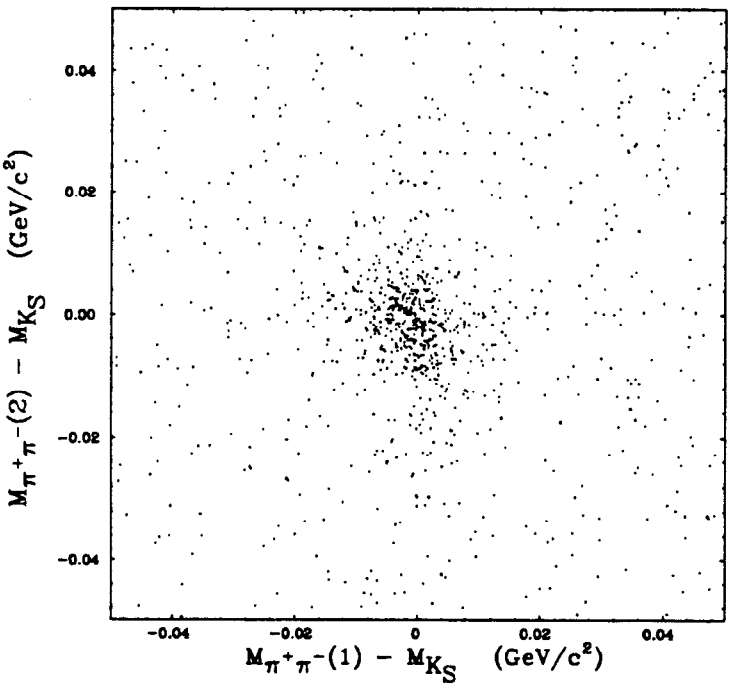

Figure 17. $M_{\pi^+\pi^-}(1) - M_{K_s}$ versus $M_{\pi^+\pi^-}(2) - M_{K_s}$ for the events which are candidates for reaction $J/\psi \rightarrow \gamma\, K_sK_s$ after the preliminary selection and kinematic fit criteria have been applied.

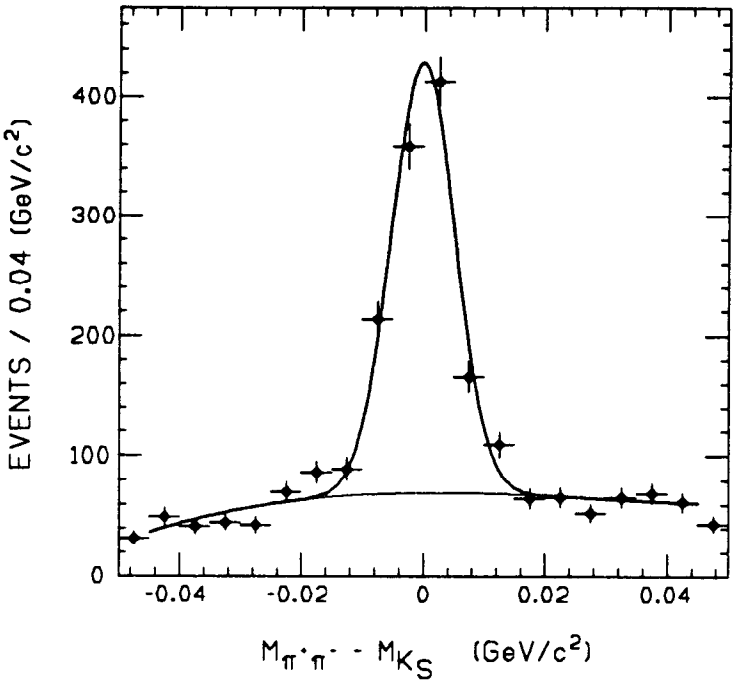

Figure 18. The $M_{\pi^+\pi^-}$ distribution of both pion pairs after the preliminary selection and kinematic fit criteria have been applied. The smooth curve corresponds to the fit of a Gaussian line shape and a polynomial background term to the data.

The mass of one charged track pair versus that of the other is plotted in Fig.17 for the events which pass the preliminary selection and kinematic fit criteria. The mass distribution of both charged track pairs is plotted as the data points in Fig. 18. The smooth curve in Fig.18 corresponds to the fit of a Gaussian line shape and a polynomial background term to the data. The mass of K_s from the fit is $496.8 \pm 0.3 MeV/c^2$.† The width of the Gaussian is

† The fitted value of the K_s mass becomes $497.6 \pm 0.3 MeV/c^2$, when the dE/dX energy losses for the charged tracks are taken into account. This is consistent with the world average measured value, namely $497.671 \pm 0.031 MeV/c^2$.[2]

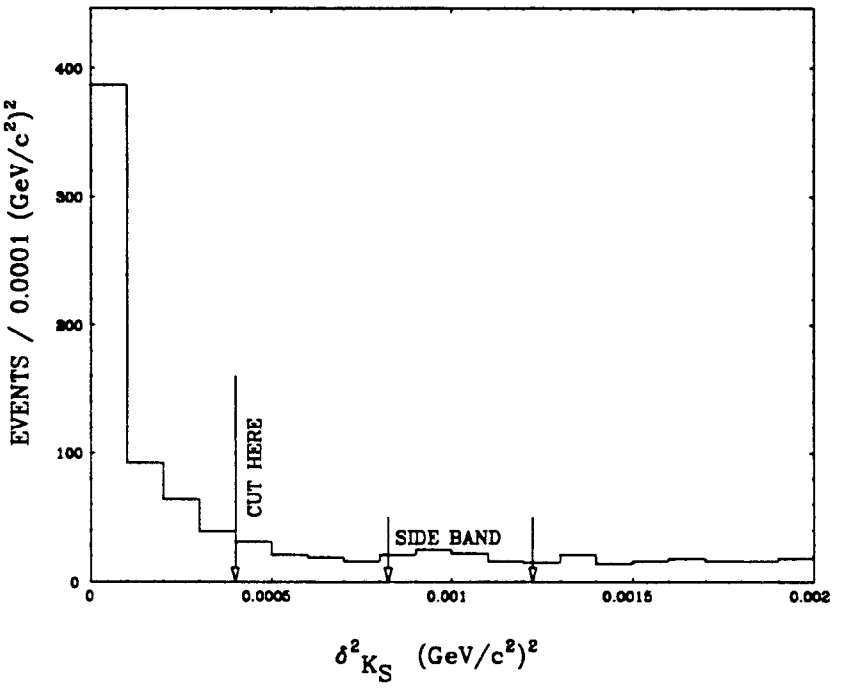

Figure 19. Distribution of the $\delta^2_{K_s}$ of the events after the preliminary cut. The arrows mark the final cut applied on this quantity, and the side band within which the events are taken to estimate the background contribution.

$4.7 \pm 0.3 MeV/c^2$, which is thus the mass resolution at the K_s mass.

The distribution of the quantity

$$\delta^2_{K_s} = (M_{\pi^+\pi^-}(1) - M_{K_s})^2 + (M_{\pi^+\pi^-}(2) - M_{K_s})^2$$

is shown in Fig. 19. Signal events are further required to satisfy $\delta^2_{K_s} < (20 MeV/c^2)^2$. The K_sK_s mass distribution after this requirement is shown as the solid histogram in Fig. 20. The dotted histogram in Fig. 20 is an estimation of the background events in the selected sample. This is obtained by selecting events which satisfy $(28.7 MeV/c^2)^2 < \delta^2_{K_s} < (35 MeV/c^2)^2$, (the region marked as the side band in Fig. 19), this corresponds to an area in Fig. 17 which is

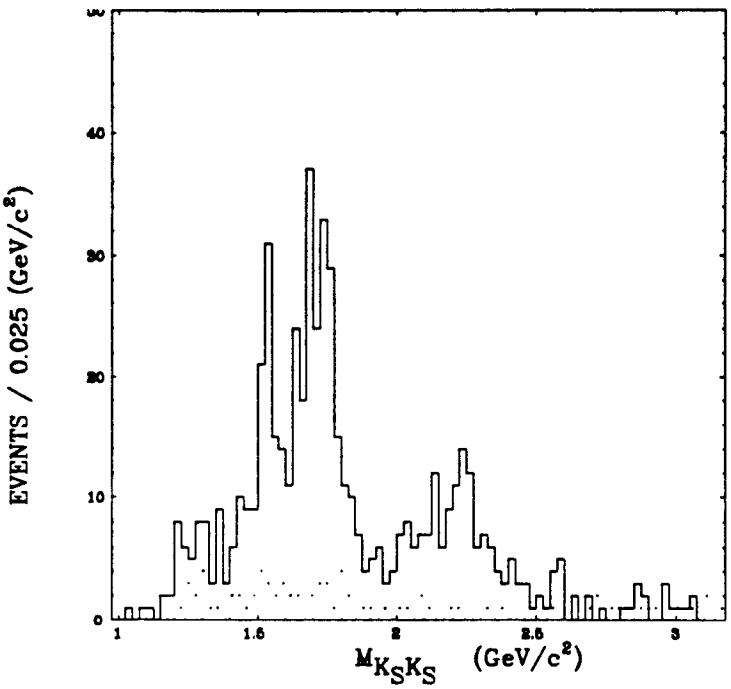

Figure 20. The $K_s K_s$ mass distribution after all cuts. The solid histogram is for the selected sample; the dotted histogram corresponds to the estimated background.

equal to that of the selected analysis sample; this equal-area-selection provides a properly normalized background estimation. In Fig. 20, there are 582 selected events and 80 background events. Since the number of background events is relatively small (14%), and no resonant structure is evident in the background distribution, the effect of the background events on the results of the amplitude analysis is small; consequently, no background subtraction procedure is carried out.

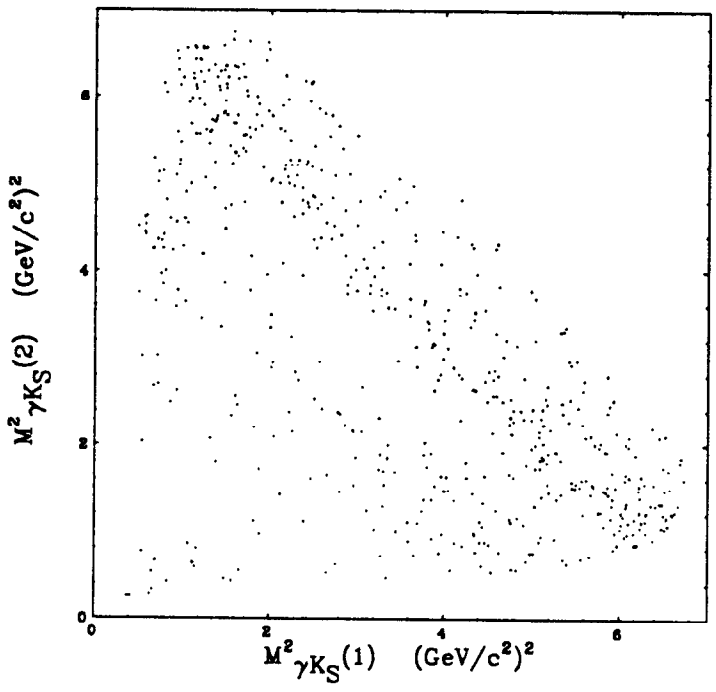

Figure 21. The Dalitz plot for the $J/\psi \to \gamma\ K_s K_s$ sample.

From Monte Carlo studies[39] , it is determined that the background events result from the following decay modes:

$$J/\psi \to \pi^0\pi^+\pi^-\pi^+\pi^-$$

$$J/\psi \to \gamma\pi^+\pi^-\pi^+\pi^-$$

$$J/\psi \to \pi^0 K_s^0 K^{\pm}\pi^{\mp}$$

$$J/\psi \to \gamma K_s^0 K^{\pm}\pi^{\mp}$$

$$J/\psi \to \gamma\pi^0 K_s^0 K_s^0$$

$$J/\psi \to K_L^0 K_s^0 \pi^+\pi^-$$

None of these modes dominates, and each contributes only a few events to the overall background.

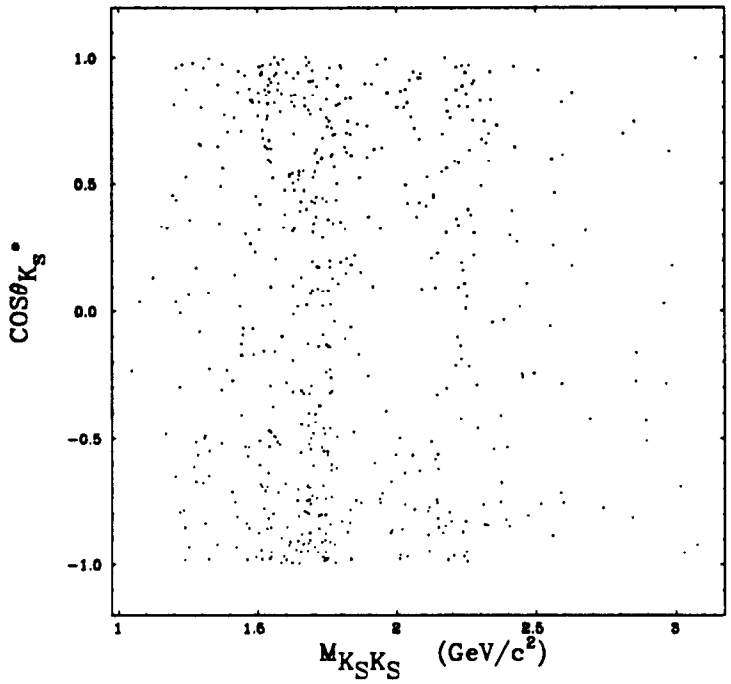

Figure 22. The scatter plot of K_sK_s mass versus $\cos\theta^*_{K_s}$ for the $J/\psi \to \gamma K_sK_s$ sample.

In Fig. 20, resonant structures are apparent in the mass regions of the $f_2'(1525)$ and $\theta(1720)$. They appear as the outer-most diagonal bands in the Dalitz plot of Fig. 21. An equivalent way of displaying the events is to plot $M_{K_sK_s}$ vs $\cos\theta^*_{K_s}$, where $\theta^*_{K_s}$ is the polar angle of one of the K_s's (chosen at random) in the rest frame of the K_sK_s system (the coordinate systems defined in this analysis are described in the Appendix). This is shown in Fig. 22. The resonant structures appear as vertical bands at the appropriate $M_{K_sK_s}$. The differing $\cos\theta^*_{K_s}$ distributions in different bands are readily apparent. The distribution in the $f_2'(1525)$ band is significantly enhanced near $\cos\theta^*_{K_s} = \pm 1$, while that in the $\theta(1720)$ band appears more uniformly distributed over $\cos\theta^*_{K_s}$. It

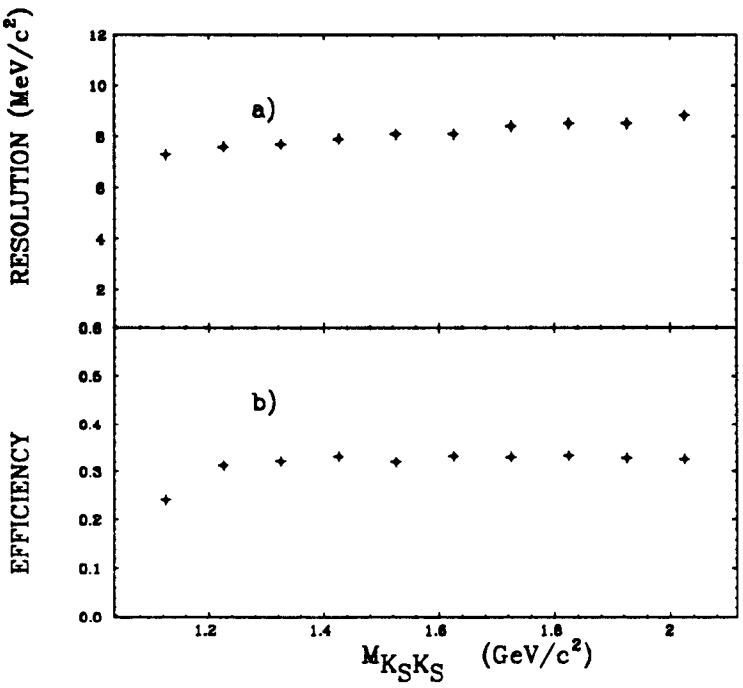

Figure 23. a) The K_sK_s mass resolution, and b) the mean $J/\psi \rightarrow \gamma$ K_sK_s detection efficiency as a function of the K_sK_s mass.

should be noted that a uniform distribution in $\cos\theta^*_{K_s}$ is one of the characteristics of a spin 0 resonance.

Since resonances with spin higher than 2 are possible in the region $M_{K_sK_s} > 2GeV/c^2$, a complete amplitude analysis would have to incorporate many spin and helicity states. However, the number of events in this region is small, and, as a result, no reliable amplitude analysis can be carried out with the available statistics. Therefore, the present study will cover only the region $M_{K_sK_s} < 2GeV/c^2$. The events having $M_{K_sK_s} > 2GeV/c^2$ (cf., Figs. 20, 21 and 22) are considered beyond the scope of this work.

The mass resolution for $J/\psi \rightarrow \gamma\, K_sK_s$ events with K_sK_s mass less than 2 GeV/c^2 is shown in Fig.23 a), and their detection efficiency shown in Fig.23 b).

These estimations are made by means of Monte Carlo studies in which the generated events are uniformly distributed in K_sK_s mass and the event angles. As a function of the K_sK_s mass, the mass resolution varies from $7MeV/c^2$ at threshold to 9 MeV/c^2 at $M_{K_sK_s} = 2GeV/c^2$. The mean detection efficiency increases from threshold to a value of $\sim$ 32% at 1.2 GeV/c^2, and thereafter remains approximately constant up to 2 GeV/c^2. Its dependence upon the event angles will be discussed in chapter IV.

Selection of the $J/\psi \rightarrow \gamma K^+K^-$ Events

The preliminary criteria for the selection of $J/\psi \rightarrow \gamma\ K^+K^-$ events are similar to those used for $J/\psi \rightarrow \gamma\ K_sK_s$ selection. They are as follows:

1. each event has two charged tracks, with net charge zero.
2. each event has at least one neutral shower.
3. each charged track has a good helix fit, which is such that the corresponding error matrix is of good quality, and can thus be used in a kinematic fit to the event as a whole.

Additional cuts are applied for the purpose of further background suppression. These are divided into two categories, namely, the intermediate cuts and the final cuts, according to the order of their application. The intermediate cuts select events which are good candidates for radiative decay, but preferentially exclude radiative di-lepton events. These are as follows:

4. cuts on the following quantities.[55] These select events which are kinematically consistent with a radiative decay.

$$|U| = |(E_{miss} - |\vec{P}_{miss}|)| \leq 0.4GeV$$
$$P_{tr}^2 = 4 \cdot |\vec{P}_{miss}|^2 \cdot \sin^2 \frac{\theta_{miss}}{2} \leq 0.005(GeV/c)^2$$

   where E_{miss} and $\vec{P}_{miss}$ are the missing energy and momentum calculated using the measured charged particle momenta only; θ_{miss} is the angle between the missing momentum vector and the measured direction of the neutral shower.

5. neither charged track deposits more than 1.0 GeV of energy in the shower counters; this suppresses radiative Bhabha events.
6. neither charged track is registered in the muon counters; this reduces $\gamma\mu^+\mu^-$ events.
7. the charged tracks are required accollinear by at least 5.7^o ($\cos\theta_{1,2} \geq -0.995$); this further suppresses radiative di-lepton events.

The events surviving the above selection criteria are subject to a kinematic fit, which requires the total momentum and energy of the final state particles to be consistent with those of a J/ψ particle produced at rest. A confidence level of at least 2% for the fit to the hypothesis $J/\psi \rightarrow \gamma K^+K^-$ is required. The K^+K^- mass spectrum after these selection criteria is shown in Fig. 24.

The final cuts are employed in order to suppress background events from the channels $J/\psi \rightarrow \pi^0K^+K^-$, $J/\psi \rightarrow \pi^0\pi^+\pi^-$, $J/\psi \rightarrow \gamma\pi^+\pi^-$, and also to suppress any residual contribution from radiative di-lepton events. In order to

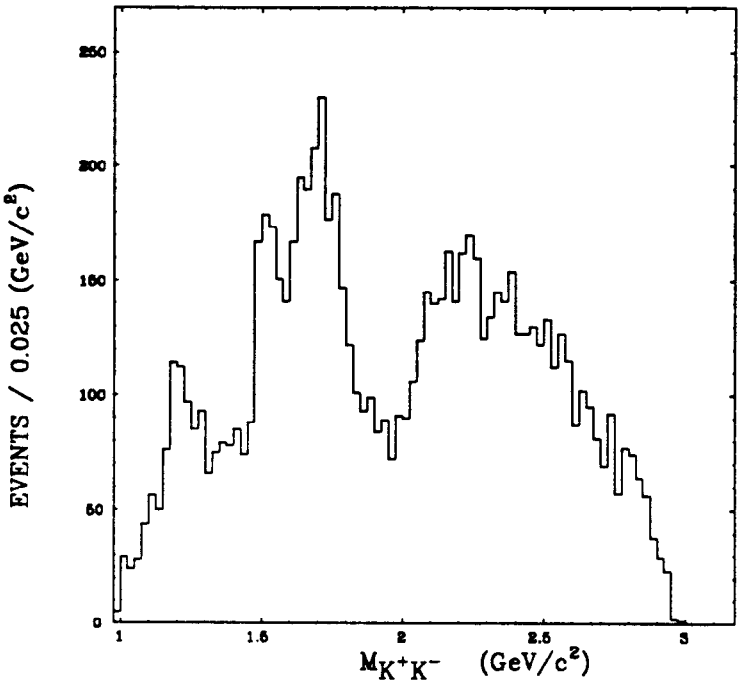

Figure 24. The K^+K^-mass distribution for the $J/\psi \rightarrow \gamma\ K^+K^-$sample after the intermediate cuts and the kinematic fit.

reduce the $J/\psi \rightarrow \pi^0 K^+K^-$, $J/\psi \rightarrow \pi^0\pi^+\pi^-$ contamination, all events surviving the cuts above are kinematically fit to these hypotheses, using the two charged tracks, the neutral shower which has the highest energy, and one of the other showers in the event. An event is rejected if there is at least one neutral shower pair, described above, having its invariant mass within $50MeV/c^2$ of the π^0 mass, and if the confidence level of the overall fit is greater than 5%. To reduce background contributions from $J/\psi \rightarrow \gamma\pi^+\pi^-$ and any residual radiative di-lepton events, the charged tracks are subject to particle identification requirements based on TOF information. Each charged track must be detected by the TOF counters, the hypothesis for it to be a kaon must be preferred over that for it to be a pion, and, finally it must have a measured flight time within

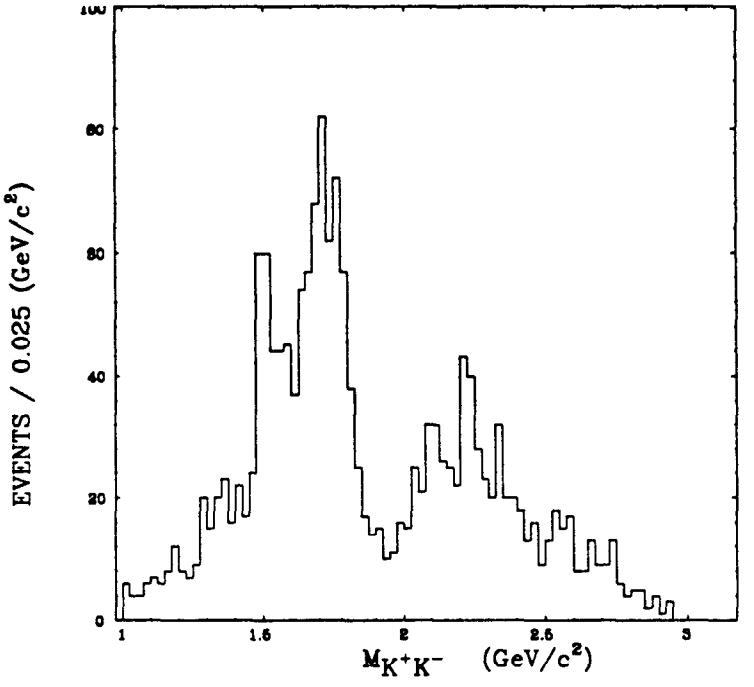

Figure 25. The K^+K^-mass distribution for the $J/\psi \rightarrow \gamma\ K^+K^-$sample after the final cuts.

3 σ of the prediction for a kaon. Since the TOF counters cover only the barrel section of the detector, which is 80% of the 4π solid angle, the event sample is reduced to 73% of its original size by these requirements. The distribution of the K^+K^-invariant mass after all selection criteria have been applied is shown in Fig.25.

The Dalitz plot for this sample is shown in Fig.26, and the distribution of K^+K^-mass versus $\cos\theta^*_{K^+}$ is shown in Fig.27, where $\theta^*_{K^+}$ is the polar angle of the K^+ in the rest frame of the K^+K^- system. The resonant structures in the mass regions of the $f_2'(1525)$ and the $\theta(1720)$ are clearly visible in both figures. As for the $J/\psi \rightarrow \gamma\ K_sK_s$data discussed in the last section, the distribution in the $f_2'(1525)$ band is enhanced for $\cos\theta^*_{K^+} = \pm 1$, while that in the $\theta(1720)$ band

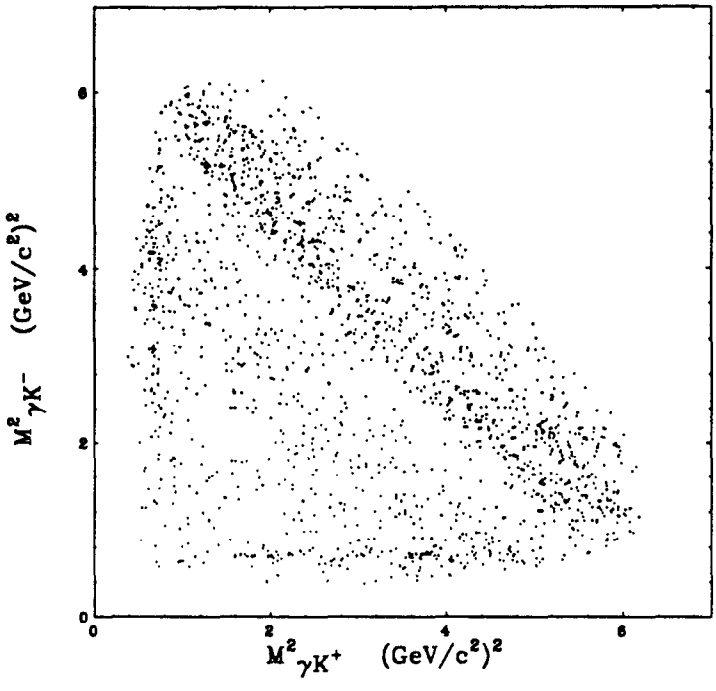

Figure 26. The Dalitz plot for the $\gamma\ K^+K^-$sample.

is of a more uniform character. As pointed out in the last section, a uniform event distribution in $\cos\theta^*_{K^+}$ is one of the characteristics of a spin 0 resonance.

The residual $J/\psi \rightarrow \pi^0 K^+K^-$ feedthrough to this final sample is evident as the curved bands in the mass region $M_{K^+K^-} \geq 1.9\ GeV/c^2$ in Fig. 27. These are $J/\psi \rightarrow \pi^0 K^+K^-$ events for which one photon from the π^0 decay is not detected by the shower counters. This feedthrough process is studied using Monte Carlo events generated using the matrix element describing the decays $J/\psi \rightarrow K^*\overline{K} \rightarrow \pi^0 K^+K^-$; detector effects and the event selection procedure for $J/\psi \rightarrow \gamma\ K^+K^-$are fully incorporated. The resulting $M_{K^+K^-}$ versus $\cos\theta^*_{K^+}$ plot for these simulated events is shown in Fig. 28; the curved bands of Fig.

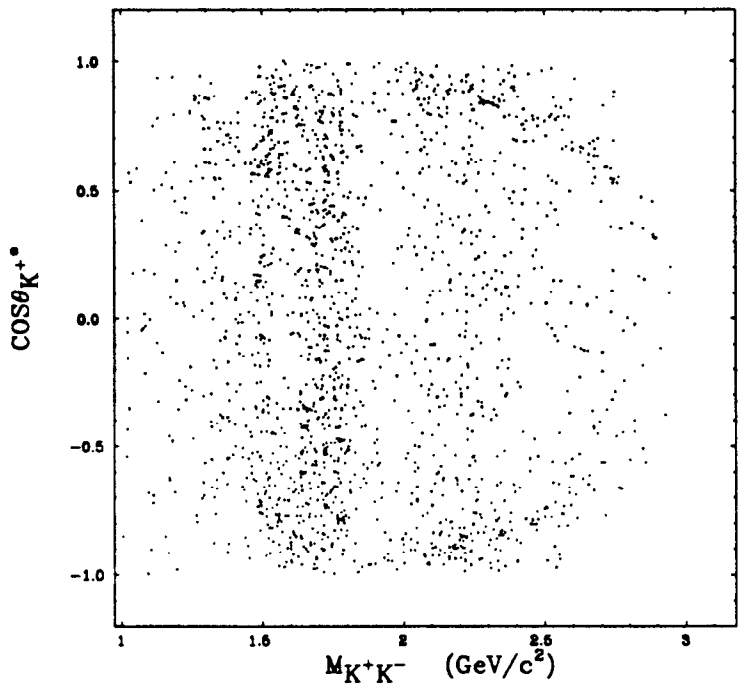

Figure 27. The scatterplot of K^+K^-mass versus $\cos\theta^*_{K^+}$ for the γ K^+K^-sample.

27 are well reproduced, and it is clear that this source of background has a negligible effect on the analysis below 2 GeV/c^2.

The mass resolution for $J/\psi \rightarrow \gamma\ K^+K^-$ events with K^+K^-mass less than 2 GeV/c^2 is shown in Fig.29 a), and the corresponding mean detection efficiency shown in Fig.29 b). These estimations are made by means of Monte Carlo studies in which the events are generated uniformly in K^+K^-mass and the event angles. As a function of the K^+K^- mass, the mass resolution varies from $4MeV/c^2$ at threshold to 8 MeV/c^2 at $M_{K^+K^-} = 2GeV/c^2$. The mean efficiency is 22%. Its dependence on the event angles will be discussed in chapter IV.

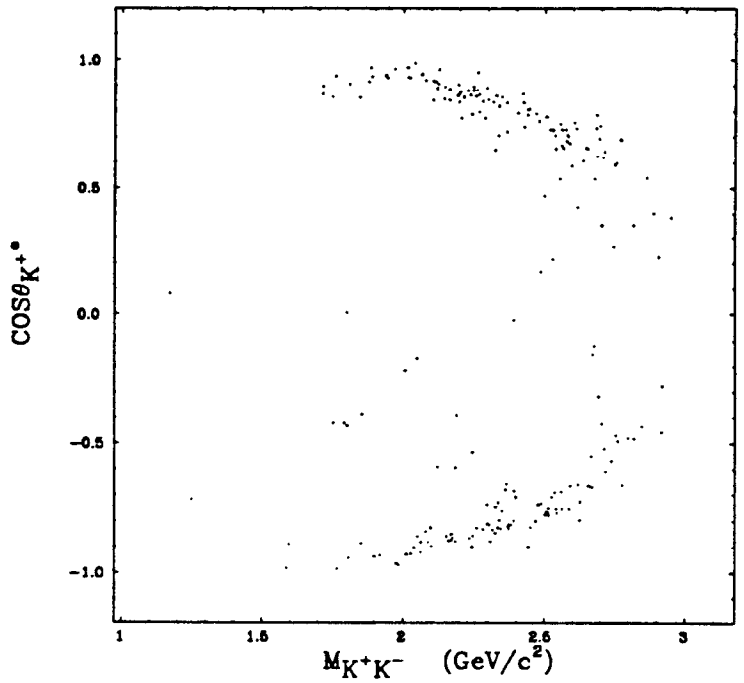

Figure 28. The distribution of K^+K^-mass versus $\cos\theta^*_{K^+}$ for the simulated $J/\psi \to K^*\overline{K} \to \pi^0 K^+K^-$ events feeding through to the γ K^+K^-sample. The normalization is arbitrary.

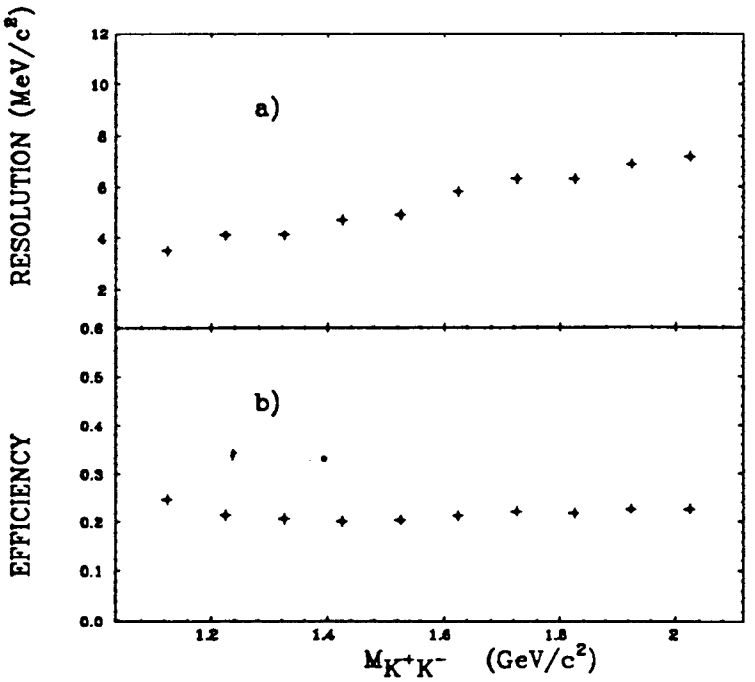

Figure 29. a) The K^+K^-mass resolution, and b) the mean $J/\psi \to \gamma$ K^+K^-detection efficiency as a function of K^+K^-mass.

CHAPTER IV

THE ANALYSIS METHOD

As stated in Chapter 1, it is the aim of this analysis to study the resonant structures in the $K\overline{K}$ systems resulting from J/ψ radiative decays by following a procedure which allows for the simultaneous inclusion of spin zero and spin two amplitudes describing the $K\overline{K}$ systems. The position, momentum and energy information for each track in each event are measured, and, for the resulting data sample, the efficiency-corrected spherical harmonic moments of the event angular distribution in each $K\overline{K}$ mass interval are obtained. The amplitudes associated with different spin and helicity states of the particles involved in the reaction are then extracted from these moments. Breit-Wigner line shape fits to the amplitudes associated with a particular state of the $K\overline{K}$ system then yield the mass, width and branching fraction estimates for the state in question.

The first section in this chapter describes the relationship between the event distribution and the underlying amplitude structure, and, subsequently, that between the spherical harmonic moments and these amplitudes. Using these relations, the amplitudes, in principle, may be determined from the experimentally measurable quantities. The second section discusses the effect of the non-uniform efficiency for event detection; the observed events are used to obtain measured values of the moments, and the procedure used to correct these values for efficiency losses is then described, as is that for extraction of the amplitudes

from the resulting efficiency-corrected moments. A detailed derivation of the relevant formulae is given in the Appendix for the interested reader. In section 3, various sources of uncertainty are discussed; in particular, the multiple solution ambiguity associated with the non-linear nature of the relations between the moments and amplitudes, and distortions due to statistical fluctuations, are considered; the details of the technical procedures adopted in order to estimate the extent of these uncertainties are presented. In sections 4 and 5, the analysis procedures are tested with Monte Carlo samples which simulate the effects of event detection with the real apparatus on the physics processes with particular selected input helicities for the intermediate $K\overline{K}$ states.

Amplitude Formalism and Moment Definition

For the decay $J/\psi \rightarrow \gamma X, X \rightarrow p\bar{p}$, where p denotes a pseudoscalar particle, the fully differential event distribution is (cf. eq. (13) in the Appendix)

$$4\pi \frac{dN}{dm\ d\Omega_X\ d\Omega_p^*} = \frac{3}{4} \sum_{\lambda_\psi, \lambda_\gamma} \left| \sum_{J_X, \lambda_X} a^{\lambda_\gamma}_{J_X, \lambda_X} \sqrt{\frac{2J_X + 1}{4\pi}} \mathbf{D}^{1*}_{\lambda_\psi, \lambda_X - \lambda_\gamma}(\Omega_X) \mathbf{D}^{J_X *}_{\lambda_X, 0}(\Omega_p^*) \right|^2 , \tag{1}$$

where m is the mass of the intermediate state X; $d\Omega = d\cos\theta d\phi$, where θ_X and ϕ_X denote the polar and azimuthal angles of X in the J/ψ rest frame, and θ_p^* and ϕ_p^* are the corresponding angles of p in the X rest frame; the definitions of the coordinate systems used are specified in detail in the Appendix; $\mathbf{D}$ is a rotational matrix whose argument, Ω, is specified in the standard way, viz. $(\phi, \theta, 0)$, where the choice of the right-most argument to be zero defines the phase convention; $\mathbf{D}^*$ denotes the complex conjugate of $\mathbf{D}$; J_X is the angular momentum of the system

X, λ_ψ, λ_γ, λ_X are the helicities of the J/ψ, γ and system X, respectively; λ_γ takes the values ± 1, as does λ_ψ, and the definition of $\mathbf{D}^1$ implies that $|\lambda_X - \lambda_\gamma| \leq 1$; $a^{\lambda_\gamma}_{J_X,\lambda_X}$ is the mass dependent complex amplitude describing decay of the J/ψ to a system X, of spin J_X and helicity λ_X, and a photon, of helicity λ_γ, followed by decay of X to $p\bar{p}$ (see eq. (14) in the Appendix). Parity conservation in these decay processes implies $a^{-\lambda_\gamma}_{J_X,-\lambda_X} = a^{\lambda_\gamma}_{J_X,\lambda_X}$ (see eq. (4),(14),(15) in the Appendix). The main objective of the present analysis is to determine the mass dependence of the $a^{\lambda_\gamma}_{J_X,\lambda_X}$ for the allowed J_X and λ_X possibilities from the event angular distribution, and thereby reveal the existence of any resonant structures.

The present analysis is restricted to events having the invariant mass of the pseudoscalar pair less than 2 GeV/c^2, consequently, only spin 0 and 2 are assumed possible for the intermediate state X (see Chapter 1). It follows that the amplitudes considered are $a_{0,0}$, for interaction through intermediate states with spin $J_X = 0$, and $a_{2,0}, a_{2,1}, a_{2,2}$, for interaction through intermediate states with spin $J_X = 2$, helicity $\lambda_X = 0, \pm 1, \pm 2$. The joint decay angular distribution, eq. (1), varies greatly according to the magnitudes and relative phases of the individual amplitudes. Indeed, even the projections onto the individual angular variables vary greatly with the amplitude structure. For example, very different projected angular distributions are obtained from eq. (1) for particular amplitude combinations, as illustrated in Fig. 30.

In general, the joint angular distribution of the sequential two-body decays can be expanded in terms of the products of the spherical harmonics of the production and decay angles of the intermediate states. The orthogonality of the spherical harmonic functions implies that the coefficient of each product of

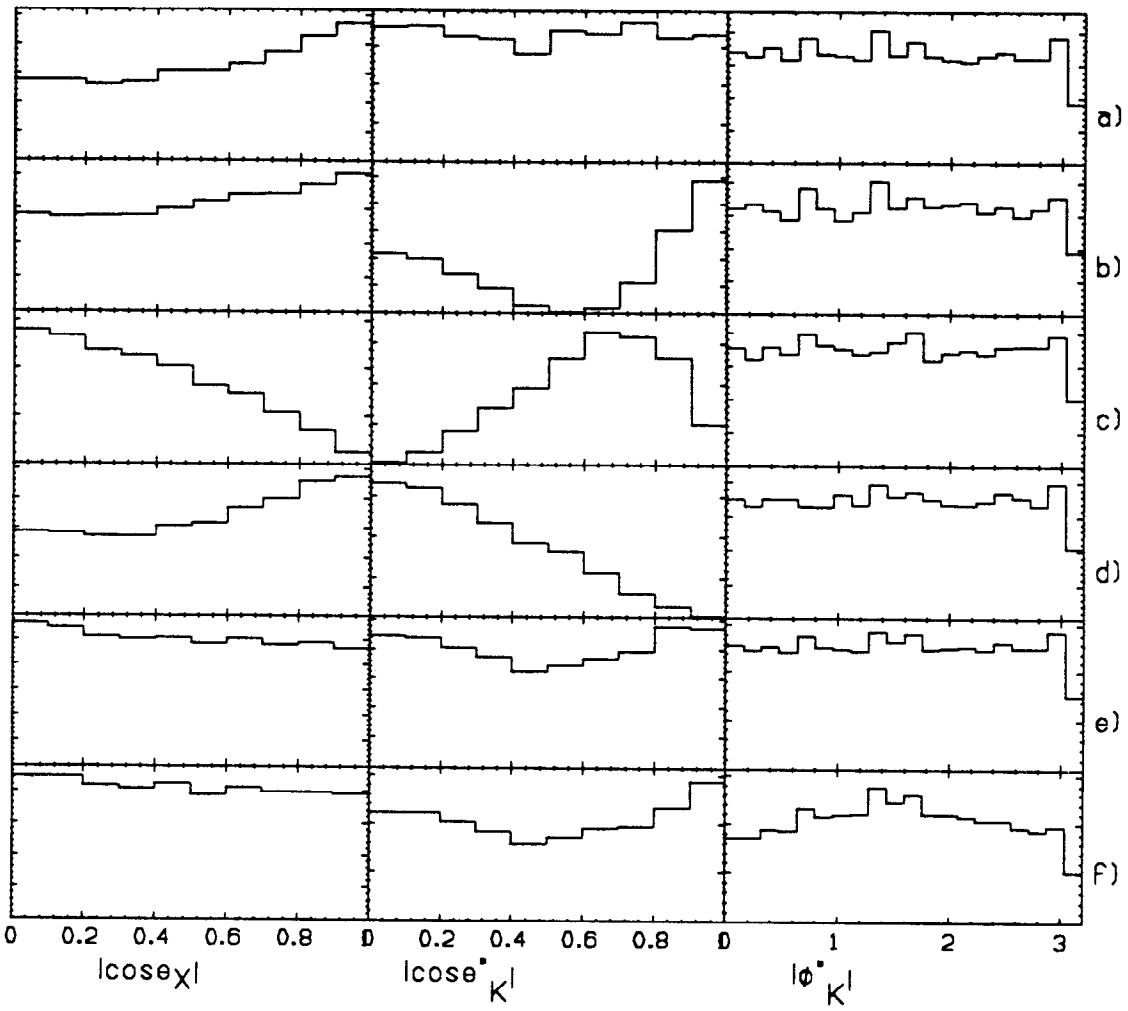

Figure 30. The projected angular distributions of events associated with some particular amplitude combinations. a) $a_{0,0}$; b) $a_{2,0}$; c) $a_{2,1}$; d) $a_{2,2}$; e) the sum of the data in b), c), d); f) $a_{2,0} = a_{2,1} = a_{2,2}$. The vertical axes are in arbitrary units.

spherical harmonics can be obtained from the data by integrating the complex conjugate of the spherical harmonic product over the event angular distribution; it is for this reason that these coefficients are called moments.

Carrying out the summations in eq. (1), expression (1) can be re-written as a linear superposition of the products of the spherical harmonics as follows† (cf. eq. (20) in the Appendix):

$$4\pi \frac{dN}{dm\ d\Omega_X\ d\Omega_p^*} = \sum_{\mathrm{j,l,(m\geq 0)}} (2-\delta_{\mathrm{m0}})\, \mathbf{T}^{\mathrm{j}}_{\mathrm{l,m}} Re\left(\mathbf{Y}_{\mathrm{j,m}}(\theta_X)\mathbf{Y}^*_{\mathrm{l,m}}(\Omega_p^*)\right). \qquad (2)$$

The limited quantum numbers allowed for system restrict the number of possible non-zero moments. The four complex amplitudes, $a_{0,0}$, $a_{2,0}$, $a_{2,1}$, $a_{2,2}$, correspond to ten real moments, as shown explicitly in eq. (19) in the Appendix.

In principle, eq. (2) above and eq. (19) in the Appendix permit the extraction of the amplitudes from the experimentally measurable quantities. Consequently, in this analysis, the data are binned according to the mass of the intermediate state, X, and the moments of the event angular distribution are measured in each such mass bin. The amplitudes are then extracted from the moments on a mass bin by mass bin basis, using eq. (19) in the Appendix. The advantages of using the intermediate results, the moments, over directly fitting amplitudes to the event angular distribution using eq. (1) , will be discussed later.

† As discussed in the Appendix, use of the argument θ_X as opposed to Ω_X means that the function is to be evaluated at $\phi_X = 0$.

Formalism of the Moment and Amplitude Measurements

For an event sub-sample observed with a real apparatus, which usually has a non-uniform detection efficiency, the measured moments (cf. eq. (22) in the Appendix) are given by

$$\mathbf{N}_\mu \equiv \mathbf{N}^{j'}_{l',m'} = 4\pi \sum_{i=1}^{N_{observed}} Re(\mathbf{Y}^*_{j',m'}(\theta^i_X)\mathbf{Y}_{l',m'}(\Omega^{*i}_p)), \tag{3}$$

where the summation is carried out over the $N_{observed}$ events in the sub-sample. The notation is such that $\mu = 1,2...10$ denotes the indices (j',l',m') of the 10 moments listed in eq. (19) in the Appendix. As explained after eq. (22) in the Appendix,$\mathbf{N}^{j'}_{l',m'}$ represents the measured value of the moment $\mathbf{T}^{j'}_{l',m'}$; it is subject to efficiency loss effects, and as a result may differ markedly from the underlying true value (cf. Fig. 32 below).

The relationship between the measured and true moments (cf. eq. (24) in the Appendix) is

$$\mathbf{N}_\mu = \sum_{\nu=1}^{10} \mathbf{C}_{\mu,\nu}\mathbf{T}_\nu, \tag{4}$$

The matrix, $\mathbf{C}$, is estimated by means of Monte Carlo studies as

$$\mathbf{C}_{\mu,\nu} = \frac{16\pi^2}{N_{generated}} \sum_{i=1}^{N_{accepted}} Re\left(\mathbf{Y}^*(\theta^i_X)\mathbf{Y}(\Omega^{*i}_p)\right)_\mu (2-\delta_{m0})\, Re\left(\mathbf{Y}(\theta^i_X)\mathbf{Y}^*(\Omega^{*i}_p)\right)_\nu \tag{5}$$

where the summation is over the set of accepted Monte Carlo events (cf. eq. (26) in the Appendix). For the mass interval in question, the Monte Carlo events are generated uniformly in mass and event angles; $N_{generated}$ is the number of generated events and $N_{accepted}$ is the number of accepted events. The

factor $\frac{16\pi^2}{N_{generated}}$ gives a normalization such that $\mathbf{T}^0_{0,0}$ is the estimate of the true number of events after efficiency correction. The Monte Carlo samples for the computation of the matrix $\mathbf{C}$ are defined such that $N_{accepted}$ is at least ten times larger than the number of real events observed in the particular mass bin; it follows that the statistical uncertainty in the $\mathbf{C}_{\mu,\nu}$ is negligible in comparison to the statistical uncertainties of the real data.

The $\mathbf{C}^{-1}N$ are called the efficiency-corrected moments, and are, consequently, denoted by $\mathbf{T}^j_{l,m}$ in the figures in this thesis.

The correlation matrix corresponding to the measured moments is estimated according to (cf. eq. (27) in the Appendix)

$$\mathbf{O}_{\mu,\nu} = 16\pi^2 \sum_{i=1}^{N_{observed}} Re\left(\mathbf{Y}^*(\theta^i_X)\mathbf{Y}(\Omega^{*i}_p)\right)_\mu Re\left(\mathbf{Y}^*(\theta^i_X)\mathbf{Y}(\Omega^{*i}_p)\right)_\nu . \qquad (6)$$

The underlying amplitudes are then obtained by minimizing

$$\chi^2 = \sum_{\mu,\nu=1}^{10} \left(\sum_{\sigma=1}^{10} \mathbf{C}^{-1}_{\mu\sigma}\mathbf{N}_\sigma - \mathbf{T}_\mu(a)\right) \mathbf{V}^{-1} \left(\sum_{\sigma=1}^{10} \mathbf{C}^{-1}_{\nu\sigma}\mathbf{N}_\sigma - \mathbf{T}_\nu(a)\right) \qquad (7)$$

where $\mathbf{T}_\mu(a)$, $\mathbf{T}_\nu(a)$ are the expressions for the moments in terms of the helicity amplitudes as listed in eq. (19) in the Appendix; $\mathbf{V} = \mathbf{COC}^+$, with $\mathbf{O}$ given by eq. (6) and $\mathbf{C}$ by eq. (5).

One of the advantages of using the moments is that the measured, efficiency-corrected moments provide a means of combining data from different decay modes or different experiments. Indeed, this analysis will combine the moments of the $J/\psi \to \gamma K^0\overline{K}^0$ and $J/\psi \to \gamma\, K^+K^-$ data samples, in order to increase

the available statistics for detailed amplitude analysis. Another advantage of using the moments is that the moments provide an intermediate step in the analysis process which permits greater insight into the underlying amplitude structure prior to the final, somewhat complicated, fit. This point will be addressed further in the next chapter when the amplitude results from the fit are discussed.

For each $K\overline{K}$ invariant mass interval, the moments and underlying amplitudes are obtained for each decay mode as well as for the combined data. Breit-Wigner line shapes are then fit to the mass dependence of the amplitude intensities corresponding to the intermediate states, X, for the combined data, in order to measure the mass and width of each such state. The branching fractions of J/ψ decay to an intermediate resonance with a given spin is then determined by the number of events associated with the resonance and the total number of J/ψ events analyzed.

Multiple Fits and Bin Size

The accuracy of the analysis method is expected to be affected by various factors, the most significant of which are listed below. Consideration of these factors led to the development of some of the technical measures adopted in the analysis procedure.

1. The multi-solution problem. In general, the amplitude analysis procedure yields multiple solutions due to the fact that the relationships between the moments of the event angular distribution and the interaction amplitudes are

not linear (cf. eq. (19) of the Appendix). This can be demonstrated by means of the following simple example.

Let the amplitude $a_{2,2}$ be non-zero, with the value A, and let all other amplitudes be equal to zero; the measured moments will then be as follows:

$$T^0_{0,0} = |A|^2,$$
$$T^2_{0,0} = \frac{\sqrt{5}}{10}|A|^2,$$
$$T^0_{2,0} = \frac{-2\sqrt{5}}{7}|A|^2,$$
$$T^2_{2,0} = \frac{-1}{7}|A|^2,$$
$$T^2_{2,1} = 0,$$
$$T^2_{2,2} = 0,$$
$$T^0_{4,0} = \frac{1}{7}|A|^2,$$
$$T^2_{4,0} = \frac{\sqrt{5}}{70}|A|^2,$$
$$T^2_{4,1} = 0,$$
$$T^2_{4,2} = 0.$$

These moments are reproduced exactly by the following different amplitude combination:

$$|a_{0,0}|^2 = \frac{5}{6}|A|^2,$$
$$|a_{2,0}|^2 = \frac{1}{6}|A|^2,$$
$$\phi_{2,0} - \phi_{0,0} = 180^0,$$
$$|a_{2,1}|^2 = 0,$$
$$|a_{2,2}|^2 = 0.$$

where the $\phi_{2,0}, \phi_{0,0}$ are the phase angles of the amplitudes $a_{2,0}, a_{0,0}$.

It should be emphasized, however, that an ambiguity problem of this kind does not always occur with real data; rather, its existence or non-existence depends on the amplitude structure in the particular mass interval under study. For example, in the above illustration, the ambiguity disappears when a significantly non-zero $a_{2,1}$ amplitude is present. In general it seems to be the case that the greater the number of amplitudes contributing to the moment structure, the less likely it is that an ambiguity will occur.

2. Statistical errors. Besides the ambiguity above, however, there is another kind of multi-solution problem. This is associated with distortions of the χ^2 function, defined earlier, as a result of large statistical fluctuations. If the distortions are large, they can result in fake local minima of the χ^2 function, and thereby lead to additional wrong solutions for the amplitude values.

3. The efficiency correction. Since the efficiency of detection is estimated with Monte Carlo events, an inaccurate simulation of the detector response to the event tracks affects the precision with which the true distribution of the real data can be estimated.

4. Background events. Event feedthrough from other decay modes contributes to the measured moments for the selected data sample. This contribution is expected to be small and smoothly distributed if only a few background events are present in the sample. However, it may become significant if the number of background events in the sample is large, and in this case, the moments of the background events have to be estimated and taken into account.

Among the factors listed above, the contribution of the latter two is not the main concern of this section, since great effort has been made to ensure accurate

detector simulation, and the event samples selected are with high purity, as discussed in the last Chapter.

To solve the multi-solution ambiguity, the first step is to find all possible solutions in a given mass interval. In order to do this, twelve independent fits are carried out for each mass bin, each of which starts with a set of random parameter values. The amplitude results from all such successful fits are retained. The final amplitude values for each mass bin are chosen to be those corresponding to the fit having the lowest χ^2, while the deviations of the results of the other fits are taken into account in estimating the corresponding amplitude uncertainties. The bin width is chosen as a compromise between the desire for high statistics in each mass bin, and the need for detailed information on the mass dependence of each measured amplitude. The choice is made such that $100 \sim 200$ events are observed in each mass bin in the regions containing interesting resonant structure. Monte Carlo studies showed that, at this level of statistics, reliable amplitude results can be obtained. To achieve this, a bin width $\Delta M = 100 MeV/c^2$ is used for the individual $K\overline{K}$ modes, while a width $\Delta M = 50 MeV/c^2$ is used for the combined K^+K^- and K_sK_s data. These bin widths are still narrow enough to resolve the peaks of the $f_2'(1525)$ and $\theta(1720)$.

Tests of the Moment Measurement and Efficiency Correction Procedures

The analysis technique is tested extensively with Monte Carlo data samples generated with various input helicity configurations for the intermediate states.

The moment measurement procedure defined in eq.(3) is first tested with the angular information (Ω_X, Ω_p^*) from the generated events with no detector effects included. The measured moments are compared with the predictions of the moment-amplitude relations given in eq. (19) of the Appendix. These tests check the approximation of the integration by a summation over the number of events in the sample.They also check the moment-amplitude relations, the definitions of the various reference frames used,and the analysis code for the present study. The importance of these tests cannot be overstated, because all of these topics are essential to the analysis. For example, an error introduced during the lengthy derivation of the moment-amplitude relations can result in completely wrong answers being obtained from the analysis. In order to check every coefficient in the moment-amplitude relations, event samples were generated firstly with only one amplitude non-zero, and then, secondly, with all possible pairs of amplitudes non-zero. The tests showed that the moments measured are always consistent with the calculated values within statistical errors. The conclusion is that the moment measurement procedure, the moment-amplitude relations and the definitions of the various reference frames are all correct.

The efficiency correction procedure is essential for the study of real data samples since the detection efficiency of the apparatus is non-uniform in the variables describing the final states under consideration. In order to demonstrate that any such procedure is at least self-consistent, it should be shown that the input moments of Monte Carlo samples which are subject to efficiency losses are recoverable.

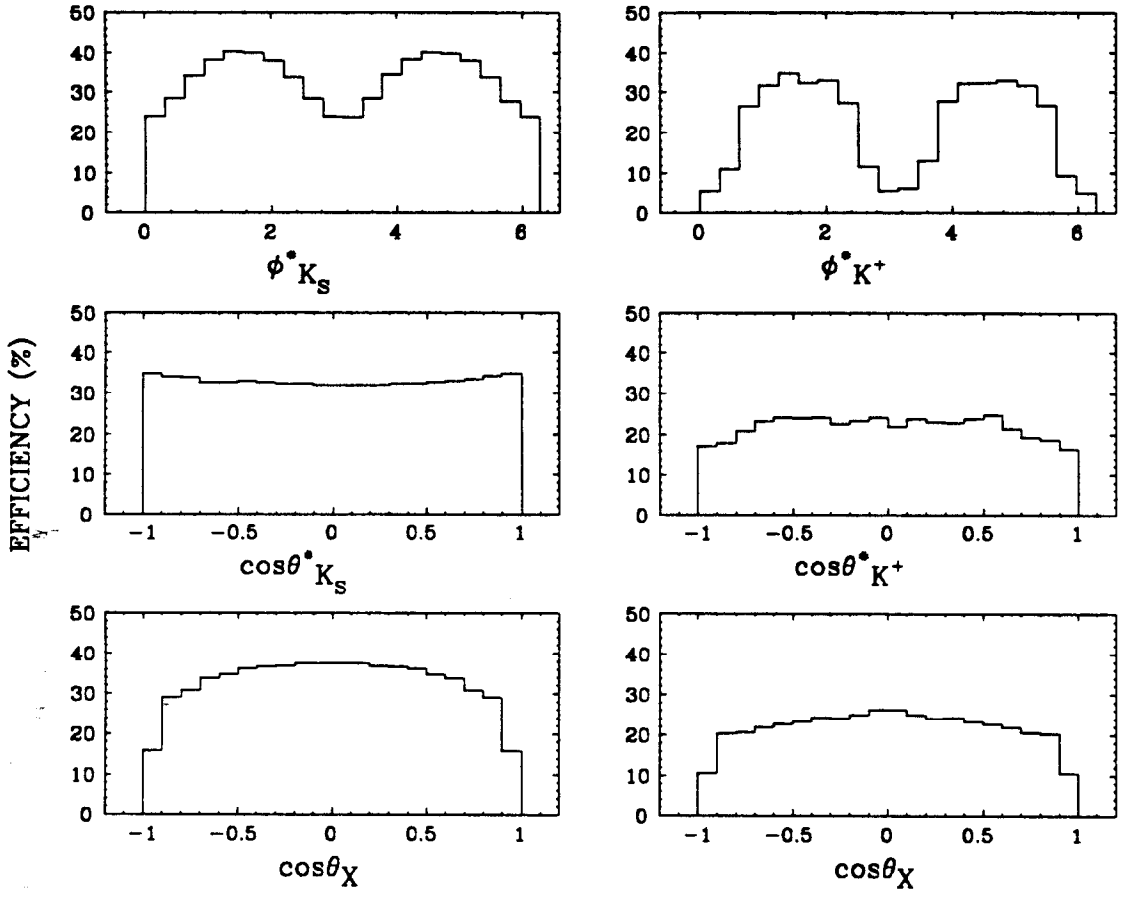

Figure 31. The projections of the efficiency functions for the event angles; left: $J/\psi \rightarrow \gamma\ K_s K_s$; right: $J/\psi \rightarrow \gamma\ K^+K^-$.

The efficiency variations of the MARK III detector for the J/ψ events under study are illustrated in Fig. 31. The plots show the projections of the efficiency functions for each of the event angles, simulated with events uniformly distributed over these angles, and generated with $m_{p\bar{p}} = 1.72\ GeV/c^2$. Events with the azimuthal angle, ϕ_p^*, of the p in $p\bar{p}$ rest frame near 0 or π are likely to have tracks parallel to the beam direction, and they will thus be missed by the

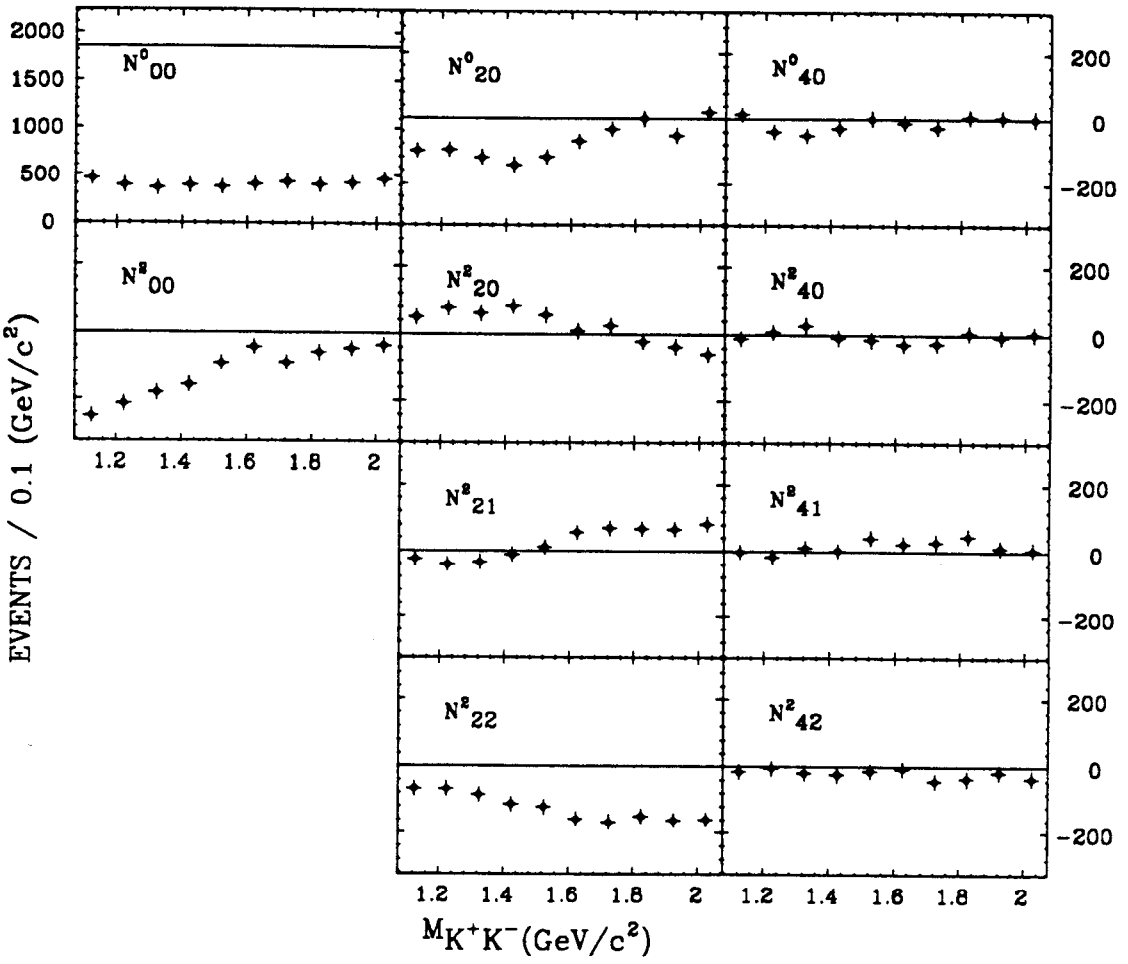

Figure 32. The effects of efficiency losses on the measured moments of the uniformly generated Monte Carlo sample of $J/\psi \to \gamma\ K^+K^-$events. Data points: the measured moments; solid lines: the generated moments.

drift chamber, which has its wires strung along this direction, or by the Time of Flight counters, which cover the barrel section of the detector only.

To display the effect of the efficiency losses, the measured moments of Monte Carlo $J/\psi \to \gamma\ K^+K^-$events, which are generated uniformly in all variables,

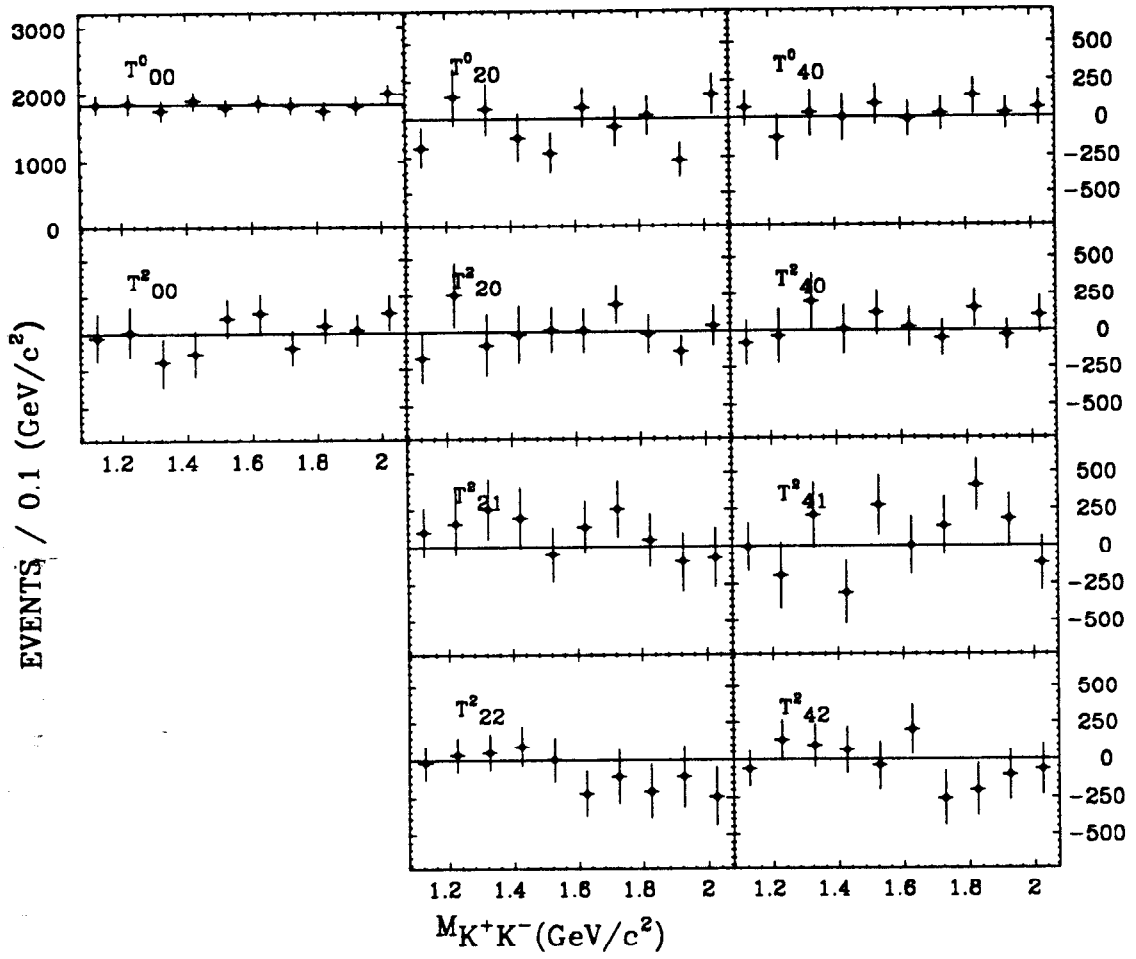

Figure 33. The efficiency-corrected moments for the uniformly generated Monte Carlo samples of $J/\psi \rightarrow \gamma\ K^+K^-$events. Data points: the measured efficiency-corrected moments; solid lines: the generated moments.

are shown in fig. 32 as the data points. The expected values of the moments are shown by the solid lines in the figure; these are zero for all moments except the first one, due to the orthogonal property of the spherical harmonics. The first spherical harmonic is normalized so that the first moment corresponds to

the total number of events. The $J/\psi \rightarrow \gamma\ K^+K^-$mode is chosen among the decay modes under study, since events of this mode suffer the greatest efficiency losses; this is because the charged tracks must not only be found and reconstructed in the drift chambers, but they must also be detected by the Time of Flight counters. In estimating the efficiency correction matrix for each mass interval, the detector response to the tracks is fully simulated, the event selection process for the real data is applied, and the events are binned according to the reconstructed mass of the intermediate state, as for the real data. For this test, about 1900 events are generated in each mass interval.

The resulting efficiency-corrected moments are shown in Fig. 33 as the data points, while the solid lines represent the values of the generated moments, as in Fig. 32. The much larger error bars in Fig. 33 compared to Fig. 32 are a consequence of the application of the efficiency-correction procedure to a sample which spans the space of the final state variables in a non-uniform way. Since the efficiency corrected moments are consistent with the expected values within errors, it is concluded that the correction procedure yields satisfactory results.

In order to demonstrate the capabilities of the efficiency-correction procedure for events having non-uniform angular distributions, Monte Carlo samples with different helicity amplitude combinations are generated, and resulting efficiency-corrected moments examined. The efficiency-corrected moments for samples with $a_{2,1} : a_{2,0} = \frac{5}{3}e^{i60^\circ}$, $a_{2,2} : a_{2,0} = \frac{5}{3}e^{i60^\circ}$ and $a_{2,2} = 1$ are shown as the data points in Figs. 34 , 35 and 36 respectively. Three independent sub-samples are generated for each amplitude combination; each contains about 200 observed events in order to simulate the statistics in the $\theta(1720)$

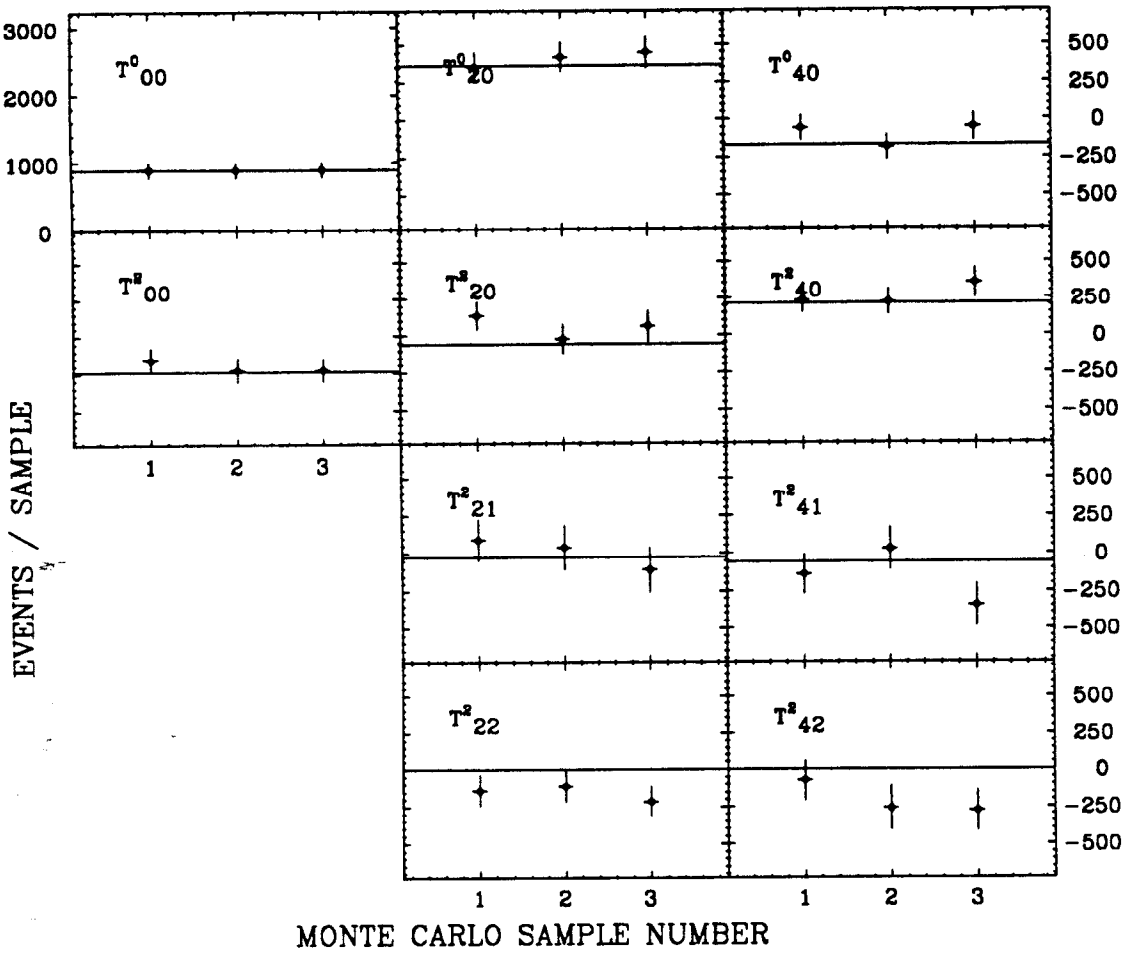

Figure 34. The efficiency-corrected moments for samples generated with $a_{2,1} : a_{2,0} = \frac{5}{3}e^{i60^\circ}$. There are about 200 observed events in each sample. Data points: the measured, efficiency-corrected moments; solid lines: the generated moments.

mass bin for the real K^+K^- data. The moments calculated on the basis of the moment-amplitude relations are plotted as the solid lines. In general, the efficiency-corrected moments are consistent with the expected values, so that it

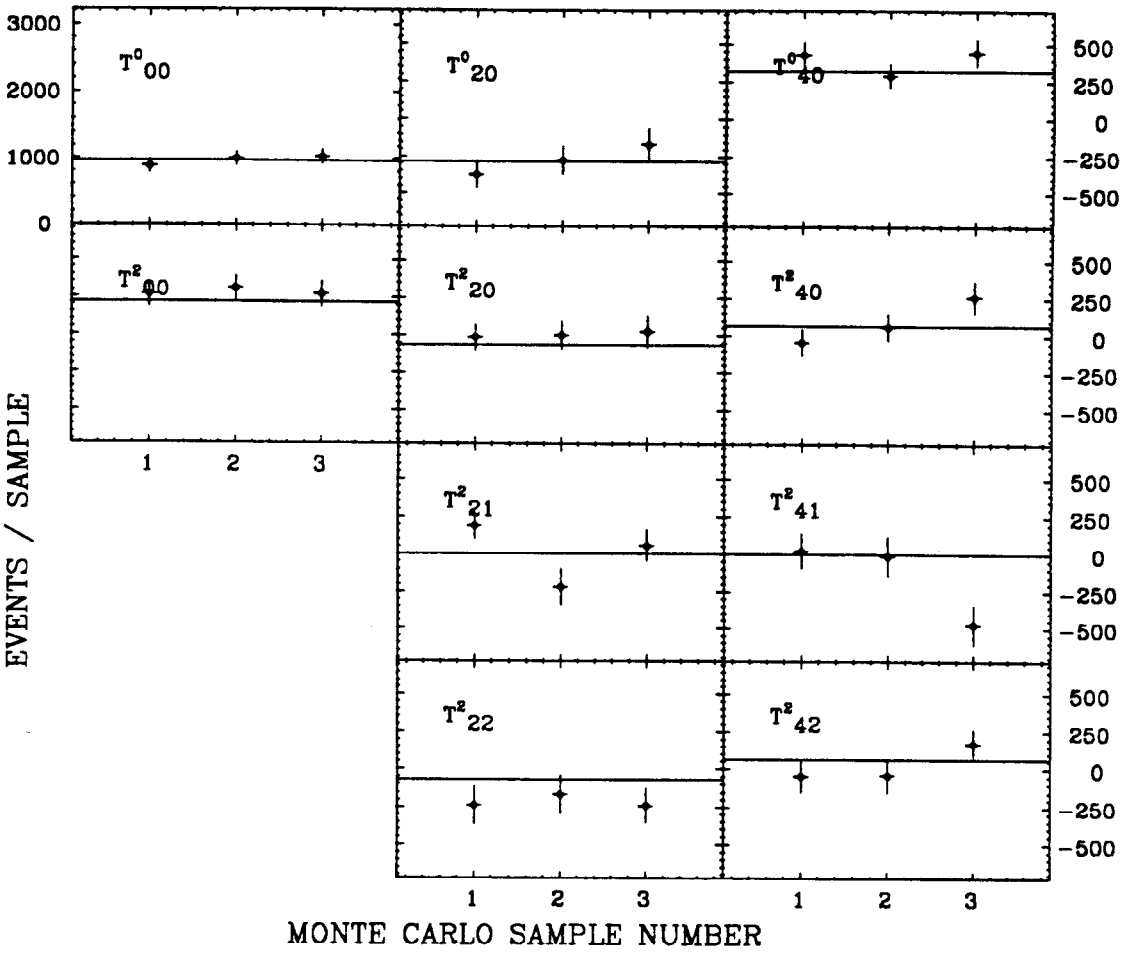

Figure 35. The efficiency-corrected moments for samples generated with $a_{2,2} : a_{2,0} = \frac{5}{3}\epsilon^{i60°}$. There are about 200 observed events in each sample. Data points: the measured, efficiency-corrected moments; solid lines: the generated moments.

can be concluded that a satisfactory correction for these sub-samples has been achieved.

The moments corresponding to pure $a_{2,2}$ (cf. Fig. 36) illustrate the ambiguity discussed previously. As a signature of this ambiguity, $T^0_{2,0}$ is negative and

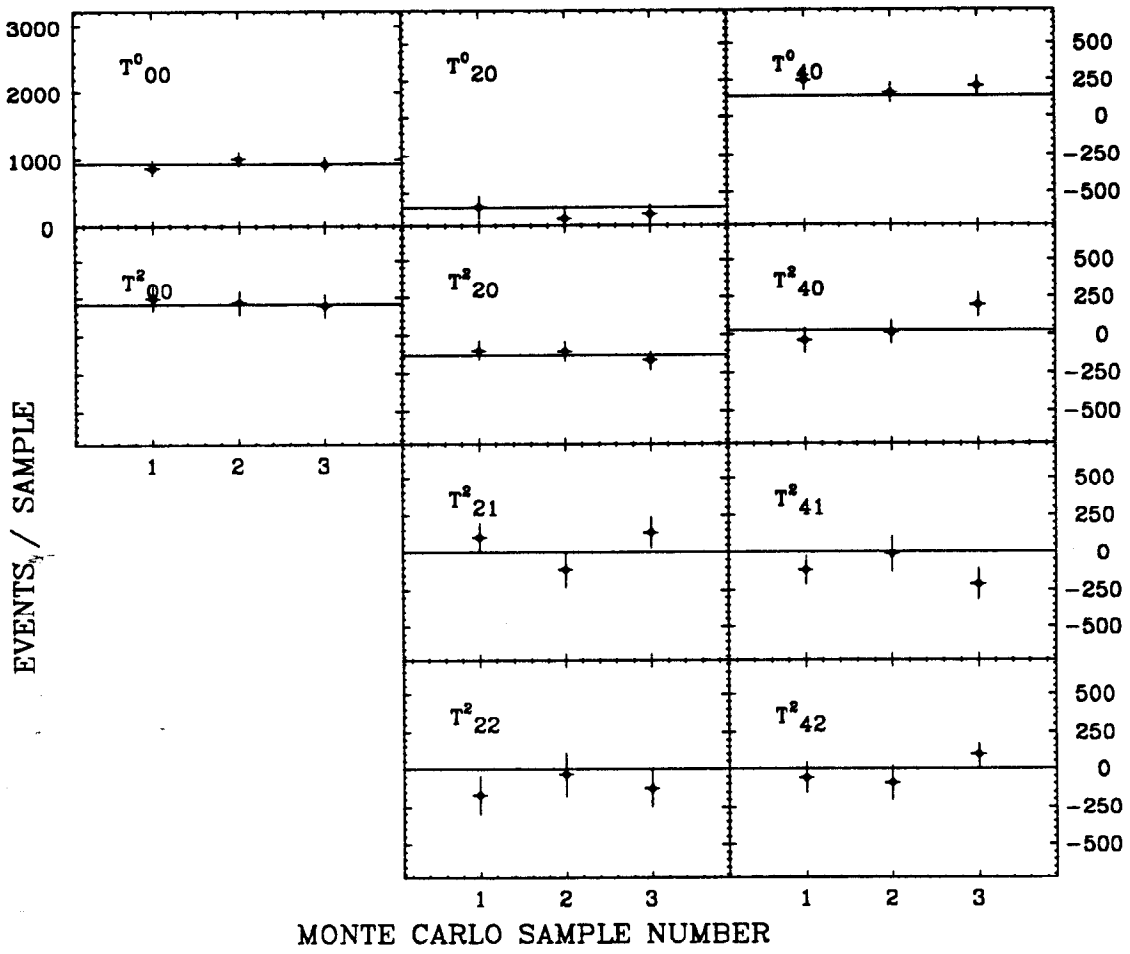

Figure 36. The efficiency-corrected moments for samples generated with $a_{2,2} = 1$. There are about 200 observed events in each sample. Data points: the measured, efficiency-corrected moments; solid lines: the generated moments.

significantly below zero. It should be noted that this feature does not appear in the moments obtained with the real data in any mass bin, as we will discuss in the next chapter, which indicates that this particular ambiguity is not directly relevant to the real data under study.

Tests of the Amplitude Extraction Procedure

As discussed previously, the amplitudes are determined by minimizing a χ^2. Multiple minimization trials based on randomly-generated starting points are carried out for each sub-sample in order to find all acceptable solutions for the mass interval in question. The ability of the analysis procedure to arrive at the correct solution is tested with Monte Carlo samples.

As for the tests of the moment measurement procedures described in the previous section, Monte Carlo samples are generated with various input helicity configurations for the intermediate states. It is found that the events associated with amplitudes $a_{0,0}, a_{2,0}, a_{2,1}$ are readily identified, while those associated with $a_{2,2}$ are subject to ambiguity. Some sub-set of the events associated with $a_{2,2}$ are usually assigned to other amplitudes, especially to $a_{0,0}$. This is due to the type of ambiguity discussed previously. The fraction of such mis-identified events varies with the ratios of the input amplitudes. The greater the strength of the other amplitudes, the smaller the fraction of misidentified $a_{2,2}$ events. The ambiguity associated with a_{22} has also been pointed out by Yan,[56] whose conclusions are consistent with those above.

To demonstrate the power of the analysis to distinguish amplitudes in cases where no a_{22} ambiguity is present, the amplitude results for Monte Carlo samples generated according to selected amplitude combinations are shown in Fig. 37. The samples are generated with single amplitudes $a_{2,0}, a_{2,1}$ or an amplitude combination $a_{2,1} : a_{2,0} = \frac{5}{3}e^{60^0}$. For these Monte Carlo samples, the reconstructed mass of the $K\overline{K}$ system is in the region of $1.675 - 1.775 GeV/c^2$. Corrections are

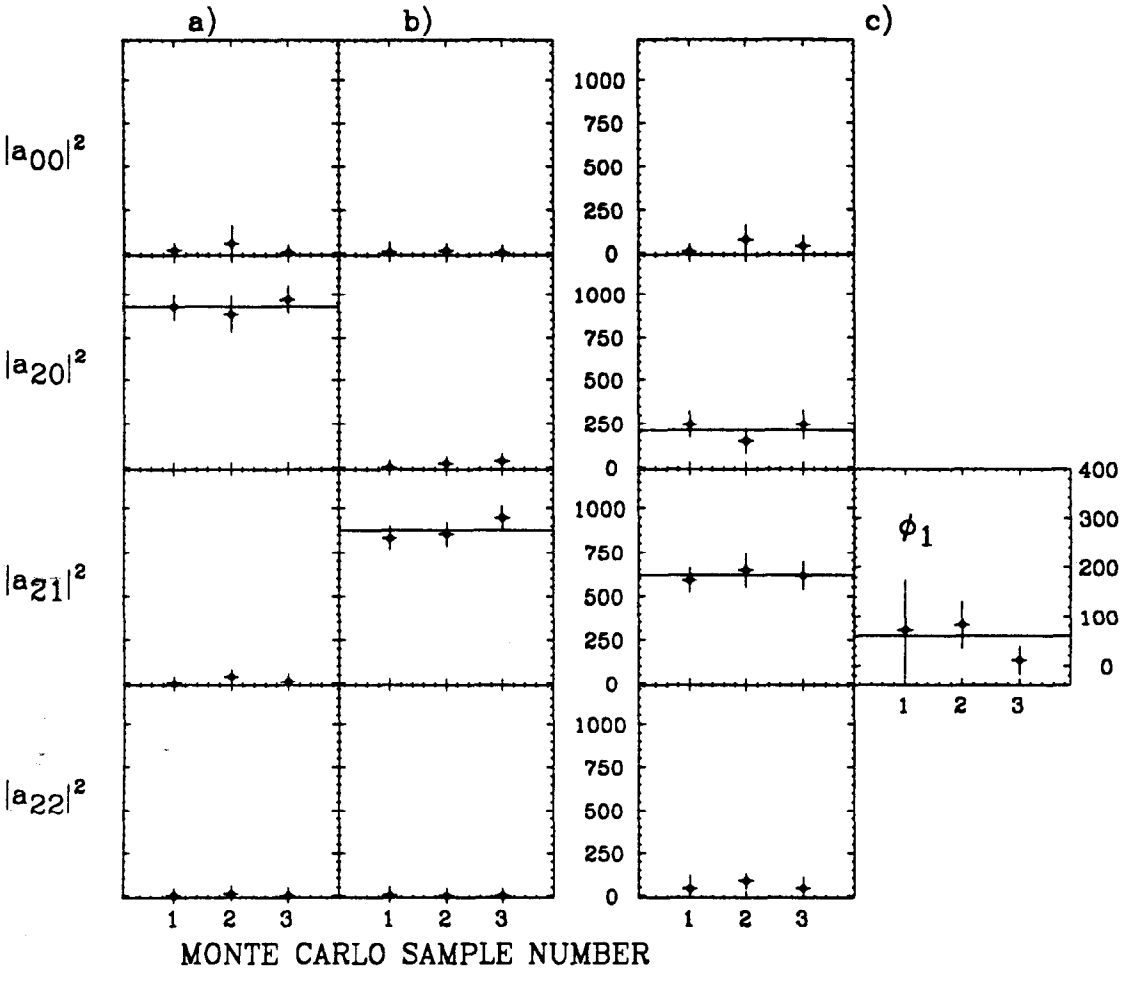

Figure 37. The amplitude results for sub-samples generated with a) pure $a_{2,0}$, b) pure $a_{2,1}$, and c) $a_{2,1} : a_{2,0} = \frac{5}{2}e^{60^0}$. The samples correspond to $J/\psi \rightarrow \gamma\, K^+K^-$ events, and are subject to efficiency loss effects. There are about 200 observed events in each sub-sample.

made for efficiency loss effects due to the apparatus. For each amplitude combination, three sub-samples are generated, each containing about 200 observed events, thus simulating the statistics of the mass bins around the $\theta(1720)$ peak in the K^+K^- data. The input amplitude values are plotted as solid lines, and

the fit results are the data points, for the fit converging to the lowest χ^2 value among the multiple fits conducted on each sub-sample. The input amplitude intensities are well reproduced. The measurements of the phase angles are less precise because of the limitation of the statistics.

The errors on the amplitude values are obtained from the MIGRAD minimization procedure in the program MINUIT.[57] This error estimation procedure is used for all amplitude values in this thesis except those for which it is explicitly stated that the more detailed MINOS procedure has been employed.

No ambiguity exists in the moment-amplitude relations if $a_{0,0}$ is not included. As a test of the analysis without $a_{0,0}$ in the model, events are generated with only spin 2 amplitudes, and a pure spin 2 fit is made to the resulting data. The results are plotted as the crosses in Fig. 38 for samples with various input values of the amplitude ratios, $x = \frac{a_{2,1}}{a_{2,0}}$, and $y = \frac{a_{2,2}}{a_{2,0}}$, denoted by the diamonds. Satisfactory fits are achieved.

At first sight, this test appears irrelevant since the analysis of real data has to include spin 0 and spin 2. However, it does demonstrate that the analysis results are reliable whenever spin 0 is small, which is the case in the $f_2'(1525)$ mass region, as reported in the following chapter. With the multi-solution problem in mind, tests of the reliability of the results from the real data are conducted in the next chapter.

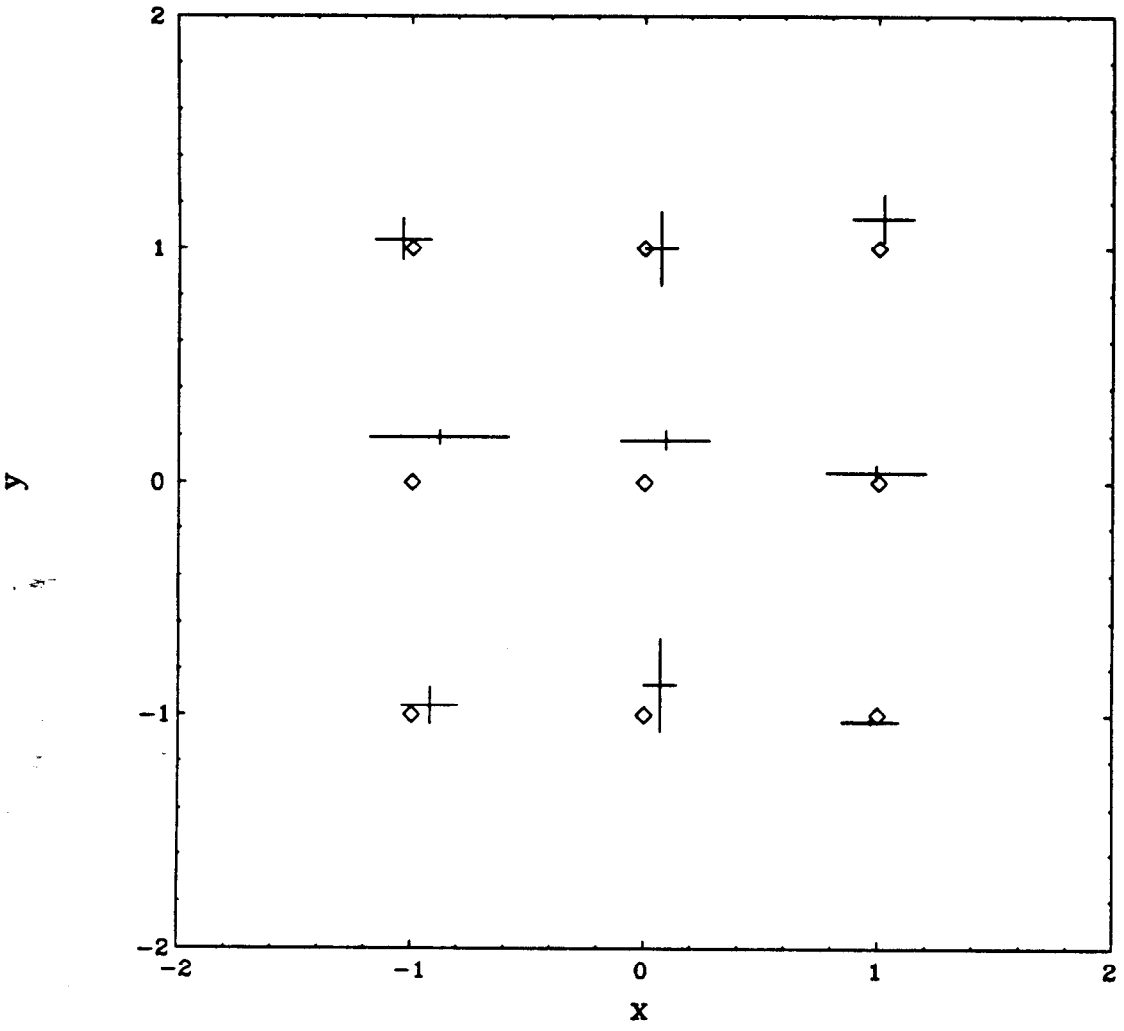

Figure 38. The amplitude results for pure spin 2 models fit to samples generated with pure spin 2 amplitudes with $x = \frac{a_{2,1}}{a_{2,0}}$, and $y = \frac{a_{2,2}}{a_{2,0}}$; diamonds: the input values; crosses: the fit results and errors. There are about 200 observed events in each sample.

CHAPTER V

MOMENT AND AMPLITUDE RESULTS

The analysis procedure applied to the $J/\psi \rightarrow \gamma\ K_sK_s$ and $J/\psi \rightarrow \gamma\ K^+K^-$ event samples, and tests thereof, have been described in the previous chapter. In this chapter, the measured moments before and after efficiency correction are presented; the amplitudes extracted from these data are then shown, and their quality and uniqueness discussed. The sensitivity of the results to the choice of the mass intervals, the event selection criteria, etc. is then considered. Further tests are applied to the fits to the $\theta(1720)$ mass region. The results of the present analysis are then compared to those from the previous MARK III analysis of the $\theta(1720)$ mass region.

Moment Measurements

The measured moments, $N^j_{l,m}$,of the $J/\psi \rightarrow \gamma K^0\overline{K}^0$ and $J/\psi \rightarrow \gamma\ K^+K^-$ data with invariant mass of the $K\overline{K}$ system in the range 1.075 to 2.075 MeV/c^2 are shown as the data points in Figs. 39 and 40 respectively. The results correspond to $100MeV/c^2$ mass intervals, with which the $f_2'(1525)$ and $\theta(1720)$ resonances peak around the central values of the 5th and 7th bins respectively. The bin width chosen ensures a reasonable number of events in the bins near these peaks. The mass resolution, as discussed in chapter 4, is less than $10MeV/c^2$, which is much less than the bin width used. The data on $J/\psi \rightarrow \gamma K^0\overline{K}^0$are obtained by applying an isospin correction factor to the data

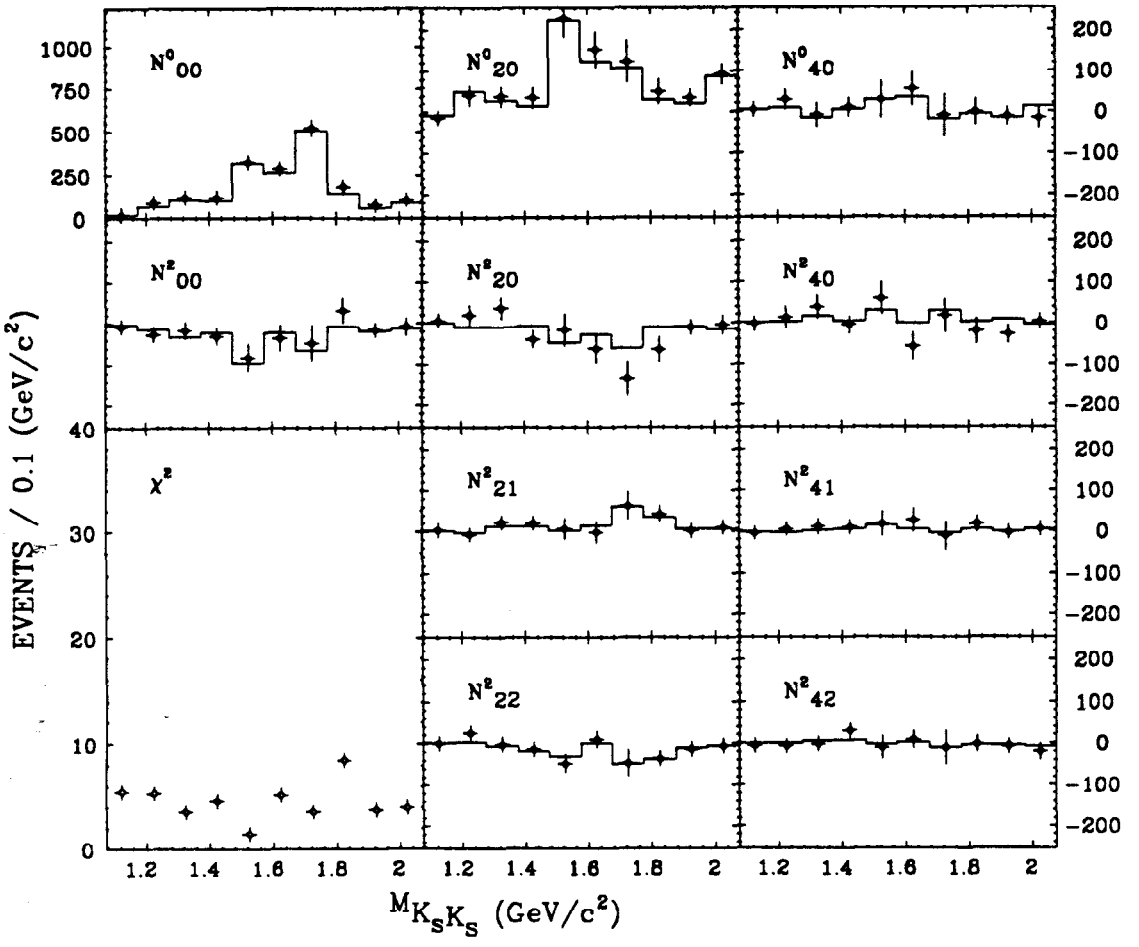

Figure 39. The measured moments of the $J/\psi \to \gamma K^0\overline{K}^0$data. The data points are the measurements; the histogram shows the values predicted from the amplitude results, taking account of efficiency effects. An isospin correction factor has been applied to the moments obtained from the $J/\psi \to \gamma\ K_sK_s$data. The plot in the bottom left corner shows the χ^2 value for the amplitude fit to the efficiency-corrected moments.

on $J/\psi \to \gamma\ K_sK_s$. The histograms in the moment plots, and the χ^2 distribu-

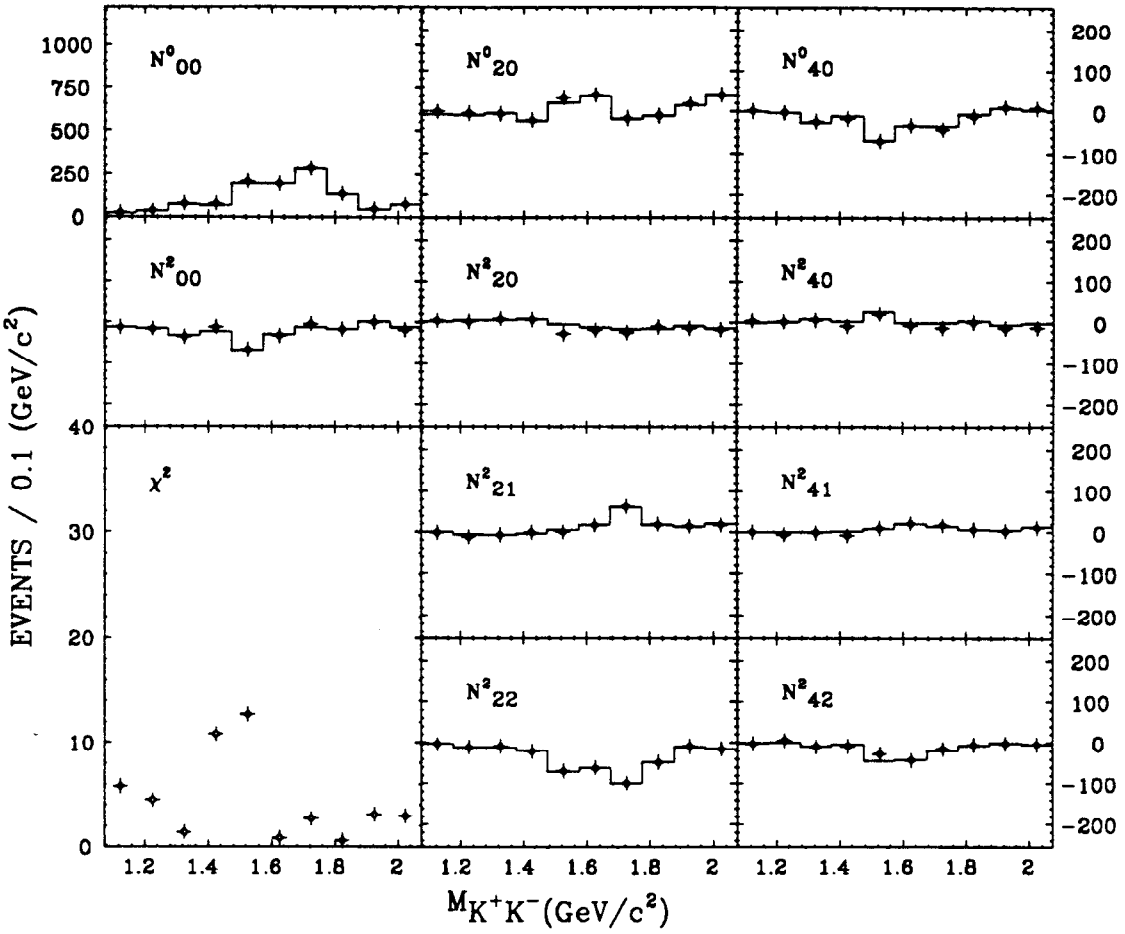

Figure 40. The measured moments of the $J/\psi \to \gamma\, K^+K^-$data. The data points are the measurements; the histogram shows the values predicted from the amplitude results, taking account of efficiency effects. The plot in the bottom left corner shows the χ^2 value for the amplitude fit to the efficiency-corrected moments.

tion plotted at the bottom left corner in Figs. 39 and 40 will be discussed in the following section.

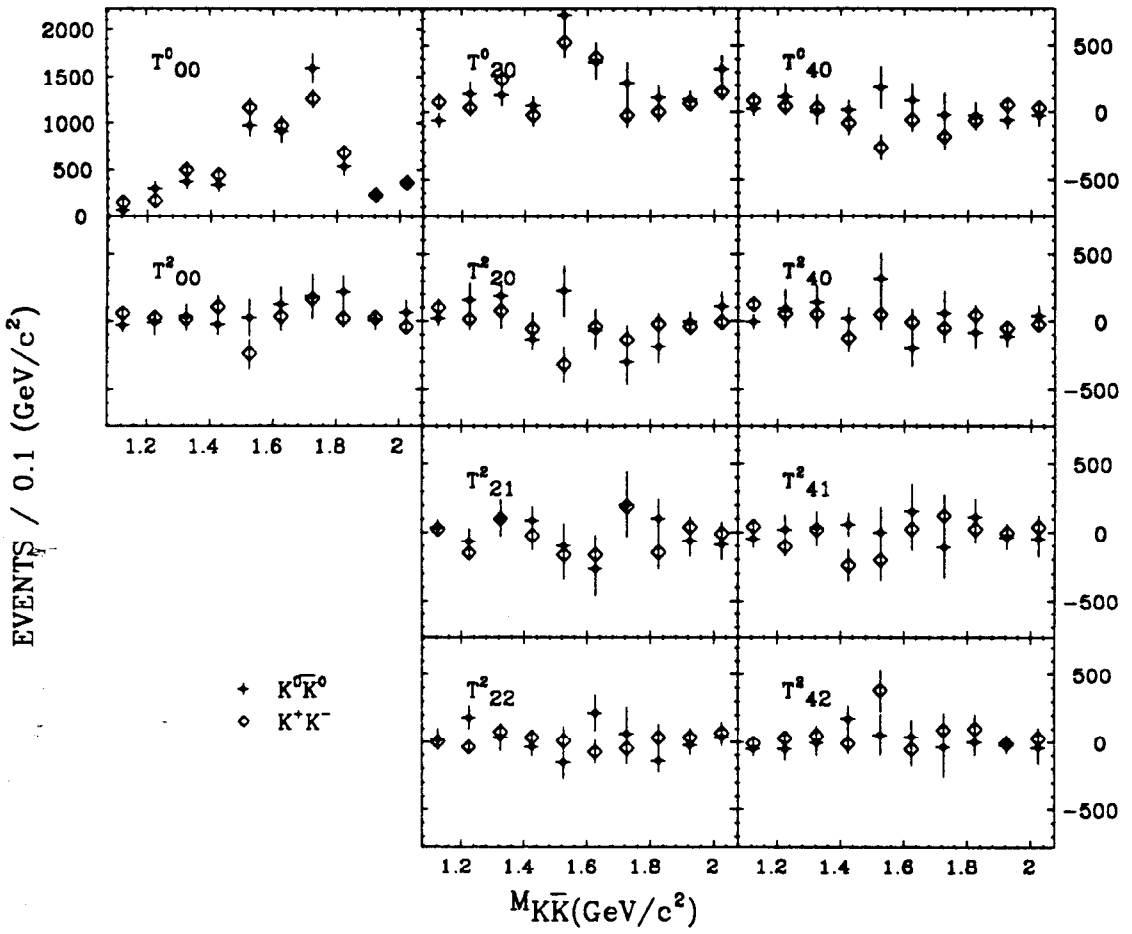

Figure 41. Moments of the $J/\psi \to \gamma K^0\overline{K}^0$ and $J/\psi \to \gamma\, K^+K^-$ data after efficiency correction. An isospin factor is applied to the $J/\psi \to \gamma\, K_sK_s$ data to obtain the moments of $J/\psi \to \gamma K^0\overline{K}^0$ decay.

As discussed in the previous chapter, the measured moments have to be corrected for efficiency losses. The moments of the two decay modes after efficiency correction, denoted by $T^j_{l,m}$, are plotted together in Fig. 41. For purely isoscalar amplitudes, the $K^0\overline{K}^0$ and K^+K^- distributions should be identical; this appears to be the case, within error. These efficiency-corrected moments are

tabulated in Table 4, and Table 5. Each bin plotted in Fig. 41 is divided into two bins of $50MeV/c^2$. The Tables will allow future experiments to compare their results to those of the present analysis; indeed such experiments may even combine their data with those of these Tables in order to increase the statistics for the amplitude fits.

As mentioned before, the spherical harmonic $Y^0_{0,0}$ is normalized such that the measured moment $N^0_{0,0}$ is equal to the number of events observed, and that the efficiency-corrected moment, $T^0_{0,0}$, corresponds to the estimated number of events after efficiency correction.

Since the statistics are low in this analysis, it is difficult to draw convincing conclusions about the possible amplitude solutions on the basis of the moments alone. However, some basic features of the amplitude results can be anticipated beforehand; for example, all of the data points for the moment $T^0_{2,0}$ are positive definite, and this differs from the Monte Carlo samples generated with pure a_{22}, i.e. the samples for which the multiple solution ambiguity was illustrated in the previous chapter. This indicates that this ambiguity will not be present at a very significant level in the data. A further useful qualitative result which can be obtained from the moments alone is presented in the next section, when the results of the fits are discussed.

Amplitude Distributions

The multiple χ^2 minimization processes is applied in each mass bin in order to obtain all possible solutions for the relevant amplitude values. During the fit procedure, the magnitudes and the phase angles of all four amplitudes are

Table 4. Efficiency corrected moments of the $J/\psi \to \gamma K^0 \overline{K}^0$ data

Bin	$T^0_{0,0}$	$T^2_{0,0}$	$T^0_{2,0}$	$T^2_{2,0}$	$T^2_{2,1}$	$T^2_{2,2}$	$T^0_{4,0}$	$T^2_{4,0}$	$T^2_{4,1}$	$T^2_{4,2}$
1	44.0± 31.2	-30.9± 24.6	-47.6± 33.8	31.9± 25.5	-12.2± 15.4	45.9± 81.3	38.8± 27.6	-28.4± 22.7	21.7± 26.5	-29.8± 57.0
2	27.7± 20.7	-5.0± 20.0	-16.2± 14.0	-2.3± 10.5	35.9± 35.9	-11.5± 41.0	-4.0± 8.5	16.2± 14.8	-47.0 ± 47.5	-24.3± 19.3
3	128.7± 41.8	-77.0± 35.4	-20.2± 39.9	5.0± 32.0	-6.7± 61.7	59.6± 55.1	10.7± 35.6	4.5± 28.3	84.0 ± 73.8	-86.4± 56.2
4	166.1± 53.6	57.7± 77.1	152.2± 78.2	145.5±113.8	-62.0± 67.2	120.2± 65.5	103.2± 84.4	87.1± 129.3	-70.1 ± 78.8	32.6± 68.7
5	225.6± 58.5	25.0± 66.7	69.6± 66.3	138.1± 86.8	49.8± 84.3	98.5± 78.5	-23.1± 76.0	101.7± 99.7	31.7 ± 75.5	-35.3± 81.4
6	148.2± 44.7	18.1± 55.5	62.5± 53.9	50.8± 78.8	52.1± 63.0	-61.8± 63.6	23.4± 44.0	42.2± 61.8	6.0 ± 84.2	30.0± 48.2
7	116.4± 40.7	19.4± 33.9	22.3± 36.1	-19.5± 29.4	-9.4± 81.0	-20.8± 36.6	-32.0± 39.4	14.9± 27.3	73.0 ± 55.7	60.9± 57.0
8	227.0± 54.9	-42.4± 69.6	27.1± 61.3	-118.8± 76.8	95.9± 62.8	-16.5± 56.0	48.4± 54.2	2.0± 73.6	-9.0 ± 62.9	117.5± 76.2
9	396.7± 76.4	44.9± 82.2	290.9±110.0	129.1±119.9	30.3± 104.2	-42.6± 78.3	218.0± 108.9	309.5± 108.5	-22.5 ± 134.1	-21.1± 104.2
10	572.6± 89.1	-21.8±106.6	432.3±111.1	93.3±144.6	-108.0± 124.6	-116.9± 93.3	-20.6± 118.1	20.2± 149.2	38.1 ± 126.6	68.4± 108.1
11	345.1± 72.6	112.7± 77.0	263.7± 91.2	-35.6± 94.1	-119.0± 113.9	63.1± 52.7	127.4± 85.3	-113.5± 83.6	-79.1 ± 139.3	52.8± 73.5
12	576.6± 97.2	25.8±104.2	106.9± 86.5	-34.0±104.2	-163.5± 168.5	160.1± 120.2	-48.8± 96.1	-94.6± 101.5	246.7 ± 133.7	-5.2± 101.5
13	755.6±102.5	29.6±114.8	137.4±104.9	-231.3±122.3	227.3± 162.5	68.7± 127.5	-41.9± 116.4	111.8± 121.5	-142.6 ± 148.9	202.0± 170.0
14	827.9±110.3	146.5±119.0	94.7±111.8	-81.2±108.3	-21.1± 173.3	-3.7± 147.7	17.0± 116.9	-44.7± 112.9	28.4 ± 164.6	-215.4± 141.2
15	332.1± 71.6	221.3±104.7	56.0± 70.1	-163.6± 99.2	73.6± 108.4	-69.0± 53.6	23.1± 78.8	-82.9± 102.6	138.3 ± 97.7	-28.0± 61.6
16	204.6± 53.3	7.9± 64.7	51.2± 52.3	-26.5± 59.1	17.9± 94.0	-78.0± 58.7	-52.3± 55.6	1.1± 66.5	-28.0 ± 76.9	31.6± 80.3
17	117.5± 43.2	13.2± 42.3	38.3± 38.9	38.2± 23.3	-64.9± 81.8	-67.6± 47.4	-36.6± 42.5	2.1± 43.8	-52.6 ± 57.5	-13.2± 30.9
18	114.0± 42.3	-12.9± 53.9	54.4± 37.9	-46.9± 65.1	1.4± 70.0	44.6± 54.8	-22.2± 41.1	-116.2± 68.0	25.1 ± 65.9	-12.2± 49.2
19	139.1± 44.4	-59.1± 42.3	144.5± 58.2	-93.5± 54.1	-53.3± 67.8	30.2± 37.1	-12.6± 54.5	-2.6± 53.2	-50.6 ± 79.6	65.5± 95.5
20	220.9± 64.8	113.3± 77.3	169.7± 77.7	185.2± 90.9	-46.0± 95.6	-0.3± 48.7	-22.7± 53.9	33.8± 55.1	-4.5± 111.3	-112.9± 66.4

Table 5. Efficiency corrected moments of the $J/\psi \to \gamma K^+K^-$ data

Bin	$T^0_{0,0}$	$T^2_{0,0}$	$T^0_{2,0}$	$T^2_{2,0}$	$T^2_{2,1}$	$T^2_{2,2}$	$T^0_{4,0}$	$T^2_{4,0}$	$T^2_{4,1}$	$T^2_{4,2}$
1	53.6±22.7	4.6±30.8	30.0±35.1	42.4± 43.8	-4.1± 18.4	-4.5± 20.5	44.5± 29.1	50.6± 31.5	17.1± 13.4	-4.6± 18.4
2	102.3±35.5	60.1±36.9	61.9±51.6	69.8± 54.7	37.6± 38.8	9.1± 13.6	47.4± 39.7	81.2± 46.6	38.1± 47.9	4.0± 16.2
3	105.6±34.9	36.5±43.1	17.5±50.6	39.9± 57.6	-52.6± 37.4	-19.3± 18.9	42.9± 58.5	49.1± 63.4	-26.3± 41.7	18.2± 16.9
4	57.0±20.8	-25.1±32.3	8.2±27.8	-48.1± 42.3	-99.3± 45.8	-21.3± 16.5	-2.3± 18.8	-12.3± 23.5	-86.9± 62.7	10.7± 26.0
5	230.4±61.6	4.1±52.1	198.9±97.7	84.3± 75.1	-9.9± 81.2	15.3± 32.7	70.6± 77.2	72.3± 62.3	16.5± 75.5	10.1± 51.6
6	264.5±54.3	15.4±71.5	51.6±75.3	8.7± 112.0	110.2± 103.5	61.7± 35.8	-28.5± 68.0	1.4± 82.8	-1.3± 98.9	30.0± 53.7
7	183.8±40.4	13.0±35.5	-24.8±44.9	11.9± 30.1	46.6± 64.8	-14.9± 39.8	-29.8± 44.6	-37.1± 46.7	-118.7± 76.5	-21.4± 49.5
8	262.9±51.8	86.5±70.2	3.3±67.3	-70.8± 106.2	-75.0± 80.6	51.1± 42.5	-57.2± 68.7	-82.7± 86.2	-110.2± 82.2	17.8± 59.5
9	637.6±72.4	-57.8±83.4	172.9±72.2	-62.9± 91.1	-94.6± 123.3	-24.2± 78.2	-143.2± 68.0	46.0± 85.4	-156.2± 96.1	253.6± 108.0
10	519.9±70.3	-173.1±69.3	336.9±80.8	-253.1± 84.2	-55.6± 118.9	31.6± 60.4	-125.3± 62.0	14.2± 66.8	-43.4± 110.8	99.2± 105.1
11	478.1±63.8	20.3±79.1	338.9±80.7	-15.4± 112.5	-102.7± 99.6	28.5± 56.0	36.5± 64.2	13.4± 75.2	130.2± 101.0	9.7± 84.8
12	508.4±64.6	24.5±67.5	91.9±74.4	-8.5± 76.6	-54.0± 103.2	-107.5± 70.8	-78.3± 55.0	-14.2± 64.9	-82.7± 120.4	-57.2± 89.2
13	733.4±75.7	97.6±76.4	17.0±75.6	-113.9± 85.3	79.3± 118.5	39.5± 87.2	-24.6± 70.9	63.5± 76.1	143.7± 126.1	107.1± 99.0
14	545.2±62.0	75.3±60.9	-25.7±55.3	-27.0± 59.6	111.9± 108.0	-84.6± 78.8	-141.9± 59.1	-101.1± 69.2	-16.4± 92.6	-5.6± 85.8
15	475.9±67.2	20.4±54.7	46.1±62.3	-22.7± 65.3	-98.3± 107.7	24.4± 78.9	-76.5± 57.7	104.8± 60.5	28.5± 85.0	93.1± 94.4
16	205.0±40.6	-9.1±30.0	-40.2±38.6	0.1± 30.9	-40.4± 57.8	16.6± 67.8	9.1± 36.6	-54.1± 33.1	-9.3± 50.4	21.1± 57.7
17	139.9±38.4	-11.2±29.3	-14.5±33.0	-24.6± 31.1	18.6± 58.5	64.4± 68.1	21.5± 33.3	-72.9± 31.7	33.0± 46.5	-39.3± 43.4
18	87.2±26.6	36.4±29.5	77.4±40.5	-14.0± 45.9	24.3± 40.3	-25.8± 23.9	36.6± 27.6	19.9± 34.4	-30.3± 49.7	28.5± 40.9
19	135.4±31.9	-43.4±28.1	45.9±37.2	-28.2± 32.8	-4.1± 42.6	28.8± 52.1	33.7± 25.8	-36.1± 27.9	13.4± 52.5	0.1± 44.3
20	233.1±46.3	0.6±39.3	114.2±51.3	29.5± 49.7	-6.6± 72.4	48.0± 60.4	-5.2± 39.5	22.6± 45.7	22.2± 72.4	38.2± 66.1

allowed to vary, except the phase angle of the amplitude $a_{2,0}$, which serves as the reference phase, and is fixed at zero. Twelve independent fits are conducted in each mass bin, each starting with a set of randomly generated values of the fit parameters. The results from the first six of these fits are plotted in Figs. 42, 43 and 44 (using different symbols for different fits), with the data for the decays $J/\psi \rightarrow \gamma K^0\overline{K}^0$, $J/\psi \rightarrow \gamma\ K^+K^-$, and the combined data for these two modes respectively. The combination of the data is the sum of the efficiency-corrected moments for the two modes. The results from other fits are not shown, since no significant deviation from the plotted results is obtained.

Though more than one solution is found in some mass bins (eg. the 7th bin of the $J/\psi \rightarrow \gamma K^0\overline{K}^0$ data), the results in any given mass bin are essentially consistent (note that ϕ and $\phi \pm 2\pi$ in a given mass bin correspond to the same solution; also, if all three phase angles have their signs reversed simultaneously, the calculated observables remain the same, since they depend only on the cosines of the relative phase angles). The general features of the results obtained from the individual decay modes and the combined data are also consistent: in the mass region of the $f_2'(1525)$, the spin 2 amplitudes dominate, while in the mass region of the $\theta(1720)$, the amplitude $a_{0,0}$ dominates. The result obtained in the $f_2'(1525)$ region is consistent with the previous MARK III measurement with the first half of J/ψ data,[38] while that in the $\theta(1720)$ mass region is somewhat controversial. The previous measurement in this region[38] made use of a spin hypothesis test, which compares the angular distribution of events in some selected mass regions to the expectations for a pure spin 0 and a pure spin 2 assumption. It concluded that the pure spin 2 hypothesis was favored over pure

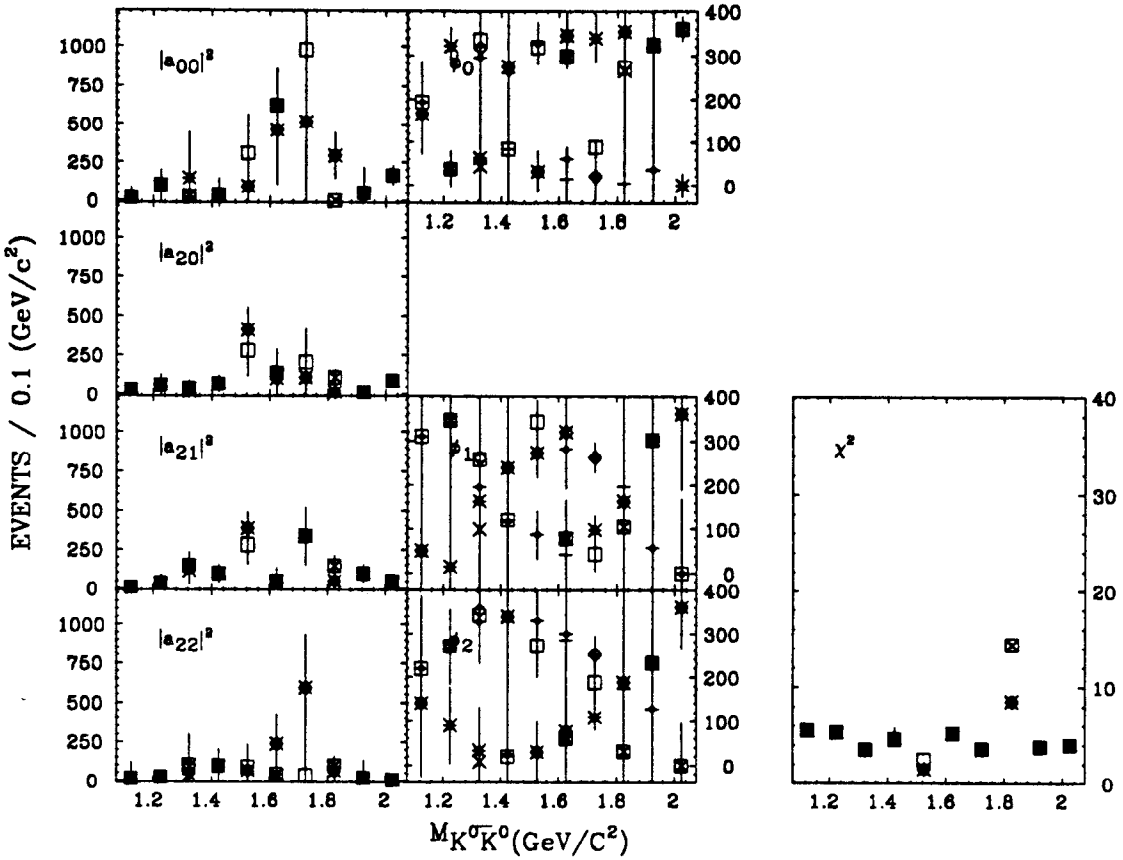

Figure 42. The amplitude distributions from the $J/\psi \to \gamma K^0 \overline{K}^0$ data. Six fit results are presented in each mass bin. The phase angles are measured relative to that of $a_{2,0}$.

spin 0 in both the $f_2'(1525)$ and $\theta(1720)$ regions. Because of the limited statistics of the first half of the MARK III J/ψ sample, a detailed amplitude analysis was not undertaken.

Since the analysis procedure is somewhat complex, the rest of this chapter will be devoted to tests of the fit procedure and of the amplitude results obtained.

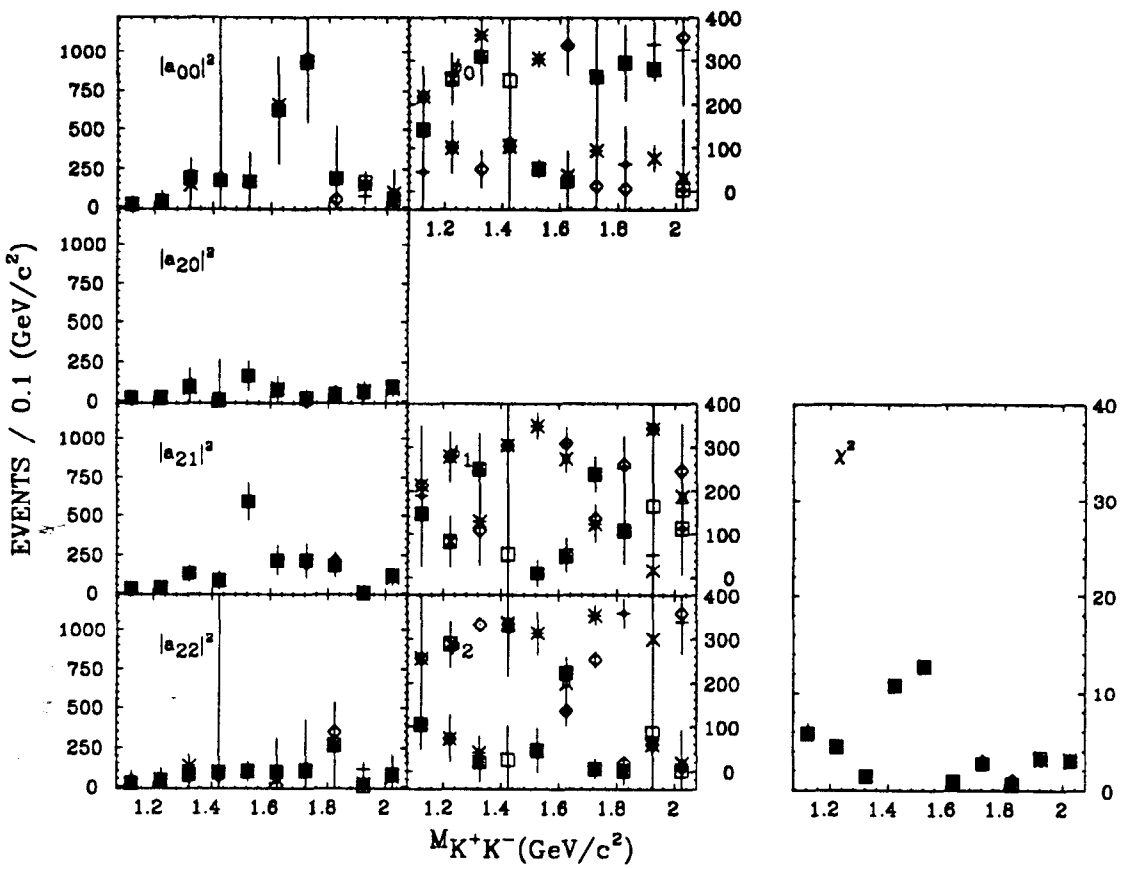

Figure 43. The amplitude distributions from the $J/\psi \rightarrow \gamma\ K^+K^-$data. Six fit results are presented in each mass bin. The phase angles are measured relative to that of $a_{2,0}$.

A quantitative discussion of these results is postponed to the next chapter, where Breit-Wigner resonance line shapes will be fitted to the distributions of the amplitude intensities, the phase angle information measured here will be compared with the predictions of the Breit-Wigner fits, and the features and contributions of the various resonances observed will be discussed.

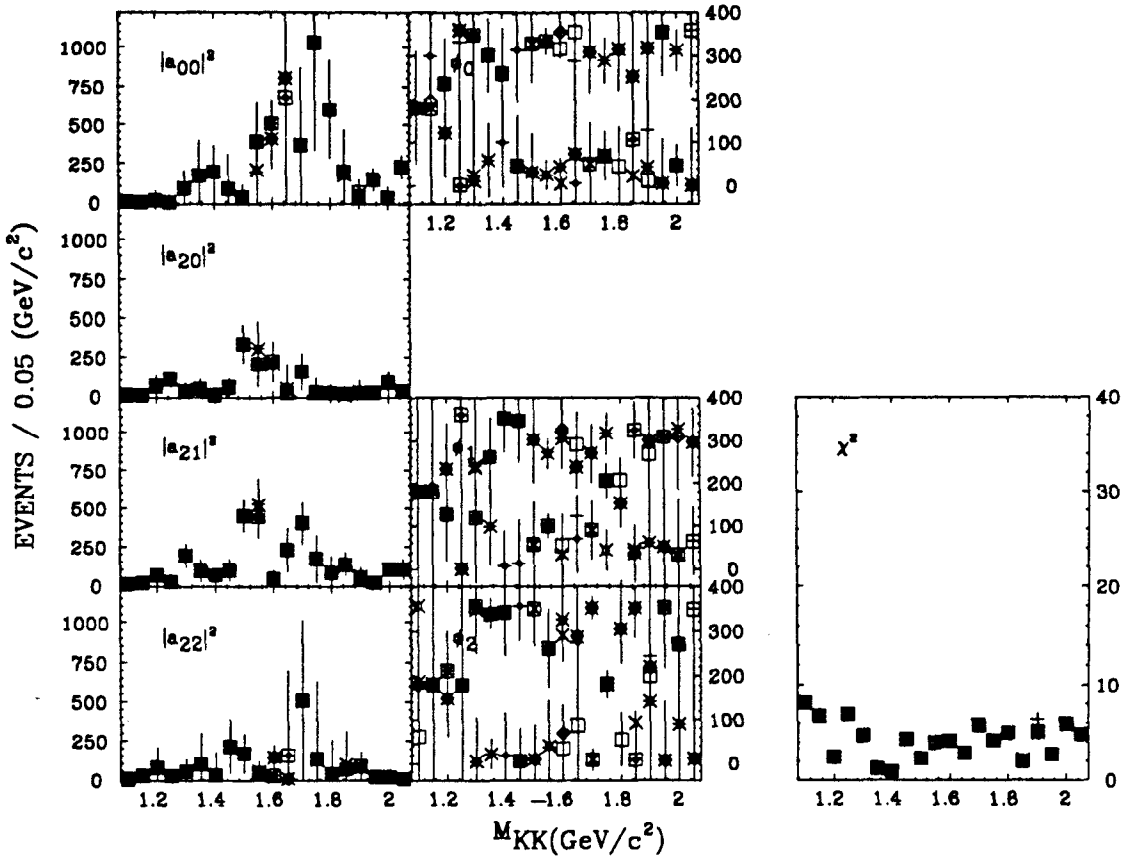

Figure 44. The amplitude distributions from the combined $J/\psi \to \gamma K^0\overline{K}^0$, $J/\psi \to \gamma\, K^+K^-$data. Six fit results are presented in each mass bin. The phase angles are measured relative to that of $a_{2,0}$.

The goodness of the amplitude fits is checked by comparing the measured moments to the predictions of the particular amplitude results modified to take account of the efficiency effects. This comparison is illustrated in Figs. 39, 40, where the data points, as pointed out earlier, represent the measured moments and the histograms represent the predictions resulting from the fits with

the lowest χ^2 in individual mass bins. These χ^2 values are plotted in the bottom left corner of each figure. Good agreement between the measured and predicted moments is observed.

In order to demonstrate the need for the large $a_{0,0}$ amplitude values obtained with the fit procedures, the moment-amplitude relations described in eq. 19) in the Appendix are combined linearly so as to project an amplitude combination which will be zero whenever the contribution of a_{00} is zero. The relevant relationship is as follows:

$$\sqrt{5}Re(a_{0,0}a^*_{2,0})+|a_{0,0}|^2 = \frac{2}{3}(T^0_{0,0}+\sqrt{5}T^2_{0,0})+\frac{\sqrt{5}}{3}(T^0_{2,0}+\sqrt{5}T^2_{2,0})-\frac{12}{9}(T^0_{4,0}+\sqrt{5}T^2_{4,0}) \tag{8}$$

The distribution of the quantity on the right hand side of this expression, as calculated from the measured efficiency-corrected moments of the $J/\psi \rightarrow \gamma\ K^+K^-$data, is plotted in Fig. 45. The need for a non-zero $a_{0,0}$ is clearly evident, especially in the $\theta(1720)$ mass region. It should be emphasized that this conclusion is independent of the fit procedure, and clearly illustrates the benefit, discussed previously, of obtaining the efficiency-corrected moments as an intermediate step in the procedure used to extract the underlying amplitudes.

Stability of the Amplitude Results

The stability of the amplitude results is tested by choosing alternative mass intervals and by using different event selection criteria. In order to avoid any possible confusion, it should be pointed out that the alternative measures taken in this section are for test purposes only; none of them is applied in obtaining

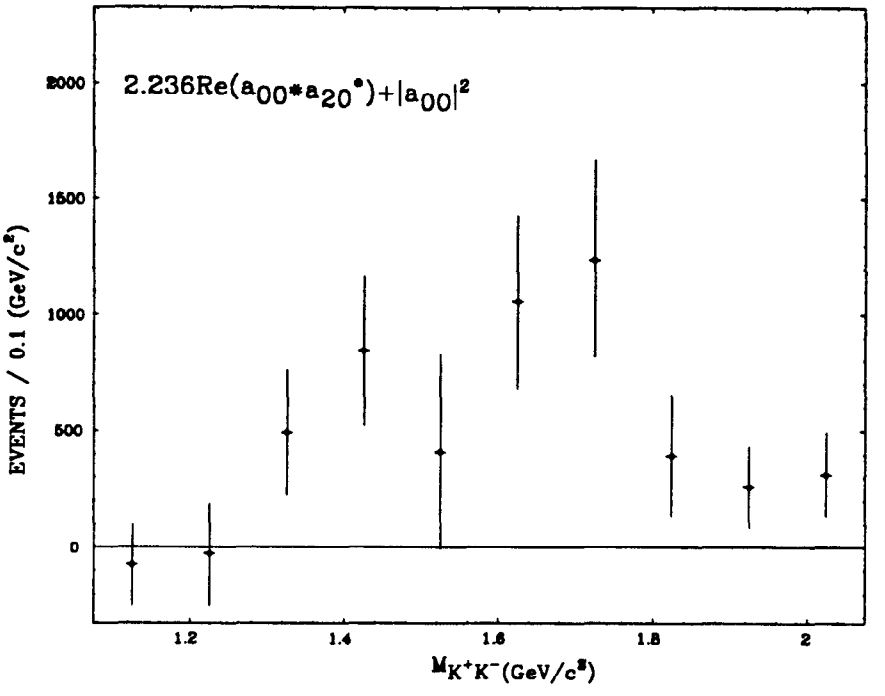

Figure 45. The distribution of the combination of moments in eq. (8) for the $J/\psi \rightarrow \gamma\ K^+K^-$data. This combination should be identically zero in the absence of the spin 0 amplitude. This is clearly not the case, especially in the $\theta(1720)$ mass region, and indicates the need for the large $a_{0,0}$ amplitude found by the fit procedure.

the results reported in other sections. The mass bins and event selection criteria described previously will be referred to as the standard ones in this section.

To verify that the amplitude results are independent of the mass intervals selected, and that any enhancements in the amplitude distributions are not due to the particular choice of binning, the same analysis is repeated using mass intervals which are different from the standard ones. For example, if the lowest limit of the mass region under study is displaced by half a bin width, each new bin overlaps a pair of old bins, and all bins have the same width as before. It follows that the amplitude results for the new bins should essentially interpolate those from the old neighboring bins if the results are independent of the choice of

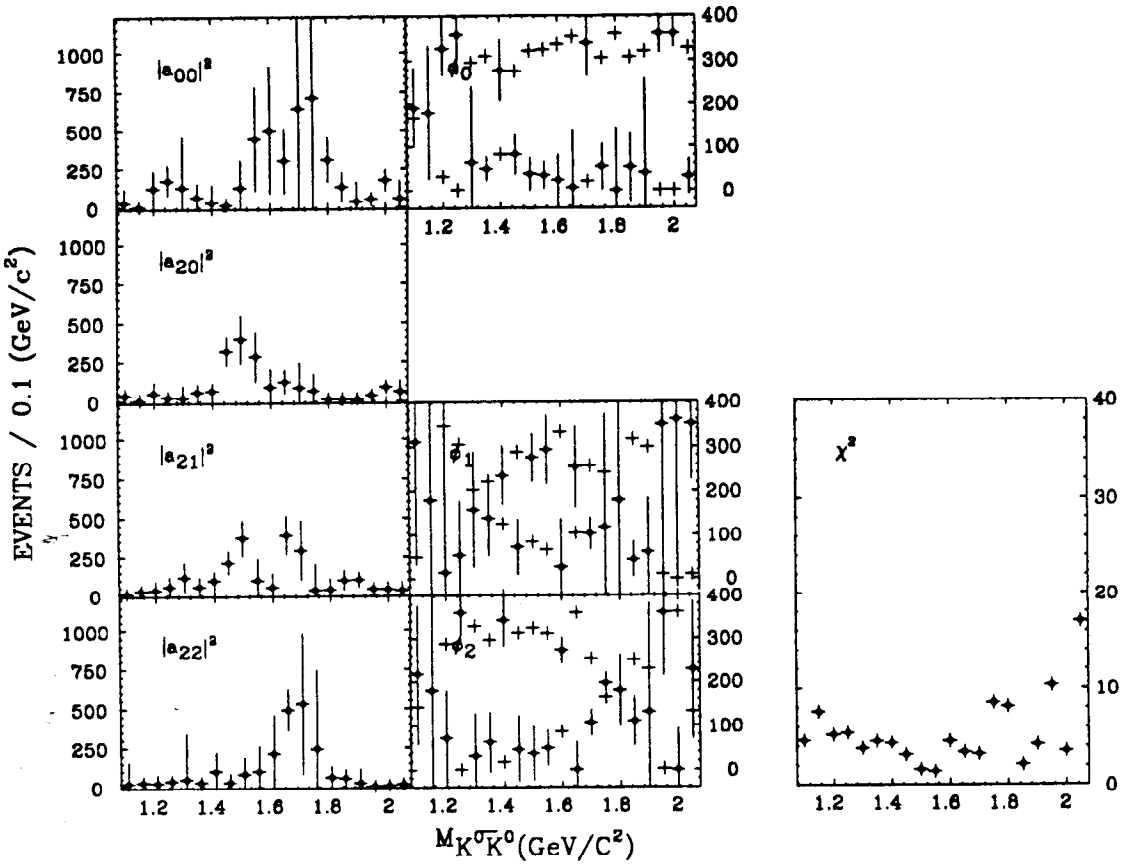

Figure 46. The amplitude distributions for the $J/\psi \to \gamma K^0\overline{K}^0$ data with overlapping bins. Bin width: $100MeV/c^2$, overlap region: $50MeV/c^2$. The crosses (with no error bars) in the phase angle plots correspond to $2\pi - \phi$, where ϕ is the fitted value in the range $0 \sim 2\pi$.

binning. The results obtained from the data of the two decay modes are plotted in Figs. 46 and 47 respectively. In these plots, only the fit which converges to the lowest χ^2 in each mass bin is plotted, since the results of the multiple fits for the same mass bin are consistent with each other, as shown in Figs.

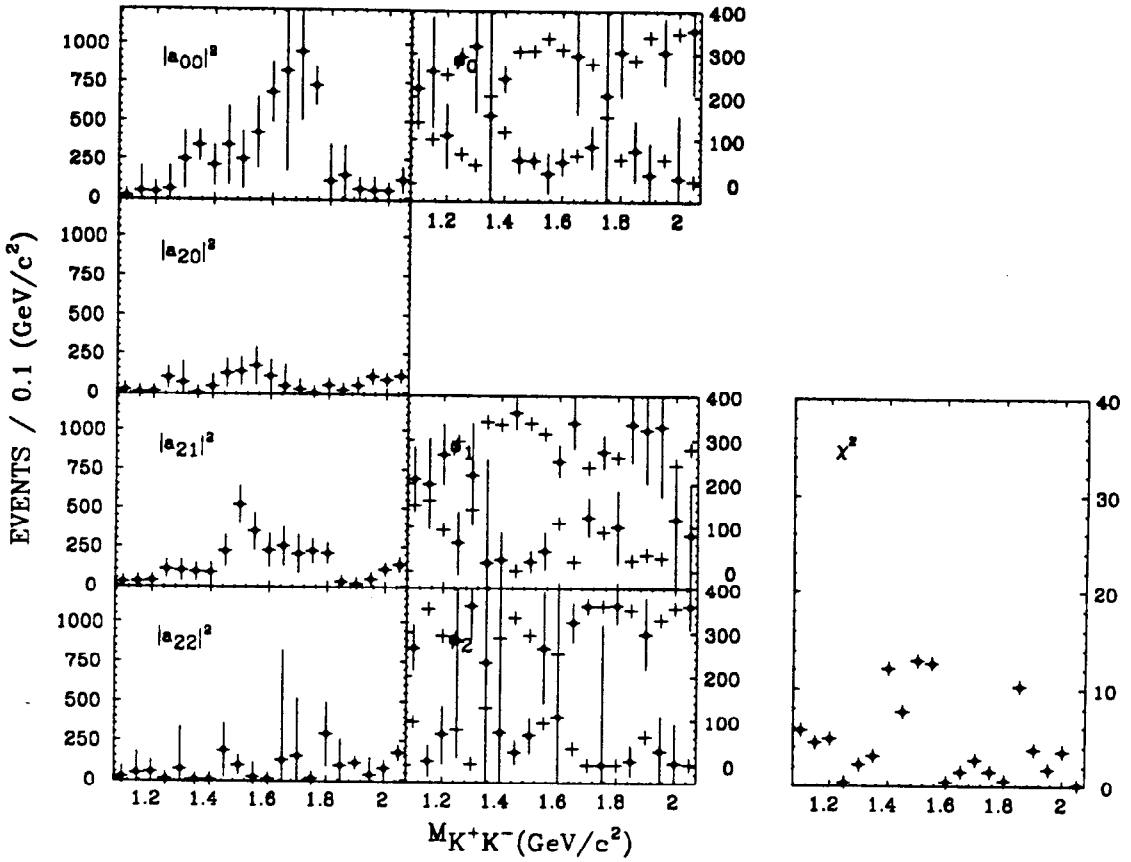

Figure 47. The amplitude distributions for the $J/\psi \rightarrow \gamma\ K^+K^-$data with overlapping bins. Bin width: $100MeV/c^2$, overlap region: $50MeV/c^2$. The crosses (with no error bars) in the phase angle plots correspond to $2\pi - \phi$, where ϕ is the fitted value in the range $0 \sim 2\pi$.

42, 43 and 44. The fitted value, ϕ, of each phase angle in the range 0 to 2π is shown as a data point with an error bar attached. In addition, the value $2\pi - \phi$ is also plotted as a point without error bar. This is equivalent to simultaneously reversing the sign of all three relative phase angles. The results from the new

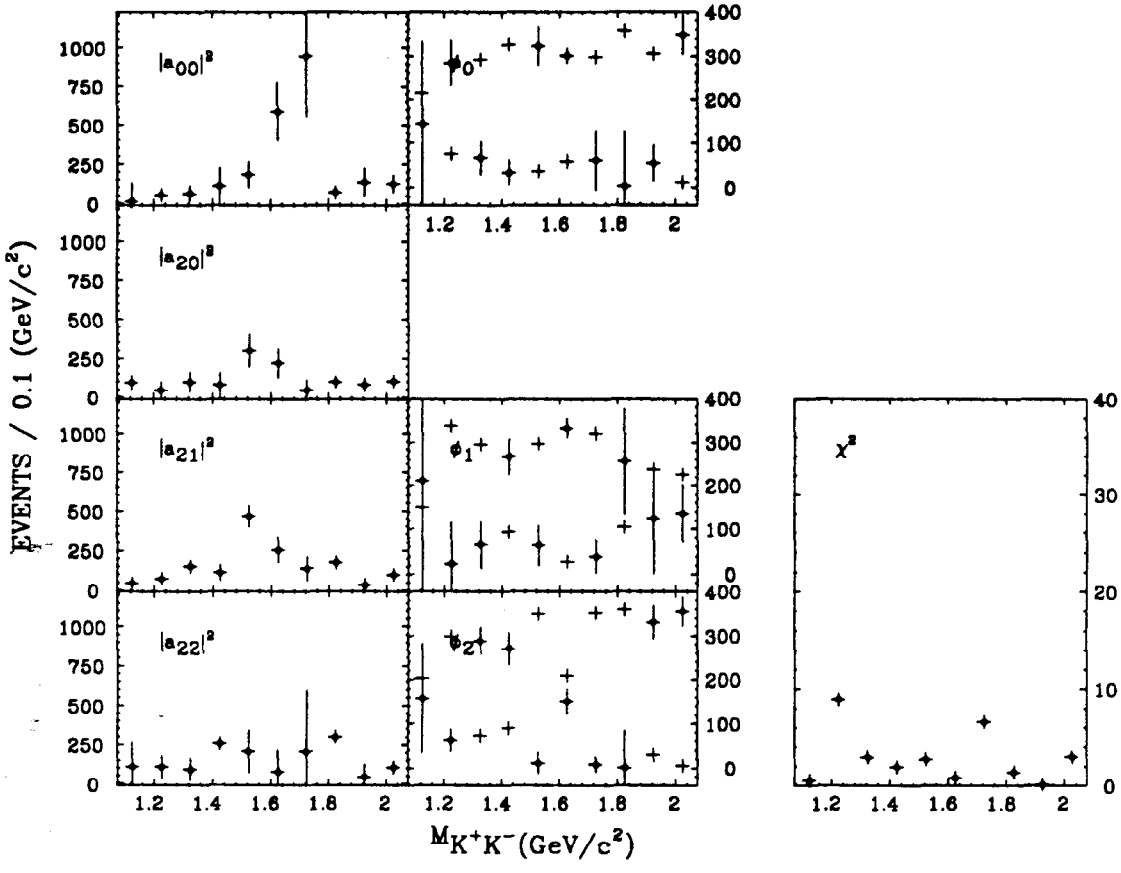

Figure 48. The amplitude distributions from the γ K^+K^-data with the TOF identification requirement on only one charged track.

bins match rather well with those from the neighboring old bins, and the basic features obtained with the standard binning remain. This indicates that the results are bin independent.

There is a minor efficiency discrepancy between the Monte Carlo simulation and the true detection efficiency in the region of small lab polar angle for the charged tracks; this has been observed using the data for other high statistics

decay modes. Consequently, the present analysis is tested by cutting on different values of the cosine of this angle for the charged tracks from the $J/\psi \rightarrow \gamma$ $K_s K_s$ decay. With the cosθ cut varying from 1.00 to 0.80 in steps of 0.05, the amplitude distributions are checked. Though the results vary slightly with the cut value, the basic features remain the same as those obtained with no cut on this quantity. The slight variations in the results may be due to some extent to the inaccuracy of the efficiency simulation, but in the main, it results from the variation of the available phase space, since the precision of the analysis procedure degrades as the available cosθ region decreases.

Since the Time of Flight requirement on both charged tracks in the $J/\psi \rightarrow$ γ K^+K^-decay is approximately equivalent to a cosθ cut, the stability of the results obtained with the γ K^+K^-data is tested by removing the TOF criterion on one of the charged tracks, ie. by requiring that only one charged track be recorded in the TOF counters and identified as a kaon track. With this modification, the available phase space is expanded, and the demands on track quality are relaxed, thus leading to a sample with higher statistics which contains more contamination from background events than the standard sample. The amplitude results obtained with this sample are plotted in Fig. 48. The basic features of the amplitude results of Fig. 43 remain the same within error. However, for the purposes of the present analysis, the TOF requirement on both charged tracks is retained in order to ensure a higher quality, if lower statistics, data sample.

The Fit to the $\theta(1720)$ Mass Bin

Since the fit results obtained in the $\theta(1720)$ mass region are the most interesting ones in this analysis, the goodness of the fits conducted in the mass bin where the $\theta(1720)$ resonance peaks is checked further. In this section, only the results from the lowest χ^2 fit to the $J/\psi \rightarrow \gamma\, K^+K^-$ data are discussed, since, as pointed out earlier, the results from the two decay modes and from the multiple fits in the same mass bin agree within error.

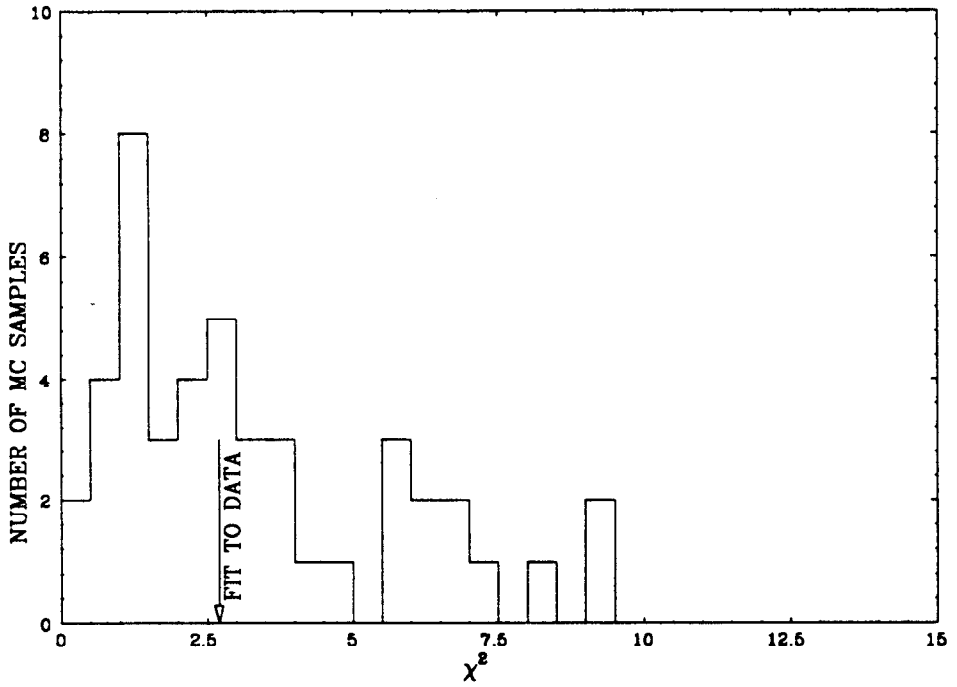

Figure 49. The goodness of the fit to the data in the θ mass bin. The χ^2 of the standard fit to the data (arrow), is compared to the χ^2 values for fits to Monte Carlo samples (histogram).

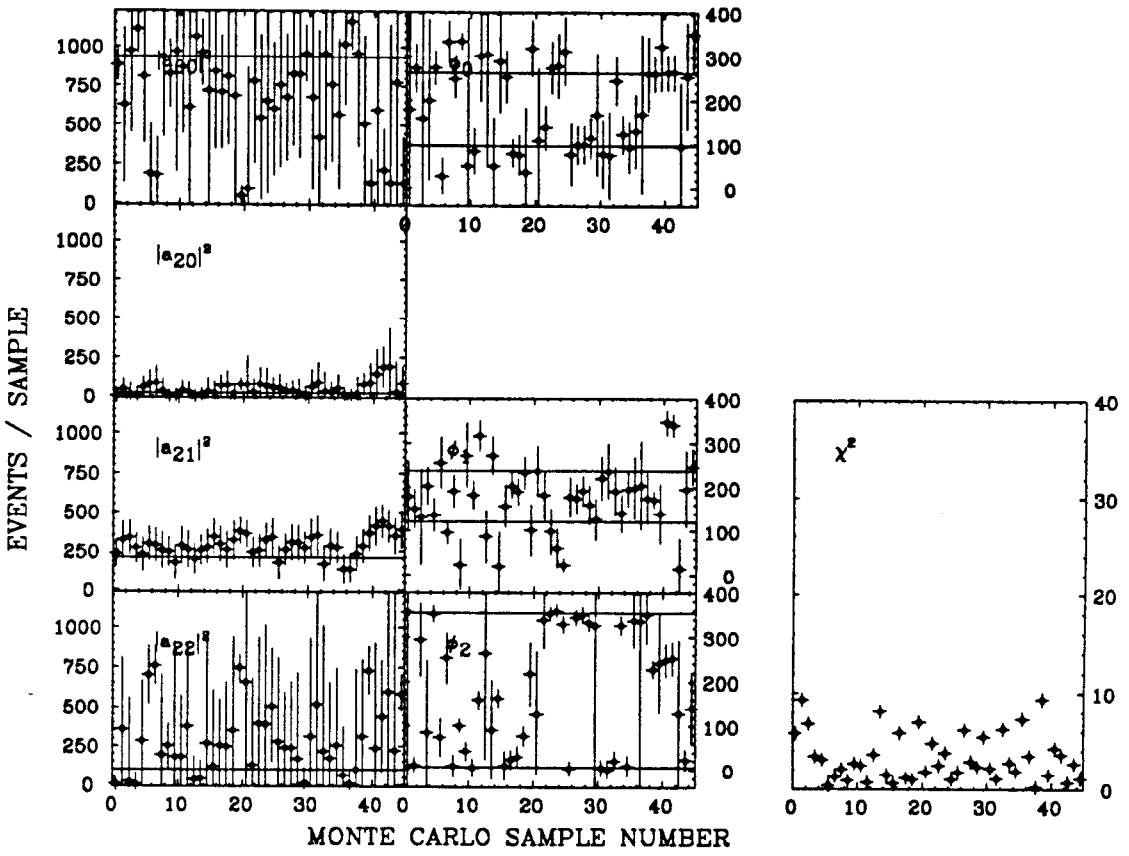

Figure 50. A test of the stability of the fit. A comparison of the results obtained with the Monte Carlo samples (data points) and the input values (solid lines).

To check the goodness of this fit, forty-five independent Monte Carlo samples are generated with input amplitudes equal to those obtained from data. The χ^2 of the fit to the data is then compared to the values obtained from the Monte Carlo samples in Fig. 49. Clearly, the χ^2 of the fit to the data, marked by the arrow in the plot, is near the average of the values obtained for the fits

to the Monte Carlo samples (the distribution of the latter is described as the histogram). This agreement indicates that the fit to the data is reasonable.

To check the stability of the fit procedure, the amplitude results obtained from the Monte Carlo samples are compared with the input values. As shown in Fig. 50, the results from the majority of the samples are consistent with the input values, which indicates that the fit procedure is stable and that the chance for it to end with a wrong solution is small.

To investigate the possibility that the $\theta(1720)$ mass region corresponds to pure spin 2 intermediate states (the favored hypothesis obtained with the previous measurements[38]), fits with pure spin 2 amplitudes (ie. with $a_{0,0}$ fixed at zero) to the data over all the mass bins are carried out; in particular, the fit to the $\theta(1720)$ mass bin is checked in the same way as the standard fit to this mass bin, as described previously. The results of the pure spin 2 fit are shown in Fig. 51 for the amplitude distributions, and in Fig. 52 for the moment comparison. Fig. 53 shows the χ^2 values obtained for pure spin 2 fits to Monte Carlo samples generated using the amplitude values obtained from the pure spin 2 fit to the data in the $\theta(1720)$ mass bin. As shown in Fig. 53, the χ^2 for the fit to the data is beyond the entire χ^2 distribution for the Monte Carlo samples. This indicates that the fit with a pure spin 2 model to the data is not good.

Based on the tests described above, it is concluded that a non-zero scalar component is necessary to describe the data in this bin. However, it is also necessary to estimate the amount of real spin 2 which may be misidentified as spin 0. To estimate the maximum amount of spin 0 in the data which might

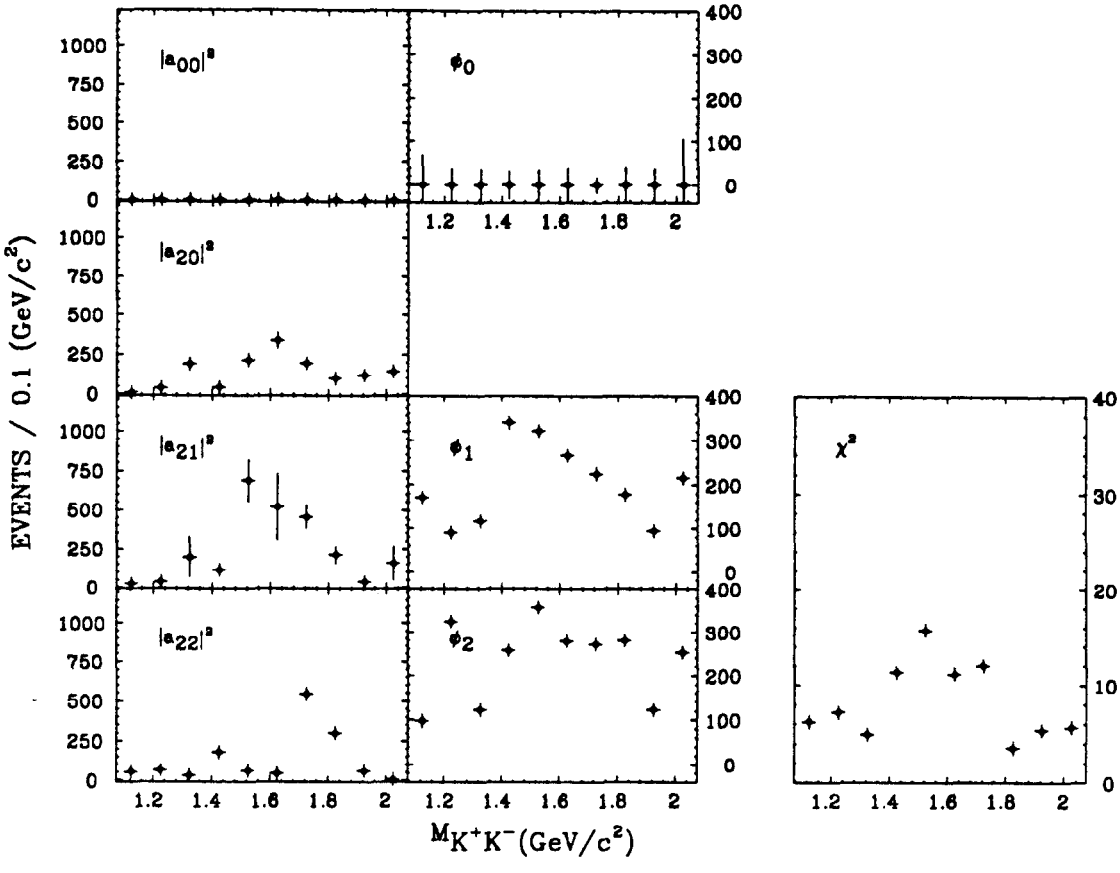

Figure 51. The amplitude results for pure spin 2 fits to $J/\psi \to \gamma\, K^+K^-$ data. The results in the 7th bin are consistent with those obtained in the previous analysis with a pure spin 2 hypothesis in the $\theta(1720)$ mass region.

result from misidentified spin 2, the standard fit procedure is applied to the Monte Carlo samples of pure spin 2 events generated and used above. The distribution of the fraction of Monte Carlo events which are misidentified as spin 0 is plotted as the histogram in Fig. 54. This should indicate the maximum

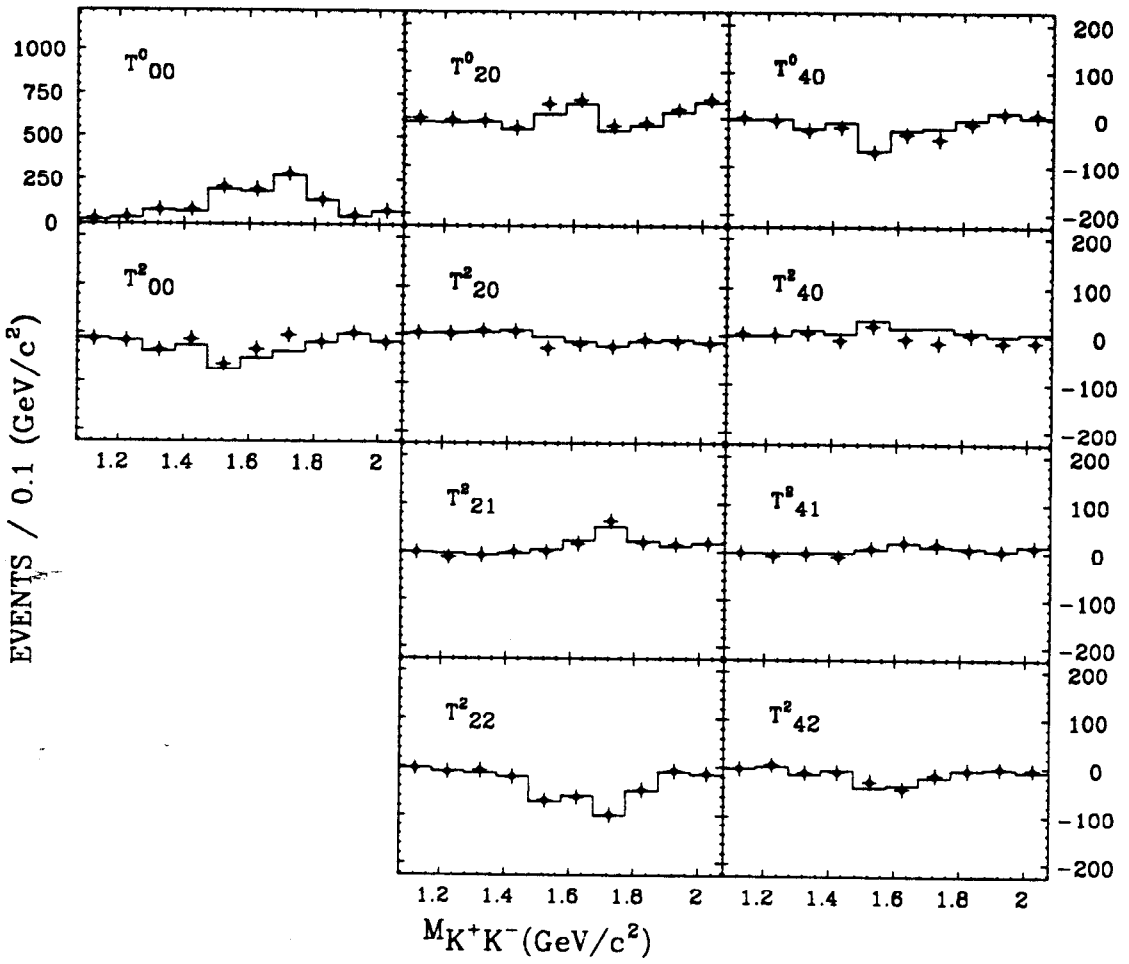

Figure 52. A comparison of the measured moments and the predictions based on the amplitude results from the pure spin 2 fits to the $J/\psi \rightarrow \gamma K^+K^-$ data. The χ^2 values of the corresponding fits are shown in Fig. 51.

fraction of misidentified events, since the number of $a_{2,2}$ events in these Monte Carlo samples corresponds to the maximum amount that could possibly be in the data. The fraction of real spin 0 events obtained in the $\theta(1720)$ mass bin by the analysis procedure is indicated by the arrow in the figure; this is well above

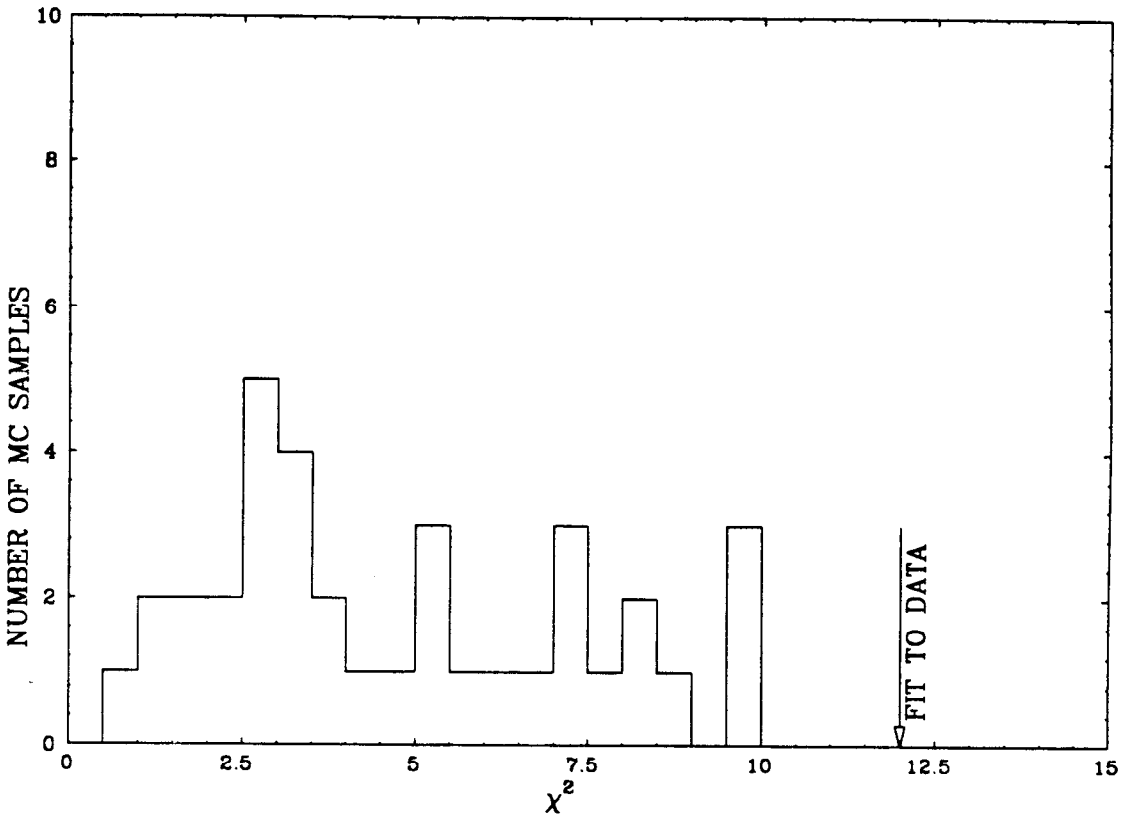

Figure 53. The goodness of the spin 2 fit to the data in θ mass bin. The χ^2 of the fit with pure spin 2 to data (arrow) is compared to the χ^2 values for fits to Monte Carlo samples generated with pure spin 2 amplitudes (histogram).

the average value, and is even beyond the maximum value of the histogram. This test clearly establishes that the spin 0 enhancement in the $\theta(1720)$ mass region is real, and does not result from the misidentification of spin 2 contributions.

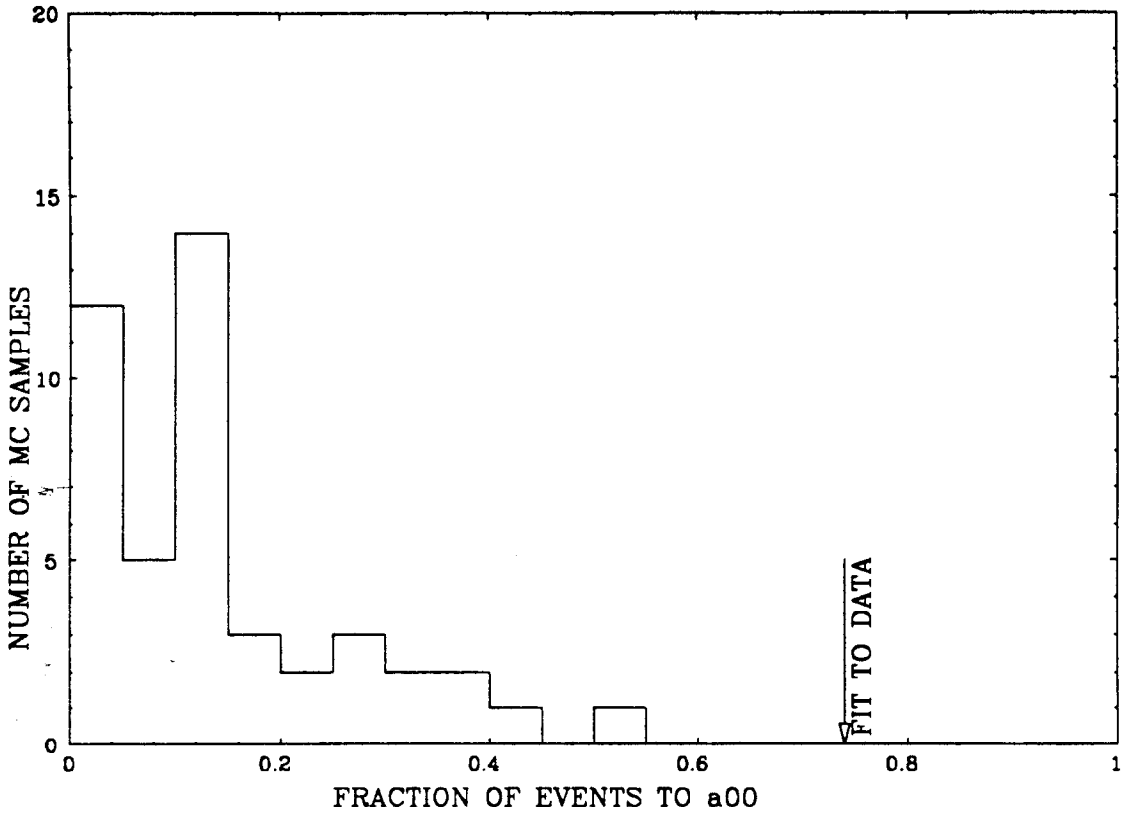

Figure 54. The fraction of events identified as spin 0 for the $\gamma\ K^+K^-$ data in the θ mass bin (arrow), and the corresponding values for Monte Carlo samples generated with pure spin 2 amplitudes (histogram).

Comparison with the Previous Analysis of the $\theta(1720)$ Region

To compare this analysis with the previous one conducted on the $\theta(1720)$ mass region,[38] hypothesis tests are formed which are similar to those made in that analysis. The same J/ψ sample, and the "full" and "restricted" mass regions used in that analysis are used for comparison purposes. In order to test

Table 6. Comparison of the probabilities of the spin 0 and spin 2 hypotheses for the present and the previous studies.

Spin	$1.60 - 1.85$ GeV/c^2	$1.675 - 1.85$ GeV/c^2
0	$\chi^2 = 25.8$, ln**L** $= -644.9$	$\chi^2 = 22.4$, ln**L** $= -438.8$
2	$\chi^2 = 6.9$, ln**L** $= -636.5$	$\chi^2 = 6.6$, ln**L** $= -432.9$

the pure spin 0 hypothesis, all spin 2 amplitudes are set to zero; conversely, to test the pure spin 2 hypothesis, the spin 0 amplitude is set to zero. The χ^2 values of the fits in these mass regions, and the likelihood values quoted in the previous analysis,[38] are tabulated in Table 6. As the results show, the χ^2 values for the pure spin 2 hypothesis are smaller than those for pure spin 0 in both mass regions, which means that the pure spin 2 hypothesis is favored over pure spin 0 by the present analysis method, also. The conclusions drawn in the previous analysis are based on the value of the likelihood function in the sense that the larger ln**L**, the more likely it is that the hypothesis describe the data. It follows that the two hypothesis tests are consistent.

The exclusion of the pure spin 0 hypothesis by both analyses may be due to the fact that, although spin 0 is dominant, some spin 2 events are indeed present in these mass regions, as the amplitude analysis in previous sections indicates. The small amount of spin 2 events may be partly from the tail of the nearby $f_2'(1525)$ resonance, and partly from some additional spin 2 activity on the high mass side of this mass region. The angular distribution of spin 0 events is flat over the helicity angles in the $K\overline{K}$ frame and has a $1 + cos^2\theta$ dependence on

$\cos\theta_{K\overline{K}}$ in the lab frame; in contrast, a combination of spin 2 amplitudes yields a broad range of possibilities for these distributions. It follows that, in making the pure spin hypothesis tests, the spin 0 distributions are much more restricted in their possibilities, and are incapable of adequately reproducing the features of the angular distributions due to the small spin 2 amplitude contributions. In contrast, it is possible to find a pure spin 2 amplitude combination which will reproduce the observed distributions fairly well, thereby yielding a lower χ^2 for spin 2 in the present analysis, and a larger LnL value in the previous analysis. It is for this reason that spin 2 was favored in the previous analysis of a sub-set of the MARK III data.

CHAPTER VI

BRANCHING FRACTIONS AND DISCUSSION

In this chapter, the branching fractions are calculated for J/ψ radiative decay to $K\overline{K}$ through the resonances exhibited in the amplitude distributions obtained in the previous chapter. To be specific, these resonances are the spin 2 states $f_2(1270)$ and $f_2^{'}(1525)$, and spin 0 states in the mass regions of the $f_0(1400)$ and $\theta(1720)$. For the spin 2 resonances, the ratios of the different helicity amplitudes are also calculated for each resonance. The contribution of a possible spin 2 structure in the mass region of the $\theta(1720)$ will also be considered. The results will be compared to those from experiments introduced in chapter 1.

In order to calculate the branching fractions, two methods are used. In the first method, the events associated with each amplitude are summed over a given mass interval, and the resulting total number of events is divided by the total number of J/ψ events analyzed. The branching fractions obtained with this method are referred to as the production branching fractions, since no resonance assumption is relied on. In the second method, Breit-Wigner line shapes (described in the last section of the Appendix) are fit to the distributions of the amplitude intensties to measure the mass and width of each resonance, and hence the number of events associated with each resonance is obtained. These branching fractions are referred to as the resonance branching fractions.

For comparison of the two $K\overline{K}$ decay modes, the production branching fractions are calculated for each mode as well as for the combined data of the two modes. The resonance branching fractions, however, are calculated for the combined data only, since high statistics and fine binning are required for reliable Breit Wigner fits.

Since the amplitude results obtained from the moments with the multiple fit procedures on each mass bin are essentially consistent with each other, the fit which converges to the lowest χ^2 value is used to represent the results. The minor deviations of the other fit results are taken into account in the estimate of the systematic error associated with the branching fraction value.

Production Branching Fractions

For the $J/\psi \rightarrow \gamma K^0\overline{K}^0$ and $J/\psi \rightarrow \gamma K^+K^-$ samples, and for the combined data of these two modes, the observed events attributed to each amplitude are summed over given mass intervals. The production branching fraction is defined as the ratio of the number of events associated with the particular amplitude for a given mass interval, and the number of J/ψ events analyzed; the latter is 5.8×10^6 with an uncertainty of 8.5%. The mass interval is chosen in such a way that it spans the peak region of the resonance under study. The production branching fractions for these samples are listed in Table 7; the error are purely statistical. These results provide a consistency check of the amplitude results obtained from the data of the individual decay modes, and from the combined data of the two modes.

Table 7. The production branching fractions ($\times 10^4$) for various amplitudes in the specified mass ($M_{K\overline{K}}$) intervals

Amplitude	1.075 – 1.475 (GeV)	1.475 – 1.575 (GeV)	1.575 – 1.975 (GeV)
	$J/\psi \to \gamma K^0 \overline{K}^0$		
$\|a_{0,0}\|^2$	191 ± 222	91 ± 132	1310 ± 655
$\|a_{2,0}\|^2$	188 ± 107	409 ± 144	232 ± 212
$\|a_{2,1}\|^2$	287 ± 118	385 ± 105	528 ± 228
$\|a_{2,2}\|^2$	223 ± 185	66 ± 100	907 ± 364
	$J/\psi \to \gamma K^+ K^-$		
$\|a_{0,0}\|^2$	413 ± 224	166 ± 185	1924 ± 528
$\|a_{2,0}\|^2$	167 ± 147	160 ± 93	198 ± 123
$\|a_{2,1}\|^2$	271 ± 83	591 ± 123	611 ± 169
$\|a_{2,2}\|^2$	226 ± 194	95 ± 66	428 ± 295
	$J/\psi \to \gamma K^0 \overline{K}^0 + J/\psi \to \gamma K^+ K^-$		
$\|a_{0,0}\|^2$	552 ± 374	420 ± 274	3586 ± 1003
$\|a_{2,0}\|^2$	306 ± 127	534 ± 187	490 ± 249
$\|a_{2,1}\|^2$	543 ± 138	897 ± 169	1121 ± 288
$\|a_{2,2}\|^2$	507 ± 337	204 ± 142	957 ± 760

Resonance Branching Fractions

The distributions of the amplitude intensities obtained with the combined $J/\psi \to \gamma K^0 \overline{K}^0$ and $J/\psi \to \gamma K^+ K^-$ data are plotted as the data points in Fig.

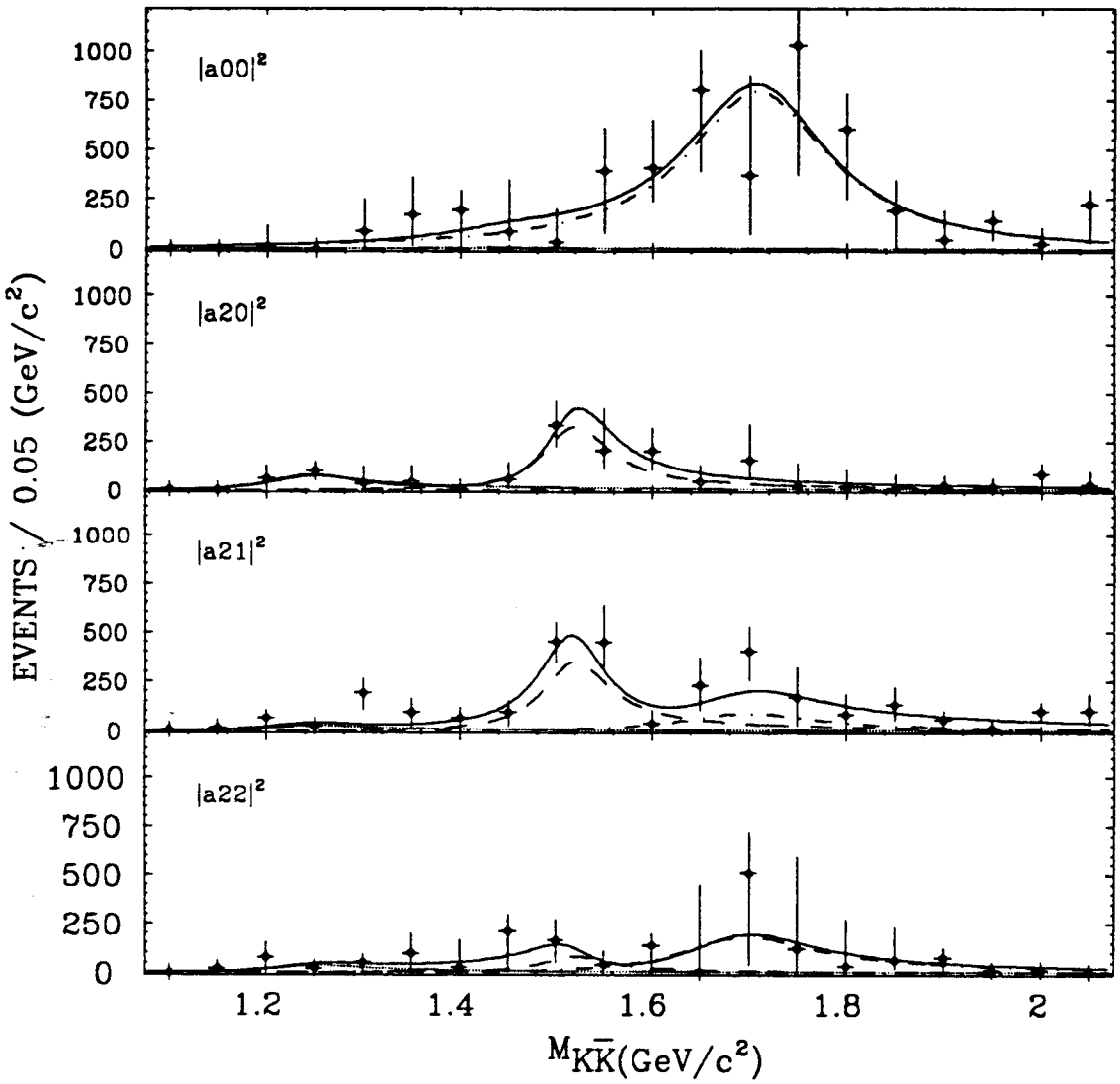

Figure 55. The results of fitting Breit-Wigner line shapes to the amplitude intensity distributions of the combined $J/\psi \to \gamma K^0 \overline{K^0}$ and $J/\psi \to \gamma\ K^+K^-$ data. The solid curves correspond to the coherent superposition of the individual Breit-Wigner resonances (the broken curves) fit to the data points.

55. These results are from the fits which converge to the lowest χ^2 among the

multiple fits (cf. Fig. 44) in each mass bin. In order to estimate the errors of the amplitude values accurately, the MINOS error search procedure in the program MINUIT[57] is used. The asymmetric errors obtained correspond to one unit change in χ^2 value while minimization in the subspace of all other parameters is carried out. The solid curves in the plots are obtained from the coherent superposition of the individual relativistic Breit-Wigner resonances (denoted by the broken curves) fit to the first 18 data points in each plot; the 2 data points beyond 2 GeV/c^2 are not included in the fits, since $K^*\overline{K}$ background events contribute in this region.

To fit Breit-Wigner line shapes to the data, a χ^2 contribution is obtained for each mass bin of each amplitude intensity distribution, using the data point, the asymmetric error estimated and the average value of the fit function over the mass bin in question. For the spin 0 amplitude, two interfering resonances are fitted. The mass and width of the first resonance are fixed to the values obtained for the $f_0(1400)$ in a similar analysis of the $J/\psi \rightarrow \gamma\pi^+\pi^-$ data;[45] those of the second resonance are to be determined. For the spin 2 amplitudes, two interfering resonances, the $f_2(1270)$ and the $f_2'(1525)$ are included, with their masses and widths fixed to the values quoted by the Particle Data Group.[2] An additional spin 2 resonance is introduced in the mass region of the $\theta(1720)$ to evaluate the contribution of a possible tensor in that region. In order to compare the branching fractions of the spin 0 and the possible spin 2 resonances in the $\theta(1720)$ region, the mass and width of the tensor are fixed to the values obtained for the scalar, which are 1710 and 186 MeV/c^2 respectively. The mass, width

and branching fraction for each of the resonances fit to the amplitude intensities are listed in Table 8.

The branching fraction is the ratio of the number of events in the fit region corresponding to the particular resonance to the number of J/ψ events analyzed. The first error listed is the statistical error, which is obtained from the Breit-Wigner fit. The second is the systematic error, which is estimated by means of fits to the amplitude results obtained with the various event selection criteria and the multiple fits to the moments, and also includes the uncertainty in the number of J/ψ events analyzed, the possible feedthrough among different amplitudes, and the contribution from background events.

For the tensor resonances, the resulting total branching fractions and the ratios of the different amplitude intensities are listed in Table 9.

Table 9. Branching Fraction results for the tensor resonances

Resonance	Total Bf($\times 10^4$)	$\frac{\lvert a_{21}\rvert^2}{\lvert a_{20}\rvert^2}$	$\frac{\lvert a_{22}\rvert^2}{\lvert a_{20}\rvert^2}$
$f_2(1270)$	$0.90 \pm 0.11 \pm 0.07$	0.32 ± 0.28	0.48 ± 0.36
$f_2'(1525)$	$3.45 \pm 0.52 \pm 0.28$	1.08 ± 0.31	0.25 ± 0.24

The values for the $f_2(1270)$ are poorly determined because of the low statistics and the weak coupling of this state to $K\overline{K}$.

Table 8. Mass, width and branching fraction of resonances fit to the various amplitude intensities

Resonance	Mass (MeV/c^2)	Width (MeV/c^2)	Bf ($\times 10^4$)	ϕ
Resonances fit to $\mid a_{00} \mid^2$ ($\chi^2/DOF = 21/13 = 1.6$)				
$f_0(1400)$	1440	160	0.05±0.16±0.01	0^0
$f_0(1710)$	1710 ± 20	186 ± 30	6.47±1.14±0.84	$88^0 \pm 80^0$
Resonances fit to $\mid a_{20} \mid^2$ ($\chi^2/DOF = 14.8/15 = 0.99$)				
$f_2(1270)$	1275	185	$0.50 \pm 0.13 \pm 0.06$	0^0
$f_2'(1525)$	1525	90	$1.48 \pm 0.26 \pm 0.19$	$-10^0 \pm 23^0$
A possible f_2		Not	included	
Resonances fit to $\mid a_{21} \mid^2$ ($\chi^2/DOF = 64.5/13 = 5.0$)				
$f_2(1270)$	1275	185	$0.16 \pm 0.06 \pm 0.02$	0^0
$f_2'(1525)$	1525	90	$1.60 \pm 0.29 \pm 0.20$	$38^0 \pm 27^0$
A possible f_2	1710	186	$0.66 \pm 0.22 \pm 0.09$	$44^0 \pm 36^0$
Resonances fit to $\mid a_{22} \mid^2$ ($\chi^2/DOF = 16.4/13 = 1.3$)				
$f_2(1270)$	1275	185	$0.24 \pm 0.10 \pm 0.03$	0^0
$f_2'(1525)$	1525	90	$0.37 \pm 0.34 \pm 0.05$	$133^0 \pm 50^0$
A possible f_2	1710	186	$1.36 \pm 0.62 \pm 0.18$	$119^0 \pm 63^0$

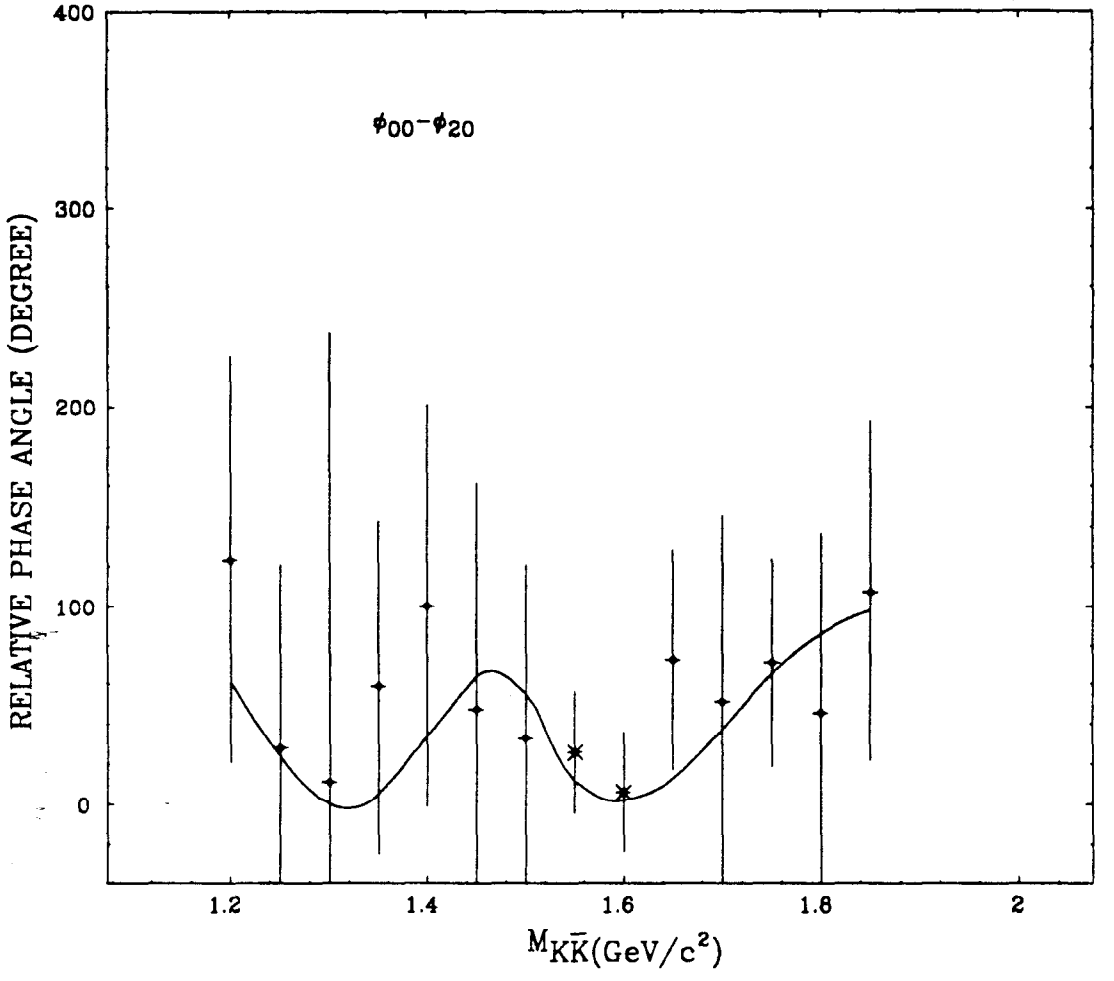

Figure 56. The relative phase $\phi_{00} - \phi_{20}$. The curve is the prediction from the resonances fitted to the amplitude intensities. The data points are extracted from the fits to the moments; those marked by crosses are reasonably measured.

The relative phase angles of the amplitudes predicted from the resonance line-shape fits to the amplitude intensities may be compared to those extracted from the fits to the moments. The comparison is shown in Fig. 56 for $\phi_{00} - \phi_{20}$. The curve is the prediction, while the data points are those extracted from the fits to the moments. The prediction agrees quite well with the data; however, this should not be over-emphasized, since there are only two data points (marked by

crosses) which are reasonably measured, namely those for which have both the relevant measured amplitudes differ from zero by more than one sigma. As Fig. 56 shows, the other data points have large errors. The phase angles between the tensor amplitudes are also examined in the same way, but no conclusion can be made due to the large uncertainty in the measurements of these quantities.

Discussion of the Spin 0 Resonances

Of the scalars introduced in the first chapter, only the one with mass around 1700 Mev/c^2 obviously appears in the distribution of the scalar amplitude intensities (Fig. 55). However, since the $f_0(1400)$ is evident in the $J/\psi \rightarrow \gamma\pi^+\pi^-$ data,[45] it is included in the fit to the $J/\psi \rightarrow \gamma K\overline{K}$ data, and will be discussed here. The broad resonance, the $f_0(1590)$, will also be considered since there is some speculation that this resonance may have some connection to the $f_0(1400)$ and $f_0(1710)$. The states $f_0(975)$, $f_0(1240)$, $f_0(1525)$ do not appear in the data, therefore no further discussion of these states will be made.

The mass and width of the dominating scalar in the present data sample match those of some measurements of the $f_0(1750)$ discussed in chapter 1. The interpretation of this state is an open question. It may be a scalar glueball, because of its production in the gluon-rich J/ψ radiative decay, and its absence in the quark-rich channels, such as peripheral hadronic processes and two photon production. However, applying a coupled channel analysis on all data available to date, Lindenbaum[41] claims that "the lack of θ in LASS data is predicted ", if it is assumed a scalar; furthermore, for a glueball interpretation, the difference in the observed rate of decay to $\pi\pi$[45] and $K\overline{K}$ needs to be explained. Similarly,

its interpretation as the first radial excitation of the mainly $s\bar{s}$ scalar also has difficulty, since the mass is too low compared to its ground state partner, presumed to be the $f_0(1525)$. The other possible interpretations are as a $q\bar{q}g$ or $qq\bar{q}\bar{q}$ state, as discussed in chapter 1 of this thesis. Recently, Tornqvist[58] has suggested that certain non-$q\bar{q}$ candidate states, including the spin zero θ, might be deuteron-like meson-meson bound states. A deeper understanding of the $f_0(1710)$ requires detailed study in other contexts, such as central production and hadronic J/ψ decay with recoil of the approximately ideally-mixed $\phi(s\bar{s})$ or $\omega(u\bar{u}+d\bar{d})$; the latter are believed to be good channels for probing the coupling of resonances to the $(s\bar{s})$ and $(u\bar{u}+d\bar{d})$ quark configurations.

The $f_0(1400)$ is confirmed in the study of the $J/\psi \to \gamma\pi^+\pi^-$ data.[45] It is most likely the mainly $u\bar{u}+d\bar{d}$ ground state scalar meson. It is close in mass to its tensor and pseudovector partners, which supports the naive speculation that the mass splitting among the P-wave triplet states is small. The ratio of the branching fractions of this state to $K\overline{K}$ and $\pi\pi$ is measured to be 0.2 ± 0.6; although this results is imprecise, it is consistent with the world average of 0.8 ± 0.1, calculated on the basis of the branching fractions quoted in ref 2.

There are speculations[59] that the $G_0(1590)$ is not real, but rather its appearance in the $\eta\eta$ and $\eta\eta'$ data is due to the $f_0(1400)$ and $f_0(1710)$. Since the quark content of $\eta\eta$ and $\eta\eta'$ is different from those of $\pi\pi$ and $K\overline{K}$, the branching fractions of these states to $\eta\eta$ and $\eta\eta'$ may lead to a different shape of the overall mass distribution due to the two near-by resonances in these channels, than those in the $\pi\pi$ and $K\overline{K}$ channels. A careful study of the $\eta\eta$ and $\eta\eta'$ channels in J/ψ radiative decay needs a future J/ψ experiment with a neutral trigger

so that the $J/\psi \rightarrow \gamma\eta\eta$ or $\gamma\eta\eta'$ events can be tagged through their high-rate all-neutral decay modes.

Discussion of the Spin 2 Resonances

This study, and a similar one for the $J/\psi \rightarrow \gamma\pi^+\pi^-$ data,[45] confirm the well established ground-state tensor mesons, the $f_2(1270)$ and $f_2'(1525)$. These results, provide a check of the analysis procedure, beyond those made with Monte Carlo samples (cf. Chapter 4), since the spins of these states are well determined from fixed target experiments with high statistics. Furthermore, these new results refine those previously obtained on the ratios of the helicity amplitudes resulting from J/ψ radiative decay through these resonances. The present study separates the contributions from states with different spins and helicities, rather than taking all the events in a selected mass region as pure spin 2 events as was done in the previous analysis.[38]

The ratios of the helicity amplitudes of the $f_2'(1525)$ from the present analysis are consistent with the previous MARK III measurements ,[38] so that the explanation of their values offered by Close and Li[60,61] is still valid. However, it should be noted that the present results are also consistent with the predictions of Krammer.[62] These ratios provide useful information for testing models of the resonance production and decay mechanisms. The ratios obtained for the $\theta(1720)$ by the previous analysis under the assumption of pure spin 2 appeared drastically different from those of the $q\bar{q}$ tensor mesons. This was taken as evidence in support of the tensor glueball interpretation of the $\theta(1720)$.[63] The present analysis has shown that the $\theta(1720)$ region is dominated by a spin

0 intermediate state, so that the "peculiar" spin 2 helicity amplitude structure in the previous analysis resulted from the incorrect assumption that the events in this region are from a pure spin 2 intermediate state.

The present study, with its limited statistics, cannot exclude the possible contribution of a small spin 2 component in the $\theta(1720)$ region, and cannot determine whether the spin 2 events are due to the tail of the $f_2'(1525)$ or to some new spin 2 activity in the $\theta(1720)$ mass region. It should be noted that the results of the higher statistics $J/\psi \rightarrow \gamma\pi^+\pi^-$ data show no events in the spin 2 amplitudes in this mass region.[45] It is clear that in order to better understand the amplitude structure, the present experiment should be repeated at a much higher (eg. 10 times) statistical level. Such statistics may become available at the Beijing Electron Positron Collider (BEPC) within the next five years, or subsequently at a Tau-Charm Factory, if such a facility is ever constructed.

CHAPTER VII

CONCLUSION

Using the 5.8×10^6 J/ψ events collected by the MARK III experiment on the SPEAR e^+e^- storage ring at SLAC, a mass independent amplitude analysis of the $J/\psi \rightarrow \gamma\, K_s K_s$ and $J/\psi \rightarrow \gamma\, K^+K^-$ decays is presented. For $K\overline{K}$ systems having mass less than 2 GeV/c^2, the efficiency-corrected spherical harmonic moments of the J/ψ joint decay angular distribution are measured. Fits are then performed in each independent mass interval in order to extract the underlying helicity amplitude structure; amplitudes describing $K\overline{K}$ systems of spin zero and spin two are included simultaneously.

For the first time, a large spin zero component in the $\theta(1720)$ mass region is observed; consistent results are obtained for the data samples corresponding to the individual decay modes. This structure is attributed to the production of an S wave resonance, the $f_0(1710)$, of mass and width $M = 1710 \pm 20\ MeV/c^2$, $\Gamma = 186 \pm 30\ MeV/c^2$, respectively, with branching fraction $Bf(J/\psi \rightarrow \gamma f_0, f_0 \rightarrow K\overline{K}) = (6.47 \pm 1.14 \pm 0.84) \times 10^{-4}$. A small amount ($\sim$ 24%) of spin two component in this mass region cannot be ruled out with the present statistics. These results revise the previous conclusion[38] that the $\theta(1720)$ is a spin two resonance, a result obtained on the basis of spin hypothesis tests, which assumed that either pure spin zero or pure spin two states contribute in this mass region, but not both.

The $f_0(1400)$ is observed in a similar analysis of the $J/\psi \to \gamma\pi^+\pi^-$ data,[45] and, consequently, although its contribution is small, it is included in the resonance fits in the present analysis. The possible connection of this state and the $f_0(1710)$ to the $f_0/G(1590)$ is not clear.

The previous measurements[38] of the $f_2'(1525)$ have been refined in the present analysis because of the simultaneous inclusion of spin zero and spin two amplitudes in the fit. The ratios of the helicity amplitude intensities for this state are found to be $\frac{|a_{21}|^2}{|a_{20}|^2} = 1.08 \pm 0.31$ and $\frac{|a_{22}|^2}{|a_{20}|^2} = 0.25 \pm 0.24$, and are consistent with the interpretation of the $f_2'(1525)$ as a $q\bar{q}$ meson.

APPENDIX: FORMALISM OF THE ANALYSIS

In this Appendix, the formalism of the analysis is described. In particular, the relationship between the spherical harmonic moments of the efficiency-corrected event angular distribution and the helicity amplitudes describing the decay process is developed. The former quantities are experimentally measurable, while the latter are to be determined. The dependence of the various helicity amplitudes on the mass of the intermediate state reveals the possible resonance structures of different spins of the intermediate state. With the helicity amplitudes determined, the mass, width and branching fraction of a resonance observed can be measured, which, along with the spin and the ratios of the different helicity amplitudes for this particular state, then provide information relevant to an understanding of the nature of this state, and of its production and decay mechanism.

In the following section, the helicity formalism, which describes the reaction density matrix in terms of the helicity amplitudes, is introduced in the context of a two-body decay process. This formalism is then extended to encompass sequential two-body decay processes of the type under study in the present analysis. The joint decay angular distribution for the sequential two-body decays is then expanded in terms of the spherical harmonics of the production and decay angles of the intermediate state. The explicit relationship between the moments of the spherical harmonics and the helicity amplitudes is derived. The variation of the event detection efficiency is then introduced, and the measured values

of the moments are defined in terms of the observed events; the procedures employed to obtain the efficiency-corrected moments are also discussed, as is the method used to extract the helicity amplitudes from these moments. The fits used to obtain the Breit-Wigner resonance parameters of interest are then described in the last section.

Helicity formalism for the two-body decay process: $\alpha \rightarrow 1+2$

This section gives a brief introduction to the helicity formalism and its application to a two-body decay process. For a general discussion of this formalism, the reader is referred to references 64 and 65.

The helicity, λ , of a system is defined as the projection of its spin, $\vec{S}$, along the direction of its motion, $\frac{\vec{P}}{|\vec{P}|}$. The quantity defined, $\lambda = \vec{S} \cdot \frac{\vec{P}}{|\vec{P}|}$, is invariant under a boost along $\frac{\vec{P}}{|\vec{P}|}$ or an ordinary rotation. As a consequence, eigenstates can be constructed in terms of linear momentum and the helicity, or of spin and the helicity.

Consider a decay process, $\alpha \rightarrow 1+2$, where α has spin J and spin projection M along a pre-defined Z-axis; in the rest frame of α, the state vector is denoted by $|JM\rangle$. The final state can be described as a two particle plane wave helicity state: $\left|\vec{P}_1 = \vec{P}, \lambda_1; \vec{P}_2 = -\vec{P}, \lambda_2\right\rangle$, where $\vec{P}$ is the momentum vector of one of the particles in the final state. The decay amplitude is then the matrix element,

$$\mathbf{M} = \left\langle \vec{P}_1 = \vec{P}, \lambda_1; \vec{P}_2 = -\vec{P}, \lambda_2 \right| U \left| JM \right\rangle , \qquad (1)$$

where U is the time evolution operator that propagates the initial state through the interaction. Because particles 1 and 2 have equal and opposite momenta

in this reference frame, the momentum vectors can be characterized by the magnitude, P, of the momentum and the decay axis $\vec{n}(\theta,\phi)$ defined along one of the decay particles. Expression (1) can then be re-written as

$$\mathbf{M} = \langle P,\theta,\phi,\lambda_1,\lambda_2 | U | JM \rangle ; \tag{2}$$

θ is the angle between the decay direction and the Z-axis (the spin quantization axis of α), and ϕ is the corresponding azimuthal angle defined with respect to the X and Y axes which complete the definition of the rest frame of α. In the particular case of the present analysis with $\alpha \equiv J/\psi$, this reference frame is the Lab frame with Z axis along the direction of the incident positron and Y axis pointing up out of the plane of the storage ring; the X axis completes the right-handed coordinate system.

As the helicity of the system is rotationally invariant, a set of two-particle basis vectors, $|\mathrm{j},\mathrm{m},\lambda_1,\lambda_2\rangle$, can be defined; these have definite total angular momentum j, angular momentum projection m and helicities λ_1,λ_2. Inserting a complete set of these states into eq. (2), and invoking angular momentum conservation, eq. (2) becomes

$$\begin{aligned}
\mathbf{M} &= \sum_{jm\lambda_1'\lambda_2'} \left\langle \theta,\phi,\lambda_1,\lambda_2 | \mathrm{jm},\lambda_1',\lambda_2' \right\rangle \left\langle \mathrm{jm},\lambda_1',\lambda_2' \middle| U | JM \right\rangle \\
&= \sum_{\lambda_1'\lambda_2'} \left\langle \theta,\phi,\lambda_1,\lambda_2 | \mathrm{jm},\lambda_1',\lambda_2' \right\rangle \left\langle \mathrm{jm},\lambda_1',\lambda_2' \middle| U | JM \right\rangle \delta_{jJ}\delta_{mM} \\
&= \sum_{\lambda_1'\lambda_2'} \left\langle \theta,\phi,\lambda_1,\lambda_2 | \mathrm{JM},\lambda_1',\lambda_2' \right\rangle \left\langle \mathrm{JM},\lambda_1',\lambda_2' \middle| U | JM \right\rangle \\
&= \sum_{\lambda_1'\lambda_2'} \left\langle \theta,\phi,\lambda_1,\lambda_2 | \mathrm{JM},\lambda_1',\lambda_2' \right\rangle A^J_{\lambda_1',\lambda_2'},
\end{aligned} \tag{3}$$

where $A^J_{\lambda_1',\lambda_2'} = \left\langle \mathrm{JM}, \lambda_1', \lambda_2' \middle| U \middle| JM \right\rangle$ is called the helicity amplitude, which describes the coupling of a particle with spin J to a final state of two particles with helicities λ_1', λ_2'; $A^J_{\lambda_1',\lambda_2'}$ is M independent due to the rotational invariance of the interaction. For a process where parity conservation is valid, ref 64 gives

$$A^J_{-\lambda_1,-\lambda_2} = \eta_\alpha \eta_1 \eta_2 (-1)^{J-J_1-J_2} A^J_{\lambda_1,\lambda_2}, \tag{4}$$

where $\eta_\alpha, \eta_1, \eta_2$ and J, J_1, J_2 are the intrinsic parities and the spins of the particles involved.

It can be shown that[65]

$$\left\langle \theta, \phi, \lambda_1, \lambda_2 | \mathrm{JM}, \lambda_1', \lambda_2' \right\rangle = \delta_{\lambda_1,\lambda_1'} \delta_{\lambda_2,\lambda_2'} \sqrt{\frac{2\mathrm{J}+1}{4\pi}} \mathbf{D}^{J*}_{M,\lambda_1-\lambda_2}(\phi, \theta, 0), \tag{5}$$

where $\mathbf{D}^*$ is the complex conjugate of the rotational matrix $\mathbf{D}$, the right most argument of the $\mathbf{D}$ function is chosen to be zero, which defines the phase conversion. It follows from eq. (3) that

$$\mathbf{M} = A^J_{\lambda_1,\lambda_2} \sqrt{\frac{2\mathrm{J}+1}{4\pi}} \mathbf{D}^{J*}_{M,\lambda_1-\lambda_2}(\phi, \theta, 0). \tag{6}$$

This expression then describes the decay of a particle α at rest with spin J and spin projection M along the Z axis, to the state composed of particles 1 and 2 with helicities λ_1 and λ_2, and particle 1 is emitted in the direction $\vec{n}(\theta, \phi)$.

Helicity formalism for the sequential two-body decays,

$J/\psi \rightarrow \gamma X, X \rightarrow$ pseudoscalar pair

The matrix element describing sequential two-body decays is the product of the matrix elements of the two-body decay processes. For the case $J/\psi \rightarrow \gamma X, X \rightarrow p\bar{p}$, where p denotes a pseudoscalar particle, the resulting matrix element is given by

$$\mathbf{M} = A^{J_\psi}_{\lambda_X,\lambda_\gamma} \sqrt{\frac{2\mathrm{J}_\psi + 1}{4\pi}} \mathbf{D}^{J_{\psi}*}_{\lambda_\psi,\lambda_X-\lambda_\gamma}(\Omega_X) A^{J_X}_{\lambda_p,\lambda_{\bar{p}}} \sqrt{\frac{2\mathrm{J_X} + 1}{4\pi}} \mathbf{D}^{J_X*}_{\lambda_X,\lambda_p-\lambda_{\bar{p}}}(\Omega^*_p), \quad (7)$$

where Ω_X denotes the arguments $(\phi, \theta, 0)$, where θ_X and ϕ_X are the polar and azimuthal angles of X in the J/ψ rest frame, and Ω^*_p denotes $(\phi^*_p, \theta^*_p, 0)$, where θ^*_p and ϕ^*_p are the corresponding angles of p in the X rest frame. The J/ψ rest frame is the Lab frame, as described previously. The rest frame of the system X is defined such that the Z axis, Z', is along the direction of motion of X in the Lab frame, and the Y' axis is along $\vec{Z} \times \vec{Z}'$; X' completes the right-handed coordinate system.

The vector coupling[3] of the initial state electron and positron to the J/ψ ensures that production of the J/ψ with helicity 0 is virtually zero, i.e., the J/ψ is produced only with helicity ± 1. Furthermore, in J/ψ radiative decay to a pair of pseudoscalar particles, charge conjugation invariance ensures that only those intermediate states for which $J^{PC} = (\text{even})^{++}$ are allowed (see Chapter 1). Since the present analysis covers only the intermediate states with mass less than 2 GeV/c^2, $J = 0, 2$ are considered to be the only candidate intermediate spins. Objects with spin as high as 4 are unlikely to exist in this mass region. It

follows that the possible quantum numbers describing the initial, intermediate and final states are:

$J_\psi = 1, \quad \lambda_\psi = \pm 1$: spin and helicity of J/ψ

$J_X = 0, 2, \quad \lambda_X = 0, \pm 1, \pm 2$: spin and helicity of X

$J_\gamma = 1, \quad \lambda_\gamma = \pm 1$: spin and helicity of γ

$J_p = 0, \quad \lambda_p = 0$: spin and helicity of p

in addition, $|\lambda_X - \lambda_\gamma| \leq 1$, since the spin projection of the (X, γ) system in any direction cannot exceed the spin of the J/ψ.

Rewriting eq. (7) with J_ψ and λ_p replaced by their unique numerical values, the matrix element becomes

$$\mathbf{M} = A^1_{\lambda_X, \lambda_\gamma} \sqrt{\frac{3}{4\pi}} \mathbf{D}^{1*}_{\lambda_\psi, \lambda_X - \lambda_\gamma}(\Omega_X) A^{J_X}_{0,0} \sqrt{\frac{2\mathrm{J_X} + 1}{4\pi}} \mathbf{D}^{J_X *}_{\lambda_X, 0}(\Omega^*_p). \tag{8}$$

The joint decay angular distribution for the sequential two-body decays, $J/\psi \to \gamma X, X \to$ pseudoscalar pair

The Fermi Golden Rule states that:

$$dN = |M|^2 \, dLIPS, \tag{9}$$

where dN is the number of transitions occurring to the Lorentz invariant phase space volume element, $dLIPS$, for the process described by the matrix element,

M. For the present analysis,

$$dLIPS \propto \frac{P}{m_\psi}\frac{Q}{m} dm^2 \; d\Omega_X \; d\Omega_p^*, \tag{10}$$

where P is the magnitude of the 3-momentum of X in the Lab frame, Q is the magnitude of the 3-momentum of one of the pseudoscalars in the X rest frame, and m is the mass of the $p\bar{p}$ pair; $d\Omega = d\cos\theta d\phi$, with θ_X, ϕ_X specify the direction of X in the Lab frame, and θ_p^*, ϕ_p^* the direction of p in the $p\bar{p}$ rest frame.

Ignoring m_ψ, which is a constant, eq. (10) can be re-written as

$$dLIPS \propto PQ \; dm \; d\Omega_X \; d\Omega_p^*. \tag{11}$$

In the present analysis, the factor PQ is subsumed into $|M|^2$, so that the transition rate is specified by

$$dN = |M|^2 \; dm \; d\Omega_X \; d\Omega_p^*; \tag{12}$$

$|M|^2$ must be summed over final, and averaged over initial spin states. The resulting differential cross section then takes the form

$$4\pi \frac{dN}{dm \; d\Omega_X \; d\Omega_p^*} = \frac{3}{4} \sum_{\lambda_\psi, \lambda_\gamma} \left| \sum_{J_X, \lambda_X} a^{\lambda_\gamma}_{J_X, \lambda_X} \sqrt{\frac{2J_X + 1}{4\pi}} \mathbf{D}^{1*}_{\lambda_\psi, \lambda_X - \lambda_\gamma}(\Omega_X) \mathbf{D}^{J_X *}_{\lambda_X, 0}(\Omega_p^*) \right|^2, \tag{13}$$

with

$$a^{\lambda_\gamma}_{J_X, \lambda_X} = A^1_{\lambda_X, \lambda_\gamma} A^{J_X}_{0,0} \sqrt{PQ} \; . \tag{14}$$

Parity conservation (eq. (4) above) then implies

$$a^{-\lambda_\gamma}_{J_X,-\lambda_X} = a^{\lambda_\gamma}_{J_X,\lambda_X} \tag{15}$$

for the particular case of J/ψ radiative decay to two pseudoscalars.

Helicity amplitudes and moments

In general, the joint angular distribution of the sequential two-body decays can be expanded in terms of the products of the spherical harmonics of the production and decay angles of the intermediate states,

$$4\pi \frac{dN}{dm\ d\Omega_X\ d\Omega_p^*} = \sum_{j,l,m,n} \mathbf{T}^j_{l,m,n} \mathbf{Y}_{j,m}(\Omega_X) \mathbf{Y}_{l,n}(\Omega_p^*),$$

where j, l are natural numbers, 0, 1, 2, ..., $|m| \leq j$ and $|n| \leq l$; it is clear that the orthogonality of the spherical harmonic functions implies that the coefficients, $\mathbf{T}^j_{l,m,n}$, which are functions of the mass of the intermediate state, can be obtained from the data by evaluating

$$\int_{\Omega_X,\Omega_p^*} \mathbf{Y}^*_{j,m}(\Omega_X) \mathbf{Y}^*_{l,n}(\Omega_p^*) \frac{4\pi dN}{dm\ d\Omega_X\ d\Omega_p^*} d\Omega_X d\Omega_p^*$$
$$= \sum_{i=1}^{All\ Events} 4\pi \mathbf{Y}^*_{j,m}(\Omega_X^i) \mathbf{Y}^*_{l,m}(\Omega_p^{*i});$$

for this reason, the $\mathbf{T}^j_{l,m,n}$, are referred to as the moments of the joint decay angular distribution.

In order to find out the relations between the underlying helicity amplitudes and the spherical harmonic moments measured in experiment, the summations in eq. (13) are carried out and expression (13) is written as

$$4\pi \frac{dN}{dm\ d\Omega_X\ d\Omega_p^*} = \sum_{\mathrm{j,l,m,n}} \mathbf{T}^{\mathrm{j}}_{\mathrm{l,m,n}} \mathbf{Y}_{\mathrm{j,m}}(\theta_X, \phi_X = 0) \mathbf{Y}^*_{\mathrm{l,n}}(\Omega_p^*), \tag{16}$$

with

$$\begin{aligned} \mathbf{T}^{\mathrm{j}}_{\mathrm{l,m,n}} =& (-1)^{\mathrm{m}} \frac{3}{4} \sum_{\lambda_\psi, \lambda_\gamma} \sum_{J_X, \lambda_X} \sum_{J'_X, \lambda'_X} a^{\lambda_\gamma}_{J_X, \lambda_X} a^{\lambda_\gamma *}_{J'_X, \lambda'_X} \sqrt{\frac{2\mathrm{J_X}+1}{2\mathrm{j}+1}} \sqrt{\frac{2\mathrm{J'_X}+1}{2\mathrm{l}+1}} \\ & \times \left\langle 1, -\lambda_\psi; 1, \lambda_\psi | \mathrm{j}, 0 \right\rangle \left\langle 1, -\lambda_X + \lambda_\gamma; 1, \lambda'_X - \lambda_\gamma | \mathrm{j}, \mathrm{m} \right\rangle \\ & \times \left\langle J_X, -\lambda_X; J'_X, \lambda'_X | \mathrm{l}, \mathrm{n} \right\rangle \left\langle J_X, 0; J'_X, 0 | \mathrm{l}, 0 \right\rangle, \end{aligned} \tag{17}$$

where $\mathrm{j, l, m, n}$ correspond to those allowed values for which the product of the Clebsch-Gordan coefficients in eq. (17) is non-zero; in particular, $\mathrm{m} = \mathrm{n} = \lambda'_X - \lambda_X$, and $|\mathrm{m}| \leq 2$; the index n is thus suppressed and

$$\mathbf{T}^{\mathrm{j}}_{\mathrm{l,m}} \equiv \mathbf{T}^{\mathrm{j}}_{\mathrm{l,m,n}}$$

is used in what follows. It should be noted that parity conservation (eq. (15)) implies

$$\mathbf{T}^{\mathrm{j}}_{\mathrm{l,-m}} = \mathbf{T}^{\mathrm{j}}_{\mathrm{l,m}}. \tag{18}$$

In eq. (13), each term within the modulus sign contains the factor $e^{i\lambda_\psi \phi_X}$ from the first $\mathbf{D}$ matrix, and this is the only dependence of the expression on ϕ_X; it

follows that the right-hand side of eq. (13) is independent of ϕ_X, as must be the case for unpolarized electron and positron beams. A direct consequence of this is that, in eq. (16), $\mathbf{Y}_{\mathrm{j,m}}$ is to be evaluated at $\phi_X = 0$.

In deriving eq. (16) and (17), the following general relations have been utilized:

$$\mathbf{D}^{J*}_{M',M}(\Omega) = (-1)^{M'-M}\mathbf{D}^{J}_{-M',-M}(\Omega);$$

$$\mathbf{D}^{J_1}_{M_1',M_1}(\Omega)\mathbf{D}^{J_2}_{M_2',M_2}(\Omega) = \sum_{|J_1-J_2|\le J_3\le J_1+J_2} \left\langle J_1, M_1', J_2, M'2 | J_3, M_1' + M_2' \right\rangle \times \langle J_1, M_1, J_2, M_2 | J_3, M_1 + M_2 \rangle \, \mathbf{D}^{J_3}_{M_1'+M_2',M_1+M_2}(\Omega);$$

$$\mathbf{D}^{J}_{M',M}(\phi,\theta,0) = e^{-iM'\phi} d^{J}_{M',M}(\theta);$$

$$d^{J}_{M',M}(\theta) = d^{J}_{-M,-M'}(\theta);$$

$$\mathbf{D}^{J}_{M,0}(\phi,\theta,0) = \sqrt{\frac{4\pi}{2\mathrm{J}+1}}\mathbf{Y}^{*}_{J,M}(\theta,\phi);$$

$$\mathbf{Y}^{*}_{J,M}(\theta,\phi) = (-1)^{M}\mathbf{Y}_{J,-M}(\theta,\phi).$$

The explicit expressions for the complete set of moments in terms of the

amplitudes are obtained from eq. (17) as follows:

$$
\begin{aligned}
\mathbf{T}^0_{0,0} &= |a_{0,0}|^2 + |a_{2,0}|^2 + |a_{2,1}|^2 + |a_{2,2}|^2 \\
\mathbf{T}^2_{0,0} &= \frac{\sqrt{5}}{10}[|a_{0,0}|^2 + |a_{2,0}|^2 - 2|a_{2,1}|^2 + |a_{2,2}|^2] \\
\mathbf{T}^0_{2,0} &= \frac{\sqrt{5}}{5}[2\sqrt{5}Re(a_{0,0}a^*_{2,0}) + \frac{5}{7}(2|a_{2,0}|^2 + |a_{2,1}|^2 - 2|a_{2,2}|^2)] \\
\mathbf{T}^2_{2,0} &= \frac{1}{5}[\sqrt{5}Re(a_{0,0}a^*_{2,0}) + \frac{5}{7}(|a_{2,0}|^2 - |a_{2,1}|^2 - |a_{2,2}|^2)] \\
\mathbf{T}^2_{2,1} &= -\frac{\sqrt{3}}{10}[\sqrt{5}Re(a_{0,0}a^*_{2,1}) + \frac{5}{7}(Re(a_{2,0}a^*_{2,1}) - \sqrt{6}Re(a_{2,1}a^*_{2,2}))] \\
\mathbf{T}^2_{2,2} &= \frac{\sqrt{6}}{10}[\sqrt{5}Re(a_{0,0}a^*_{2,2}) - \frac{10}{7}(Re(a_{2,0}a^*_{2,2})] \\
\mathbf{T}^0_{4,0} &= \frac{1}{7}[6|a_{2,0}|^2 - 4|a_{2,1}|^2 + |a_{2,2}|^2] \\
\mathbf{T}^2_{4,0} &= \frac{\sqrt{5}}{70}[6|a_{2,0}|^2 + 8|a_{2,1}|^2 + |a_{2,2}|^2] \\
\mathbf{T}^2_{4,1} &= -\frac{\sqrt{3}}{14}[\sqrt{6}Re(a_{2,0}a^*_{2,1}) + Re(a_{2,1}a^*_{2,2})] \\
\mathbf{T}^2_{4,2} &= \frac{3\sqrt{2}}{14}Re(a_{2,0}a^*_{2,2}).
\end{aligned}
\tag{19}
$$

There are 10 moments in total. In eq. (19), λ_X takes values greater than or equal to 0, and λ_γ is suppressed from $a^{\lambda_\gamma}_{J_X,\lambda_X}$ as a consequence of the parity conservation relation (eq. (15)). The amplitudes to be determined in this analysis are: $a_{0,0}$, the amplitude with $J_X = 0, \lambda_X = 0$, and $a_{2,0}, a_{2,1}, a_{2,2}$, the amplitudes with $J_X = 2, \lambda_X = 0, \pm 1, \pm 2$. Since the moments are the quantities measured in the experiment and the amplitudes are the ones to be determined, the relations expressed in eq. (19) are essential to the present analysis, and are referred to frequently in the main text of the thesis.

Moment measurement and efficiency correction

Making use of the relation (18), eq. (16) may be re-written as

$$4\pi \frac{dN}{dm\ d\Omega_X\ d\Omega_p^*} = \sum_{\mathrm{j,l,(m\geq 0)}} (2-\delta_{\mathrm{m0}})\, \mathbf{T}^{\mathrm{j}}_{\mathrm{l,m}} Re\left(\mathbf{Y}_{\mathrm{j,m}}(\theta_X)\mathbf{Y}^*_{\mathrm{l,m}}(\Omega_p^*)\right), \qquad (20)$$

where the argument of $\mathbf{Y}_{\mathrm{j,m}}$ is denoted simply by θ_X to indicate that the function is to be evaluated with $\phi_X = 0$.

The analysis is carried out on a mass bin by mass bin basis; that is, the data sample for each decay mode is divided into sub-samples according to $p\overline{p}$ invariant mass, and the moments and helicity amplitudes of each sub-sample are determined. Mass intervals of $\Delta m = 100\ MeV/c^2$ are used for each individual decay mode, while $\Delta m = 50\ MeV/c^2$ is used for the combined $J/\psi \rightarrow \gamma K^+K^-$ and $J/\psi \rightarrow \gamma K^0\overline{K}^0$ data.

The detection efficiency is, in general, a function of all the kinematical quantities, and thus is denoted by $A(\Omega_X, \Omega_p^*, m)$; it is the probability that an event produced with the mass of the intermediate state,m, and decay angles, Ω_X and Ω_p^*, will be detected, reconstructed, and will survive the event selection criteria (consequently, $0 \leq A \leq 1$). Multiplying by $Re\left(\mathbf{Y}^*_{\mathrm{j',m'}}(\theta_X)\mathbf{Y}_{\mathrm{l',m'}}(\Omega_p^*)\right)$ and $A(\Omega_X, \Omega_p^*, m)$ on both sides, and integrating over the whole $(\Omega_X, \Omega_p^*, \Delta m)$ do-

main, expression (20) becomes:

$$\int\limits_{\Omega_X,\Omega_p^*,\Delta m} Re\left(\mathbf{Y}^*_{j',m'}(\theta_X)\mathbf{Y}_{l',m'}(\Omega_p^*)\right) A(\Omega_X,\Omega_p^*,m)\frac{4\pi dN}{d\Omega_X\, d\Omega_p^*\, dm} d\Omega_X d\Omega_p^* dm$$

$$= \sum_{j,l,(m\geq 0)} \int\limits_{\Omega_X,\Omega_p^*,\Delta m} Re\left(\mathbf{Y}^*_{j',m'}(\theta_X)\mathbf{Y}_{l',m'}(\Omega_p^*)\right) A(\Omega_X,\Omega_p^*,m)$$

$$\times (2-\delta_{m0})\,\mathbf{T}^j_{l,m} Re\left(\mathbf{Y}_{j,m}(\theta_X)\mathbf{Y}^*_{l,m}(\Omega_p^*)\right) d\Omega_X d\Omega_p^* dm. \tag{21}$$

The integration on the left hand side of eq. (21) can be approximated by a summation over the observed real events as follows,

$$\mathbf{N}^{j'}_{l',m'} \equiv 4\pi \sum_{i=1}^{N_{observed}} Re(\mathbf{Y}^*_{j',m'}(\theta_X^i)\mathbf{Y}_{l',m'}(\Omega_p^{*i})); \tag{22}$$

The approximation would become exact if $N_{observed}$ were infinitely large, since the observed real events are distributed according to $A(\Omega_X,\Omega_p^*,m)\frac{dN}{d\Omega_X\, d\Omega_p^*\, dm}$. The notation, $N^j_{l,m}$, employed here denotes the value of the moment $T^j_{l,m}$ obtained from the data sample; it is therefore subject to efficiency loss effects, and may differ markedly from the underlying true value, $T^j_{l,m}$ (cf. Fig. 32). The normalization in eq. (22) is such that $\mathbf{N}^0_{0,0}$ is equal to the number of observed events.

To simplify the notation,

$$\begin{aligned} \mathbf{N}_\mu &= \mathbf{N}^{j'}_{l',m'} \\ \mathbf{T}_\nu &= \mathbf{T}^j_{l,m} \end{aligned} \tag{23}$$

are used in what follows, where μ and ν denote the combinations of indices (j',l',m') and (j,l,m), respectively. Expression (21) then may be written as

$$\mathbf{N}_\mu = \sum_{\nu=1}^{10} C_{\mu,\nu}\mathbf{T}_\nu, \tag{24}$$

with

$$\begin{aligned}\mathbf{C}_{\mu,\nu} = \int_{\Omega_X,\Omega_p^*} & Re\left(\mathbf{Y}^*(\theta_X)\mathbf{Y}(\Omega_p^*)\right)_\mu A(\Omega_X,\Omega_p^*,m)(2-\delta_{\mathrm{m}0}) \\ & \times Re\left(\mathbf{Y}(\theta_X)\mathbf{Y}^*(\Omega_p^*)\right)_\nu d\Omega_X d\Omega_p^* dm.\end{aligned} \tag{25}$$

Equation (22) defines the procedure which is followed in obtaining the measured moments; the efficiency-corrected moments, $\mathbf{T}_\nu$, are then obtained from eq. (24) by matrix inversion. The right hand side of eq. (25) is obtained, to a very good approximation, from the summation

$$\mathbf{C}_{\mu,\nu} = \frac{16\pi^2}{N_{generated}} \sum_{i=1}^{N_{accepted}} Re\left(\mathbf{Y}^*(\theta_X^i)\mathbf{Y}(\Omega_p^{*i})\right)_\mu (2-\delta_{\mathrm{m}0})\, Re\left(\mathbf{Y}(\theta_X^i)\mathbf{Y}^*(\Omega_p^{*i})\right)_\nu \tag{26}$$

over a set of accepted Monte Carlo events, The Monte Carlo events are generated uniformly over the mass region of the sub-sample, and in (Ω_X, Ω_p^*). In eq. (26), $N_{generated}$ is the number of Monte Carlo events generated, and $N_{accepted}$ is the number which survive detector simulation and the event selection criteria applied to real data events. The factor $\frac{16\pi^2}{N_{generated}}$ gives a normalization such that $\mathbf{T}^0_{0,0}$, which is the sum of the squares of all the helicity amplitudes (eq. (19)), is the estimate of the true number of events after efficiency correction. With this normalization, the intensity of each amplitude is then equal to the number of events contributed by the intermediate state with the particular spin and helicity.

In the efficiency correction process, the Monte Carlo samples are defined such that the value of $N_{accepted}$ for each sub-sample is at least ten times larger than the corresponding number of observed real events; it follows that the contributions due to statistical fluctuations in the Monte Carlo sample to the uncertainties in the efficiency-corrected amplitudes are negligible in comparison to the statistical uncertainties of the real data.

The covariance matrix associated with the measured moments, $\mathbf{N}_\mu$, is estimated as

$$\mathbf{O}_{\mu,\nu} = 16\pi^2 \sum_{i=1}^{N_{observed}} Re\left(\mathbf{Y}^*(\theta_X^i)\mathbf{Y}(\Omega_p^{*i})\right)_\mu Re\left(\mathbf{Y}^*(\theta_X^i)\mathbf{Y}(\Omega_p^{*i})\right)_\nu ; \qquad (27)$$

this takes account of statistical uncertainties only. Contributions due to angular resolution are negligible by comparison.

Extraction of the helicity amplitudes from the moments

From eq. (24),

$$\mathbf{T}_\mu = \sum_{\nu=1}^{10} \mathbf{C}^{-1}_{\mu,\nu}\mathbf{N}_\nu, \qquad (28)$$

where $\mathbf{C}^{-1}$ is the inverse matrix of $\mathbf{C}$ as defined by eq. (26). The covariance matrix of the efficiency-corrected moments is then

$$\mathbf{V} = \mathbf{C^{-1}O}(\mathbf{C^{-1}})^+ \qquad (29)$$

with $\mathbf{O}$ given by eq. (27) and $\mathbf{C}$ by eq. (26). In cases where data samples corresponding to different decay modes (e.g. the K^+K^- and $K^0\overline{K}^0$ modes in

this study) or data samples from different experiments can be combined, the efficiency-corrected moments, and their covariance matrix, are the quantities to be combined. On the other hand, if incoherent contributions due to background events are large and have to be subtracted before the amplitude analysis, the efficiency-corrected moments and their covariance matrix of the background events should be simulated and taken into account prior to the amplitude extraction.

To obtain the amplitudes which fit the efficiency-corrected moments, a χ^2 function given by

$$\chi^2 = \sum_{\mu,\nu=1}^{10} \left(\sum_{\sigma=1}^{10} \mathbf{C}_{\mu\sigma}^{-1} \mathbf{N}_\sigma - \mathbf{T}_\mu(a) \right) \mathbf{V}^{-1} \left(\sum_{\sigma=1}^{10} \mathbf{C}_{\nu\sigma}^{-1} \mathbf{N}_\sigma - \mathbf{T}_\nu(a) \right) \qquad (30)$$

is minimized mass bin by mass bin. In eq. (30) , $\mu, \nu, \sigma = 1, 2...10$ stand for the indices (j, l, m) of the 10 moments; $\mathbf{T}_\mu(a)$, $\mathbf{T}_\nu(a)$ are the expressions for the moments in terms of the helicity amplitudes, as listed in eq. (19). The minimization can be performed using a standard software package. In this analysis, it is carried out by means of the code MINUIT.[57]

Breit-Wigner fits to the amplitude intensity distributions

The intensity distribution of each helicity amplitude, a, as a function of the mass, m, of the system X may be written (cf. eq. (14))

$$|a|^2 = |B|^2 PQ, \qquad (31)$$

where B is the amplitude describing the mass dependence of the production and decay of X. In the case that X is resonant, B may be written as

$$B = B_P \frac{1}{m_0^2 - m^2 - im_0\Gamma^{tot}(m)} B_D, \tag{32}$$

where B_P describes the radiative decay of the J/ψ to X, B_D describes the decay of X to $p\bar{p}$, m_0 is the mass of the resonance, and $\Gamma^{tot}(m)$ is its mass-dependent total width. For spin 0 and 2, it is assumed that X couples to the recoil photon with the lowest allowed orbital angular momentum, namely, S-wave. Consequently, B_P is taken to be a constant. On the other hand, the mass dependence of B_D is taken to be in the form of the appropriate centrifugal barrier factor, namely Q^L, where L is the orbital angular momentum of $p\bar{p}$ system from the decay of X, i.e., 0 or 2. The total width is given by

$$\Gamma^{tot}(m) = \sum_i \Gamma^i(m), \tag{33}$$

where the summation is over all of the decay modes of X. In principle, each mode has its own characteristic mass dependence. However, for the purpose of this analysis, it is assumed that the overall mass dependence is given by that corresponding to the $K\overline{K}$ mode, and the width is given by

$$\Gamma^{tot}(m) = \Gamma_0 \left(\frac{Q}{Q_0}\right)^{2L+1} \frac{m_0}{m}, \tag{34}$$

where Q_0 represents Q evaluated at m_0, the resonance mass; Γ_0 corresponds to the resonance width which is quoted in the tables of the Review of Particle

Properties.[2] Frequently, eq. (34) is modified by including a Blatt-Weisskopf barrier factor[66] with a choice of a radius equal to 1 fermi. The lack of precision in the measured amplitudes in the present experiment does not justify such refinements, consequently this factor is not included. The amplitude, B, thus takes the form

$$B = \frac{f' Q^L}{m_0^2 - m^2 - i m_0 \Gamma^{tot}(m)}, \tag{35}$$

where f' is a constant, and Γ^{tot} is given by eq. (34). The parameters of the resonance X are extracted by fitting eq. (31) to the data, with B specified by eq. (35). If I denotes the integral of eq. (31) over the mass range of the fit, ΔM, i.e.,

$$I = \int_{\Delta M} | a |^2 \, dm, \tag{36}$$

the expression which is actually fit to each amplitude intensity distribution is

$$|a|^2 = f \, | \frac{B}{\sqrt{I}} |^2 \, PQ \, , \tag{37}$$

so that the fitted value of f directly represents the number of events in the mass interval ΔM corresponding to the production of the resonance X.

If the amplitude intensity distribution, $|a|^2$, is to be described by a coherent superposition of several resonances, eq. (37) is generalized to

$$|a|^2 = | \sum_j \frac{\sqrt{f_j} e^{i\phi_j} B_j}{\sqrt{I_j}} |^2 \, PQ, \tag{38}$$

where j runs over the resonances involved; if the phase ϕ_1 is chosen to be zero, the remaining ϕ_j represent the production phases of the other resonances relative

to the first one. The fitted value of the parameter f_j represents the intensity contribution due to the j-th resonance in the mass range ΔM.

The fits are carried out by integrating eq. (38) over each individual mass bin and setting up a χ^2 contribution which is the square of the difference between this value and the measured value divided by the measured uncertainty for the bin in question. The overall χ^2 is obtained by summing this quantity over the bins included in the fit, and the relevant parameter values are estimated by minimizing this χ^2 by means of the program MINUIT.[57]

REFERENCES

1. J. J. Aubert *et al.*, Phys. Rev. Lett **33** (1974) 1404; J. E. Augustin *et al.*, Phys. Rev. Lett **33** (1974) 1406.

2. Particle Data Group, Phys. Lett. **B 239** (1990) 1-516.

3. D. Perkins, *Introduction to High Energy Physics*, 3rd ed., (Addison-Wesley, Menlo Park, CA, 1987), p. 377-378.

4. S. Okubo, Phys. Lett. **5** (1963) 165; G. Zweig, CERN Report Theor, 401 and 412 (1964) unpublished; J. Iuzuba, Prog. Theor. Phys. Suppl. **37-38** (1966) 21; J. Iuzuba, K. Okudo and O. Shito, Prog. Theor. Phys. **35** (1966) 1061.

5. L. Kopke and N. Wermes, J/ψ *Decays*, Phys. Reports (Review Section of Phys. Lett.) **174** (1989) 67-227 and the references therein.

6. J. Weinstein and N. Isgur, Phys. Rev. **D27** (1983) 588; UTPT 89-03.

7. W. Toki, BNL Workshop on Glueball, Hybrids and Exotic Hadrons at Brookhaven National Labs, Upton, New York, August 29 - September 1, 1988; Q.-X. Shen, High Energy and Nuclear Physics Journal (in Chinese), **15** (1991) 358.

8. J. Drinkard, Ph.D thesis, University of Californin, Santa Cruz (1990), unpublished, SCIPP 90/04; Z. Bai *et al.*, Phys. Rev. Lett. **65** (1990) 2507.

9. A. Birman *et al.*, Phys. Rev. Lett. **61** (1989) 1557.

10. M. G. Rath *et al.*, Phys. Rev. **D40** (1989) 693.

11. N. R. Stanton *et al.*, Phys. Rev. Lett. **42** (1979) 346; A. Ando *et al.*, Phys. Rev. Lett. **57** (1986) 1296.

12. A. Etkin *et al.*, Phys. Rev. Lett. **49** (1982) 1620; Phys. Lett. **B165** (1985) 217; Phys. Lett. **B201** (1988) 568.

13. P. S. L. Booth *et al.*, Nucl. Phys. **B273** (1986) 677.

14. T. A. Armstrong *et al.*, Phys. Lett. **B221** (1989) 221.

15. G. Eigen, CALT-68-1595 (1989).

16. Z. Bai *et al.*, SLAC-PUB-5159 (1990).

17. D. Bisello *et al.*, Phys. Lett. **B179** (1986) 294; D. Bisello *et al.*, LAL 90-12 (1990).

18. R. Sinha *et al.*, Phys. Rev. **D35** (1987) 952.

19. K. F. Einsweiler SLAC-PUB-3202 (1983); R. M. Baltrusaitis *et al.*, Phys. Rev. Lett. **56** (1986) 107.

20. D. Alde *et al.*, Phys. Lett. **B177** (1986) 120.

21. V. F. Obraztsov, Proc. of the 23rd Int. Conf on HEP, Berkeley, July 1986.

22. D. Aston *et al.*, Nucl. Phys. **B301** (1988) 525.

23. D. Aston *et al.*, Phys. Lett. **B208** (1988) 342.

24. J. Augustin *et al.*, Phys. Rev. Lett. **60** (1988) 2238.

25. J. Sculli *et al.*, Phys. Rev. Lett. **58** (1987) 1715; G. Bardin *et al.*, Phys. Lett. **B195** (1987) 292.

26. A. Etkin *et al.*, Phys. Rev. **D25** (1982) 2446.

27. D. Alde *et al.*, Nucl. Phys. **B269** (1986) 485.

28. M. Baubillier *et al.*, Z. Phys. **C17** (1983) 309.

29. F. Binon, *et al.*, Nuovo Cimento **A78** (1983) 313.

30. S. Gershtein, *et al.*, Z. Phys. **C24** (1984) 305.

31. J.-P. Stroot, Proc. of QCD'90, Montpellier. July 1990. CERN-PPE/91-02.

32. Named as $f_2(1720)$ in Ref. 2, with a note that spin needs confirmation.

33. A. Etkin, *et al.*, Phys. Rev. **D25** (1982) 1786.

34. E. Williams, *et al.*, Phys. Rev. **D30** (1984) 877.

35. D. Alde, *et al.*, Phys. Lett. **B182** (1986) 105.

36. B. Bolonkin, *et al.*, Nucl. Phys. **B309** (1988) 426.

37. C. Edwards *et al.*, Phys. Rev. Lett. **48** (1982) 458.

38. R. M. Baltrusaitis *et al.*, Phys. Rev. **D35** (1987) 2077.

39. T. A. Bolton, Ph.D thesis, Massachusetts Institute of Technology (1988), unpublished.

40. T. Armstrong *et al.*, Phys. Lett. **B167** (1986) 133; Phys. Lett. **B227** (1989) 186.

41. S. Lindenbaum, Proceedings of Conference *From Symmetries to Strings, Forty Years of Rochester Conferences*, Okubofest, Rochester, New York, May 5-6, 1990, BNL-45258.

42. B. Li *et al.*, Phys. Rev. **D35** (1987) 1070; Phys. Rev. **D40** (1989) 3648. For a recent review, see for example: D. Hitlin, AIP conference proceedings No.185, Particles and fields series 36, Glueballs, Hybrids, and Exotic Hadrons, Upton, NY1988, Editor S-U. Chung.

43. For example, H. Aihara *et al.*, Phys. Rev. Lett. **57** (1986) 404.

44. L.-P. Chen, representing the MARK-III collaboration, *Amplitude Analysis of the $K\overline{K}$ Systems in J/ψ Radiative Decay*, proceedings of the Rheinfels Workshop on Hadron Mass Spectrum, St. Goar, Germany, September 3-6, 1990, Nucl. Phys. **B 21** (Proc. Suppl.) (1990) 80-86; SLAC-PUB-5378 (1990).

45. L-P. Chen, representing the MARK III collaboration, *An Amplitude Analysis of the $K\overline{K}$ and $\pi^+\pi^-$ Systems ($m < 2GeV/c^2$) Produced in J/ψ Radiative Decay*, Proceedings of the Hadron' 91 conference, University of Maryland, College Park, MD, USA, August 12-16, 1991; SLAC-PUB-5669 (1991).

46. L-P. Chen and W. M. Dunwoodie, representing the MARK III collaboration, *Evidence for $\rho'(1600)$ in the Reaction $J/\psi \rightarrow \pi^0\pi^+\pi^-$*. Proceedings of the XV International Lepton Photon Symposium at High Energies, CERN, Geneva, Switzerland, July 24 - August 1, 1991; Proceedings of the Hadron' 91 conference, University of Maryland, College Park, MD, USA, August 12-16, 1991; SLAC-PUB-5674 (1991).

47. D. Bernstein *et al.*, Nucl. Instrum. Methods. **226** (1984) 301.

48. J. Roerhig *et al.*, Nucl. Instrum. Methods. **226** (1984) 319.

49. J. Brown *et al.*, Nucl. Instrum. Methods. **221** (1984) 503.

50. W. Toki *et al.*, Nucl. Instrum. Methods. **219** (1984) 220.

51. R. Fabrizio *et al.*, Nucl. Instrum. Methods. **222** (1984) 220.

52. J. Thaler *et al.*, IEEE TNS-30, (1982) 236; J. Becker, Ph.D thesis, University of Illinois at Urbana-Champagne (1984), unpublished.

53. A. Spadafora, Ph.D thesis, University of Illinois at Urbana-Champagne (1984), unpublished.

54. R. L. Ford and W. R. Nelson, SLAC-PUB-0210, June, 1978.

55. T. Himel *et al.* Phys. Rev. Lett. **45** (1980) 1146.

56. W. G. Yan, High Energy and Nuclear Physics Journal (in Chinese),**14** (1990) 193; Procedings of the Hadron' 91 conference, University of Maryland, College Park, MD,USA, August 12-16, 1991.

57. F. James, M. Roos, MINUIT Function Minimization and Error Analysis, release 89.12j, CERN D506 MINUIT.

58. N. A. Tornqvist Phys. Rev. Lett. **67** (1991) 556.

59. S. Lindenbaum, BNL-45878, Feb, 1991.

60. F. Close and Z. Li RAL-91-039, May, 1991.

61. F. Close, *Conference Summary*, proceedings of the Rheinfels Workshop on Hadron Mass Spectrum, St. Goar, Germany, September 3-6, 1990, Nucl. Phys. **B 21** (Proc. Suppl.) (1990) 423-429.

62. M. Krammer, Phys. Lett. **B74** (1978) 361.

63. F. Close and Z. Li Phys. Rev. Lett. **24** (1991) 3109.

64. J. D. Richman, Ph.D Thesis, California Institute of Technology, CALT-68-1148 (1984), unpublished.

65. S. U. Chung, (eq. (4.25) in *Spin Formalisms*, CERN-71-8, (1971).

66. J. M. Blatt and V. F. Weisskopf, *Theoretical Nuclear Physics*, (Wiley, New York, 1952), p. 361.